Electronic Supplementary Material (ESI) for Dalton Transactions.
This journal is © The Royal Society of Chemistry 2019

Electronic Supplementary Material (ESI) for Dalton Transactions.
This journal is © The Royal Society of Chemistry 2019

Supporting Information

Syntheses and Quadratic Nonlinear Optical Properties of Fluorenyl- and 4-Ethynylphenyl-Functionalized *o*-Carboranes

Peng Jiang,[a] Zhaojin Wang,[a] Graeme J. Moxey,[b] Mahbod Morshedi,[b] Adam Barlow,[b] Genmiao Wang,[b] Cristóbal Quintana,[b] Chi Zhang,[a] Marie P. Cifuentes[a,b] and Mark G. Humphrey[a,b]

[a] School of Chemical and Material Engineering, Jiangnan University, Wuxi 214122, Jiangsu Province, China.
E-mail: Mark.Humphrey@anu.edu.au

[b] Research School of Chemistry, Australian National University, Canberra, ACT 2601, Australia.

Table of Contents

NMR spectra

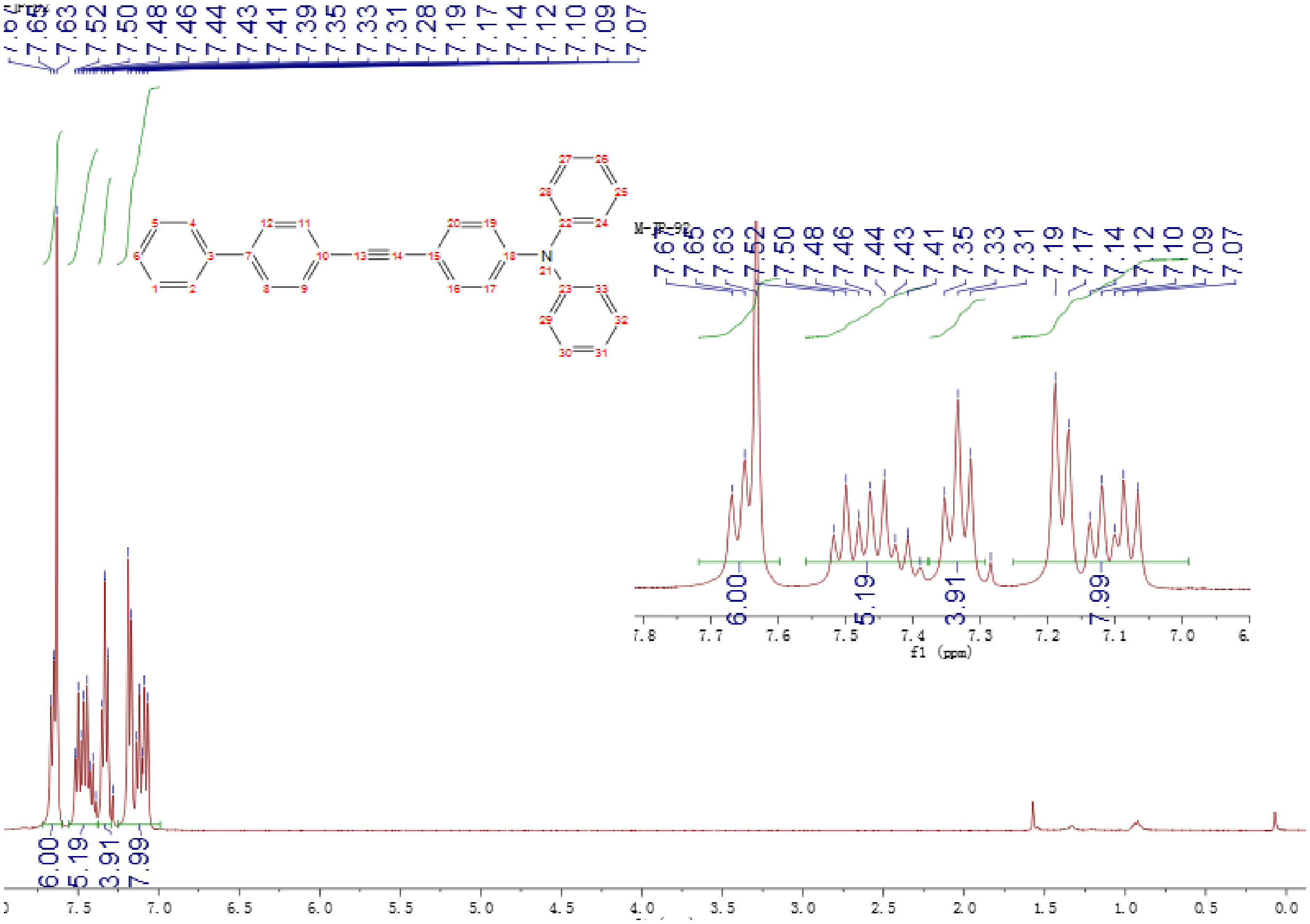

Figure S1. ^{1}H NMR spectrum of **1** (400 MHz, $CDCl_3$).

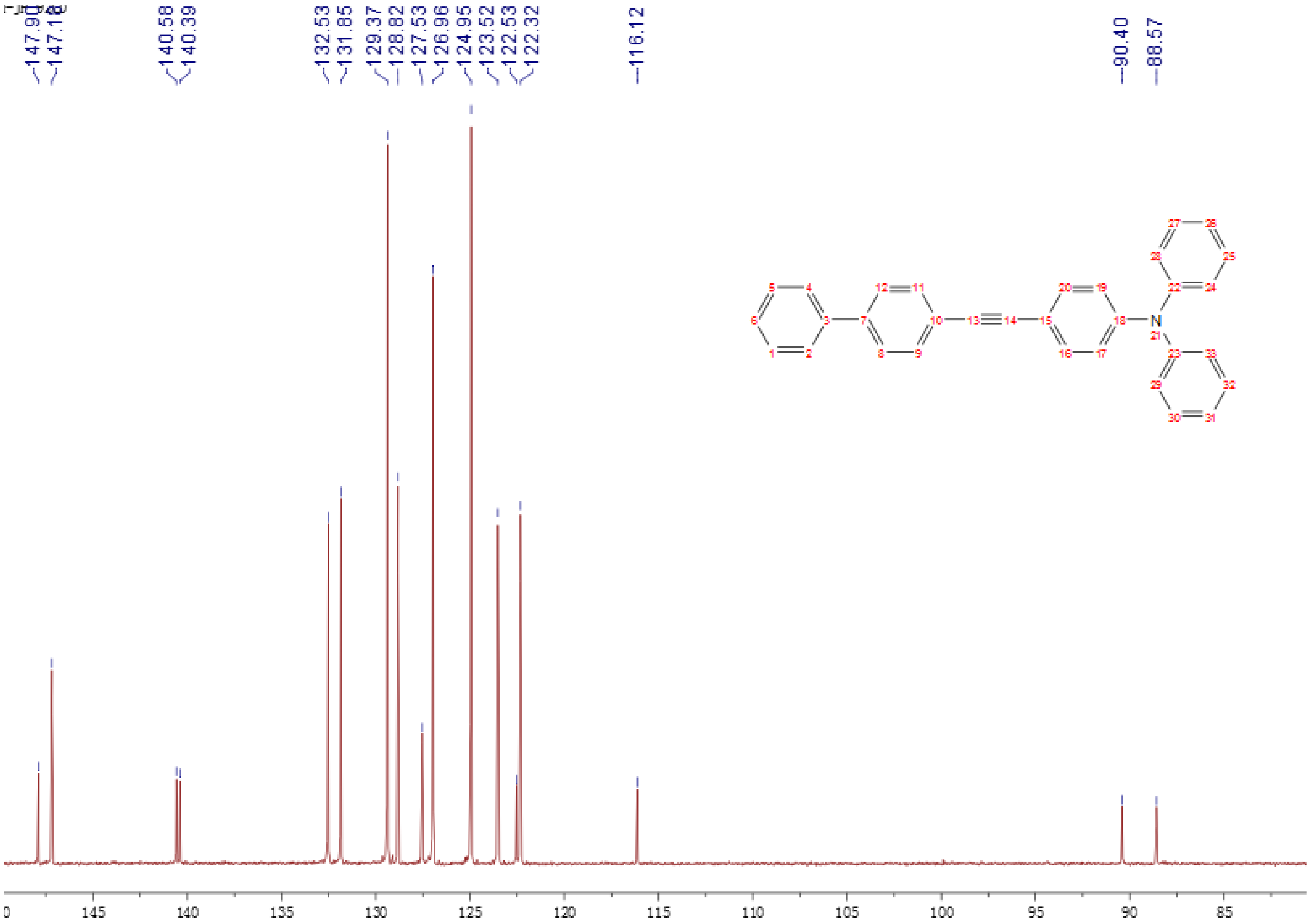

Figure S2. ^{13}C NMR spectrum of **1** (101 MHz, $CDCl_3$).

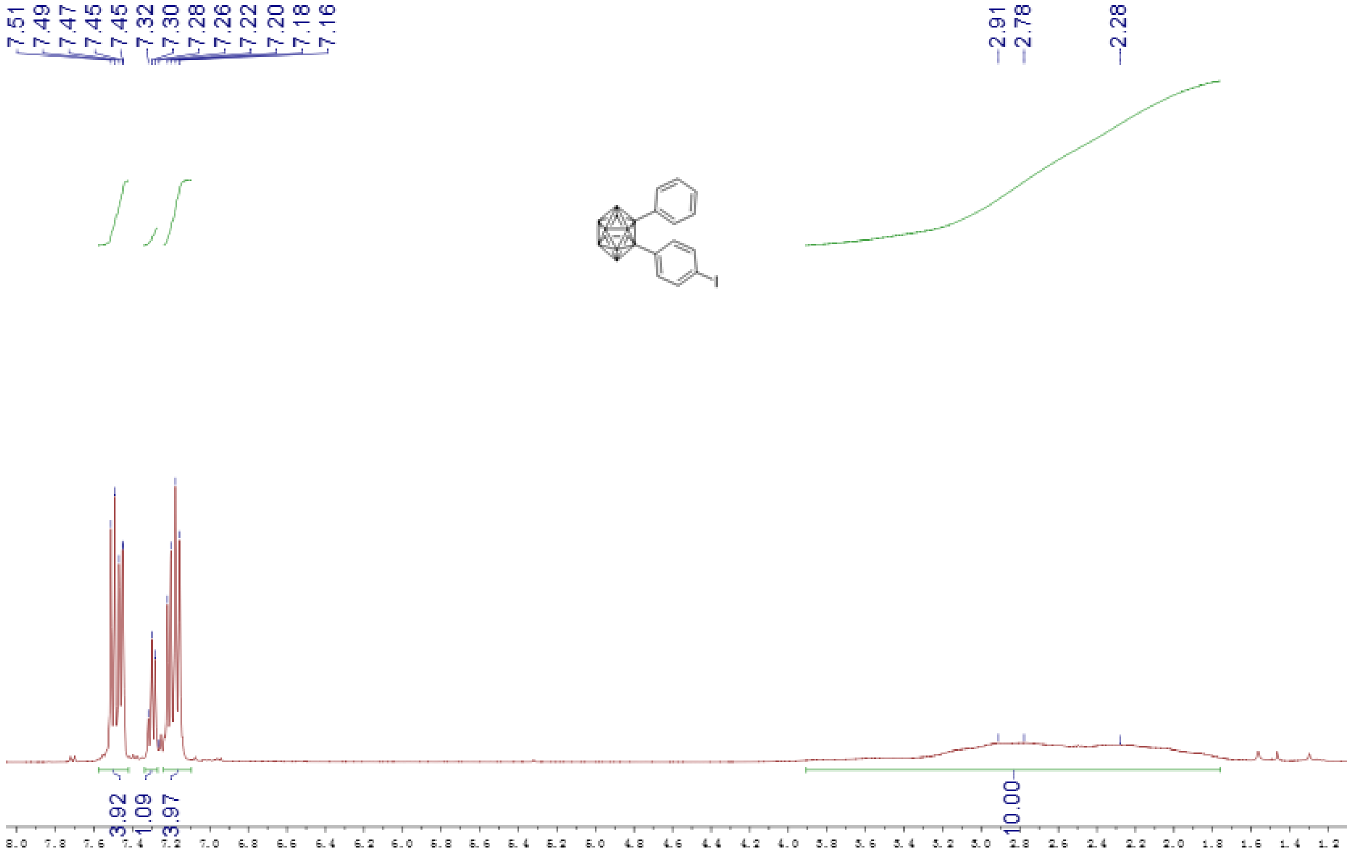

Figure S3. ^1H NMR spectrum of **3** (400 MHz, $CDCl_3$).

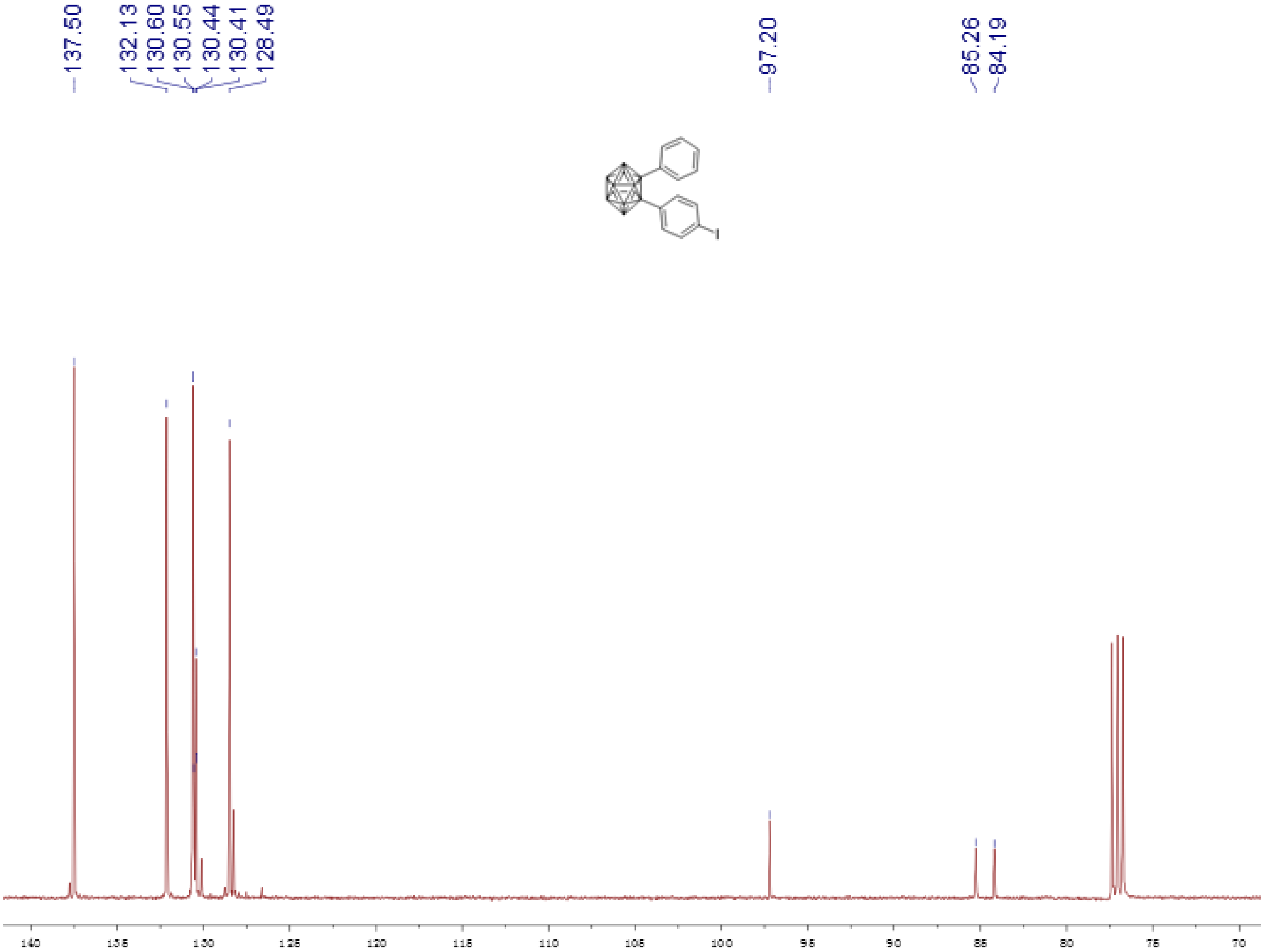

Figure S4. ^{13}C NMR spectrum of **3** (101 MHz, $CDCl_3$).

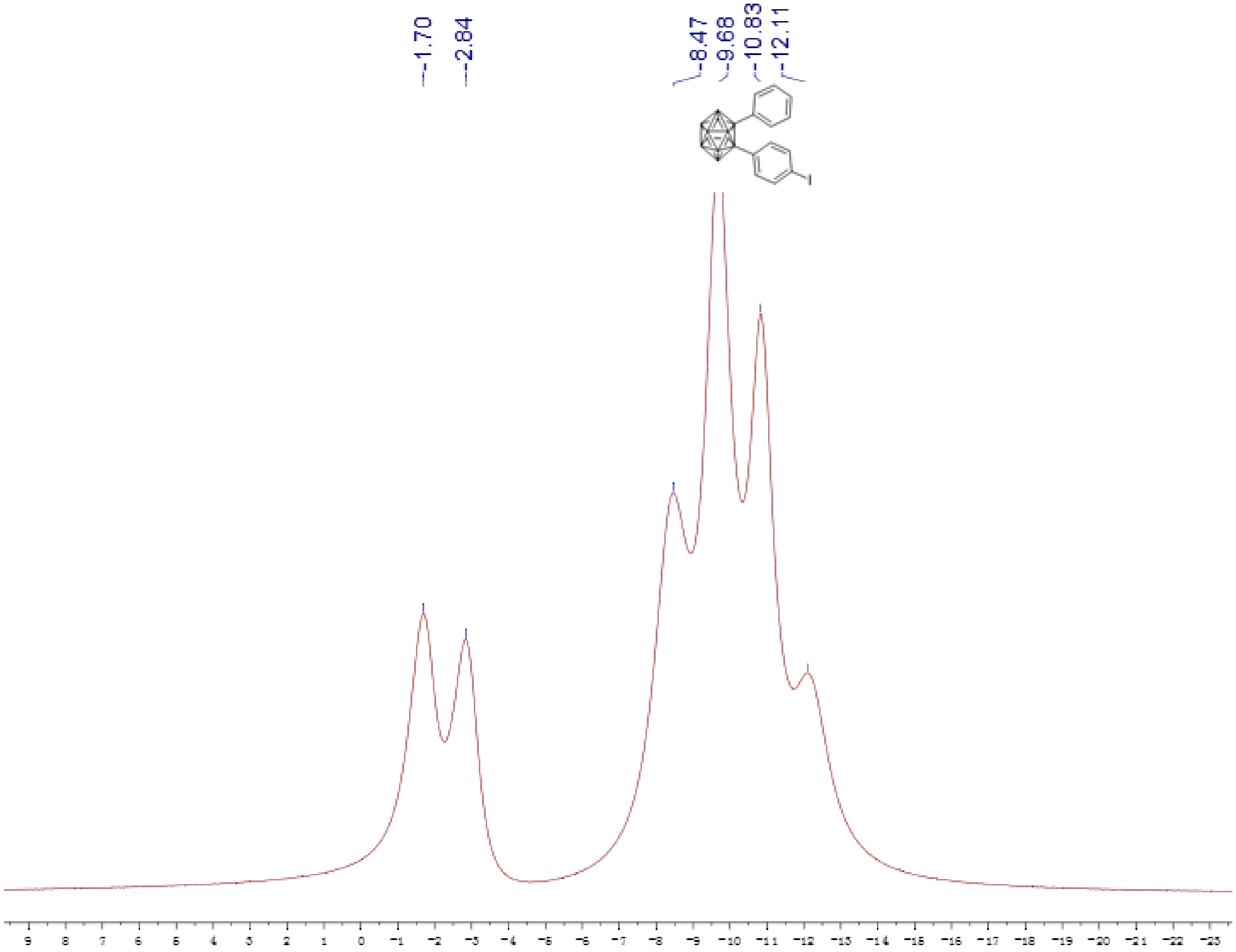

Figure S5. ^{11}B NMR spectrum of **3** (128 MHz, $CDCl_3$).

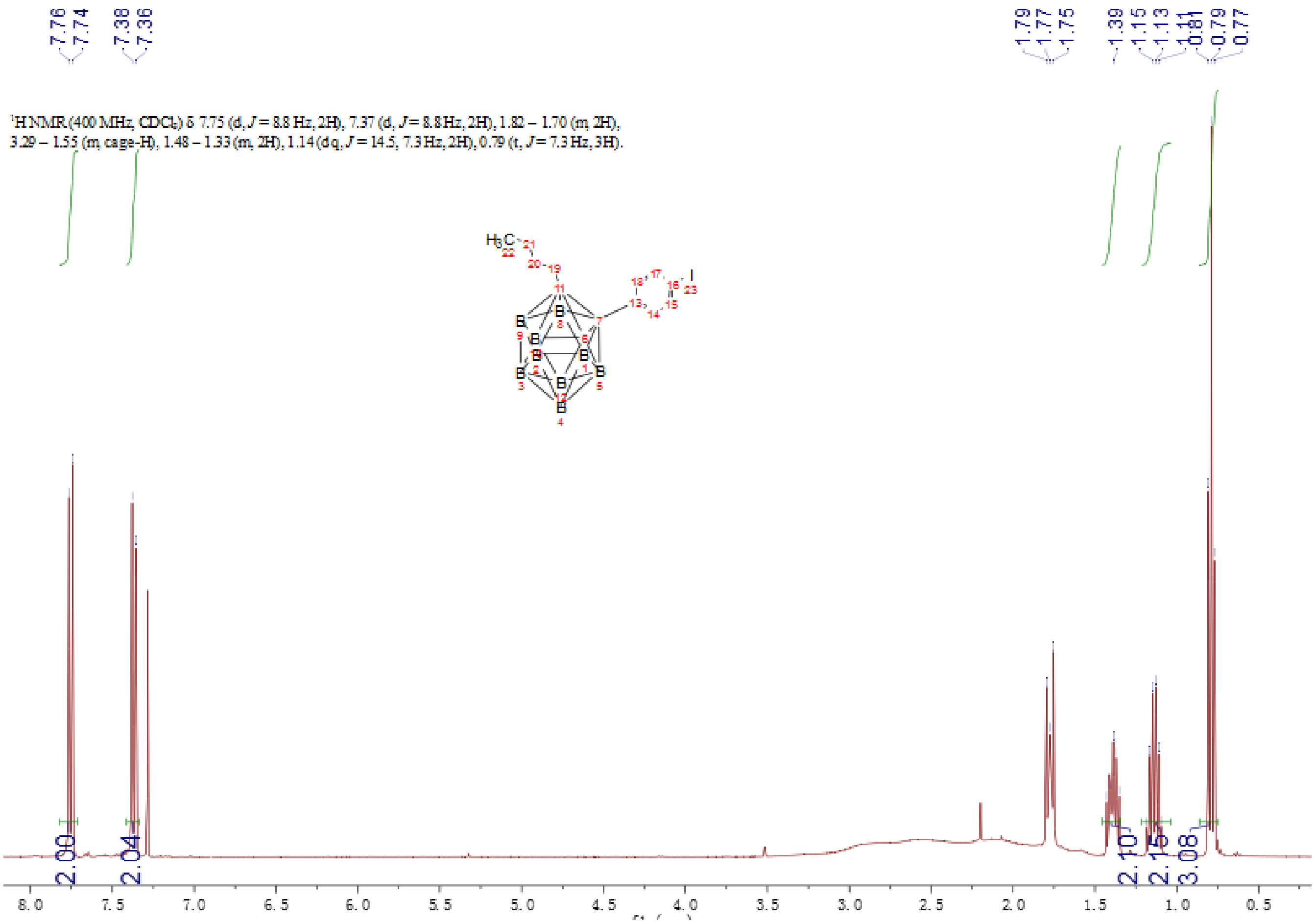

^{1}H NMR (400 MHz, CDCl$_3$) δ 7.75 (d, J = 8.8 Hz, 2H), 7.37 (d, J = 8.8 Hz, 2H), 1.82 – 1.70 (m, 2H), 3.29 – 1.55 (m, cage-H), 1.48 – 1.33 (m, 2H), 1.14 (dq, J = 14.5, 7.3 Hz, 2H), 0.79 (t, J = 7.3 Hz, 3H).

Figure S6. ^{1}H NMR spectrum of **4** (400 MHz, CDCl$_3$).

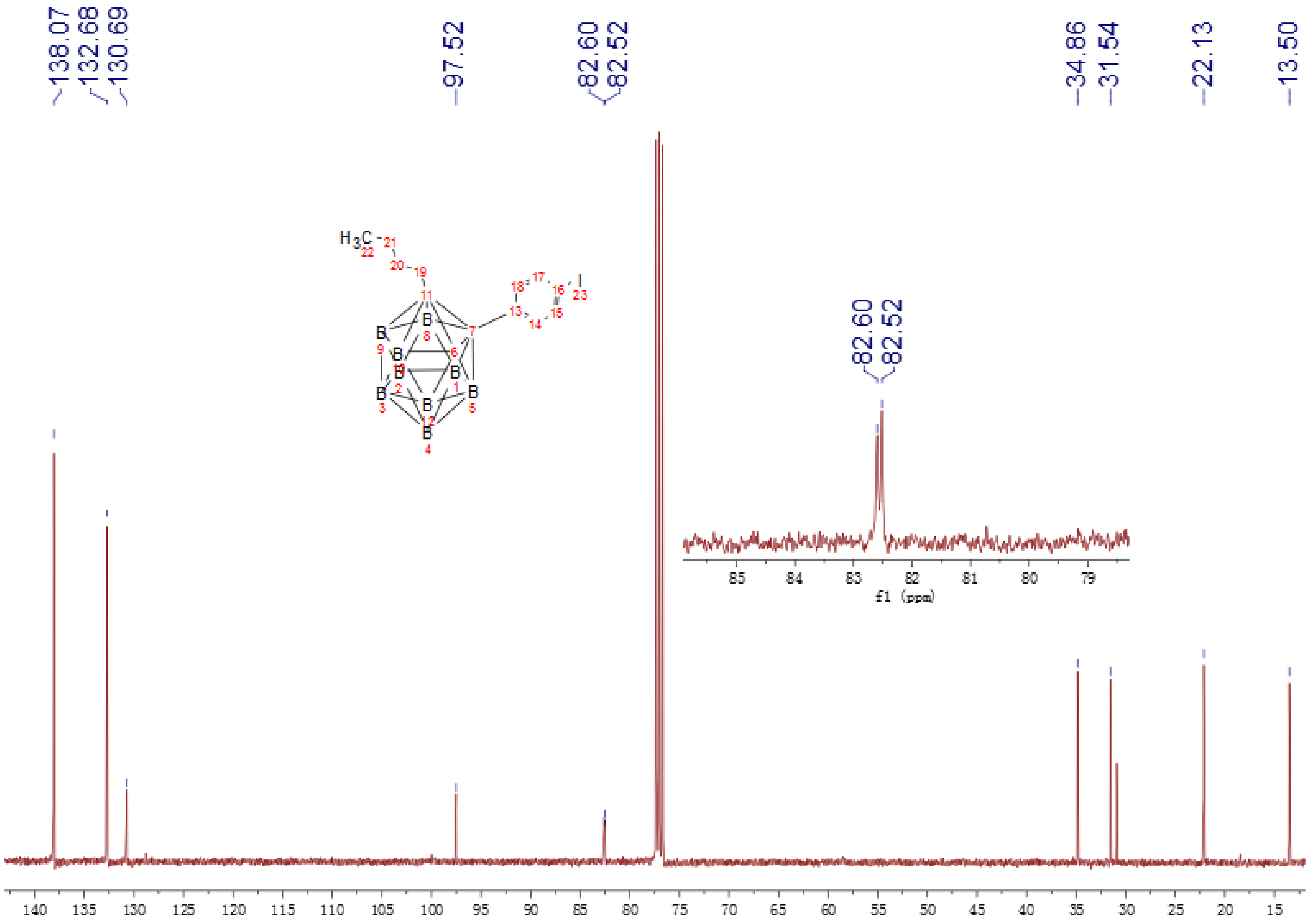

Figure S7. ^{13}C NMR spectrum of **4** (101 MHz, $CDCl_3$).

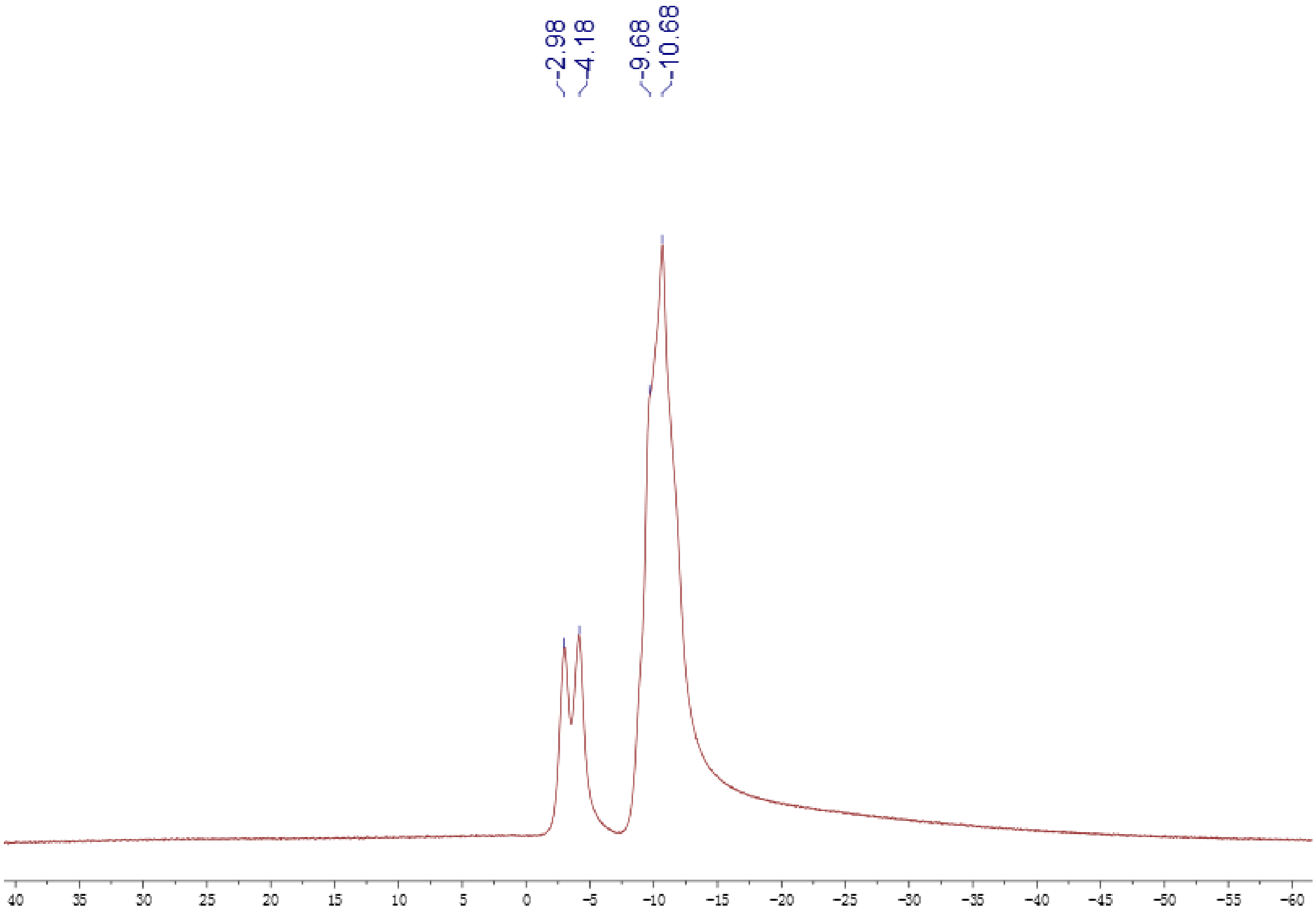

Figure S8. ^{11}B NMR spectrum of **4** (128 MHz, $CDCl_3$).

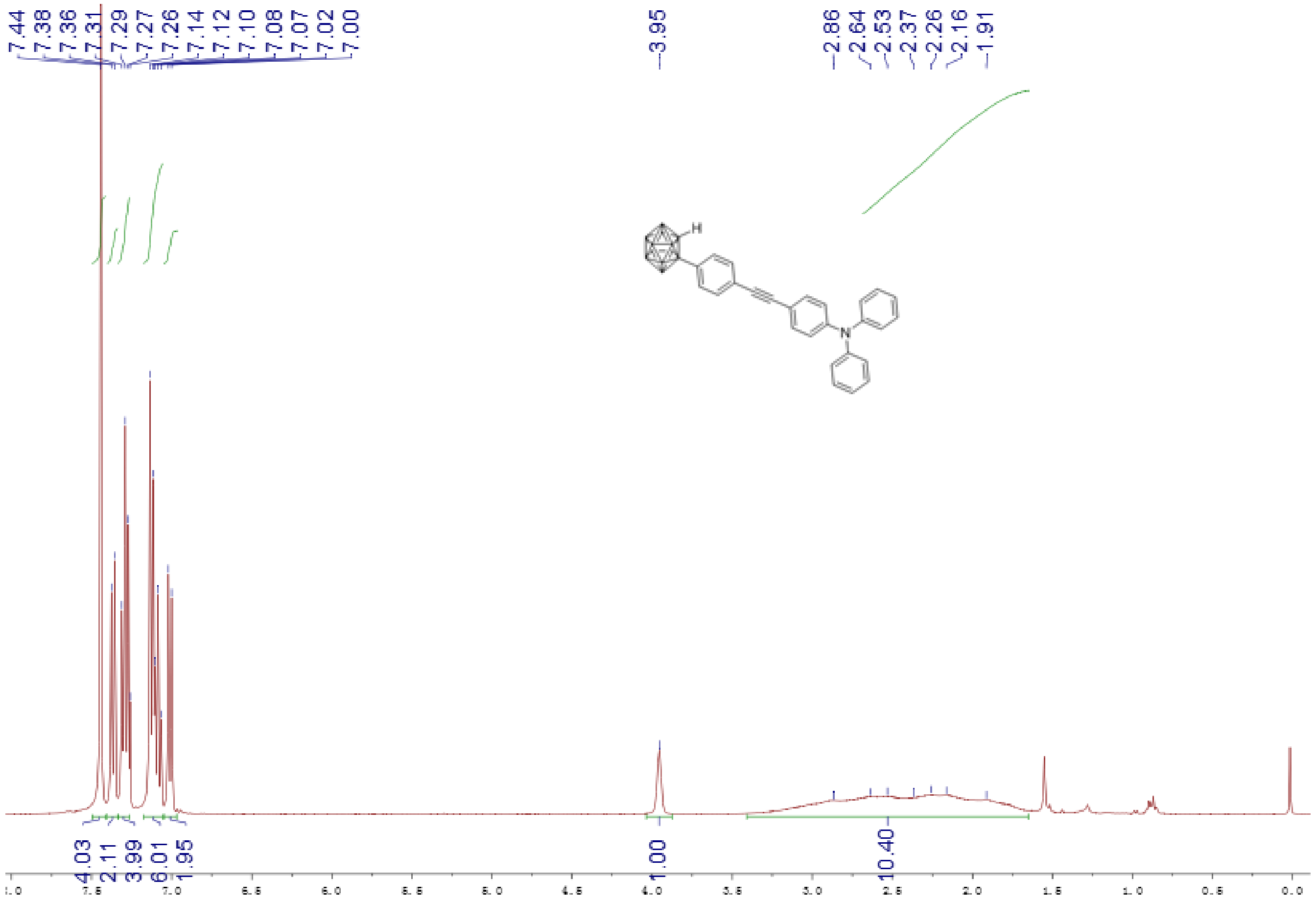

Figure S9. ^{1}H NMR spectrum of **5** (400 MHz, $CDCl_3$).

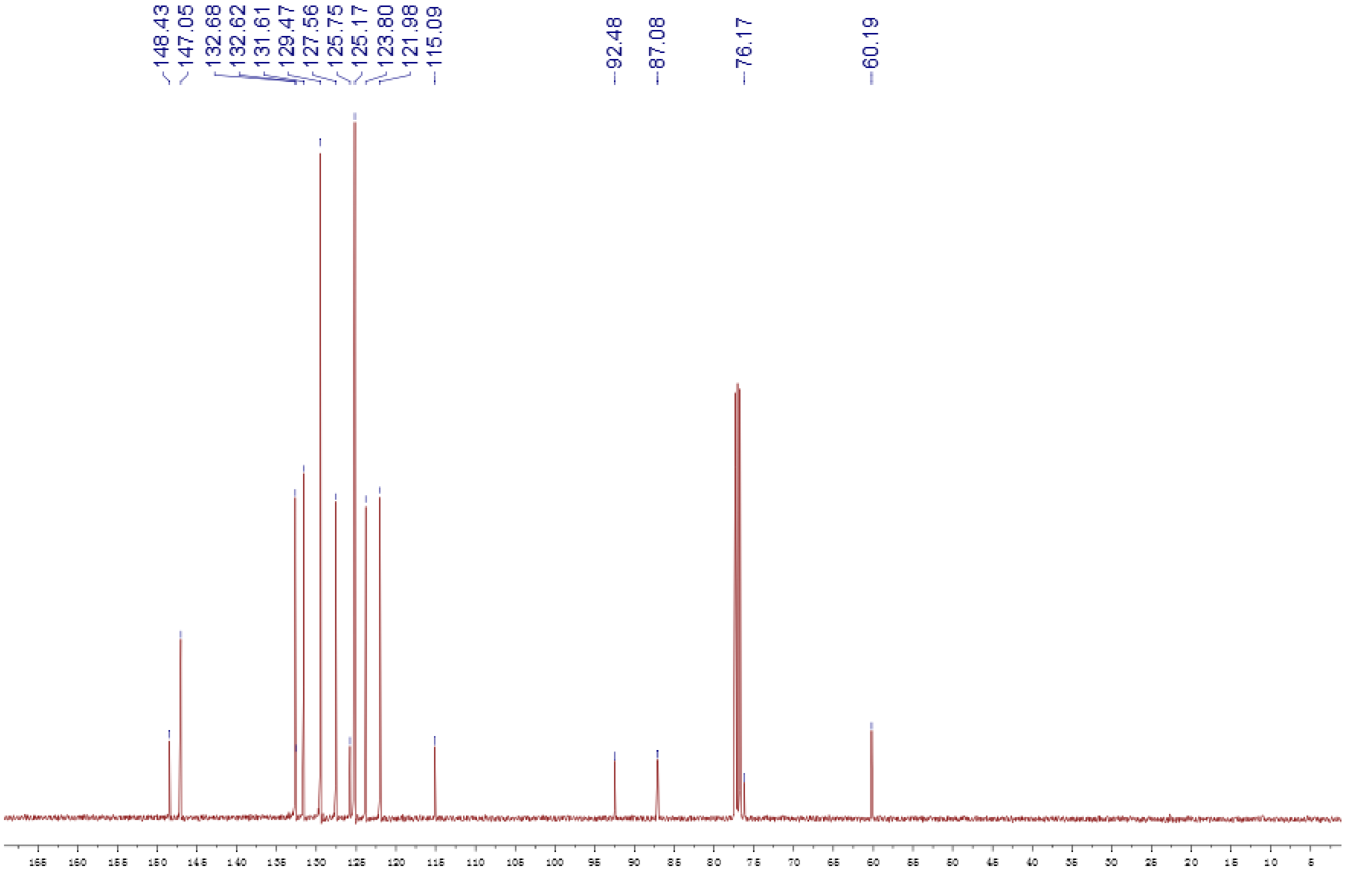

Figure S10. ^{13}C NMR spectrum of **5** (101 MHz, $CDCl_3$).

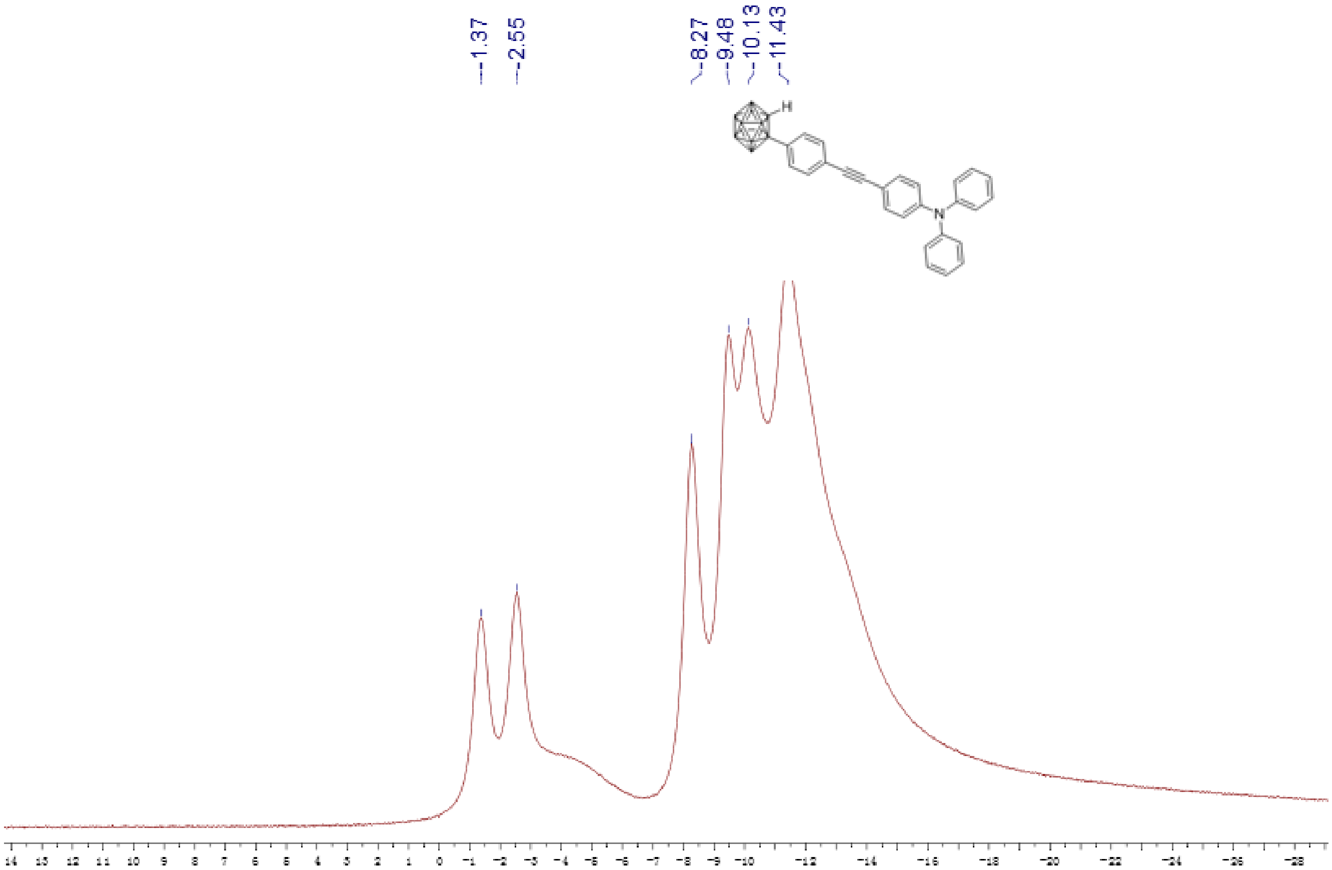

Figure S11. ^{11}B NMR spectrum of **5** (128 MHz, $CDCl_3$).

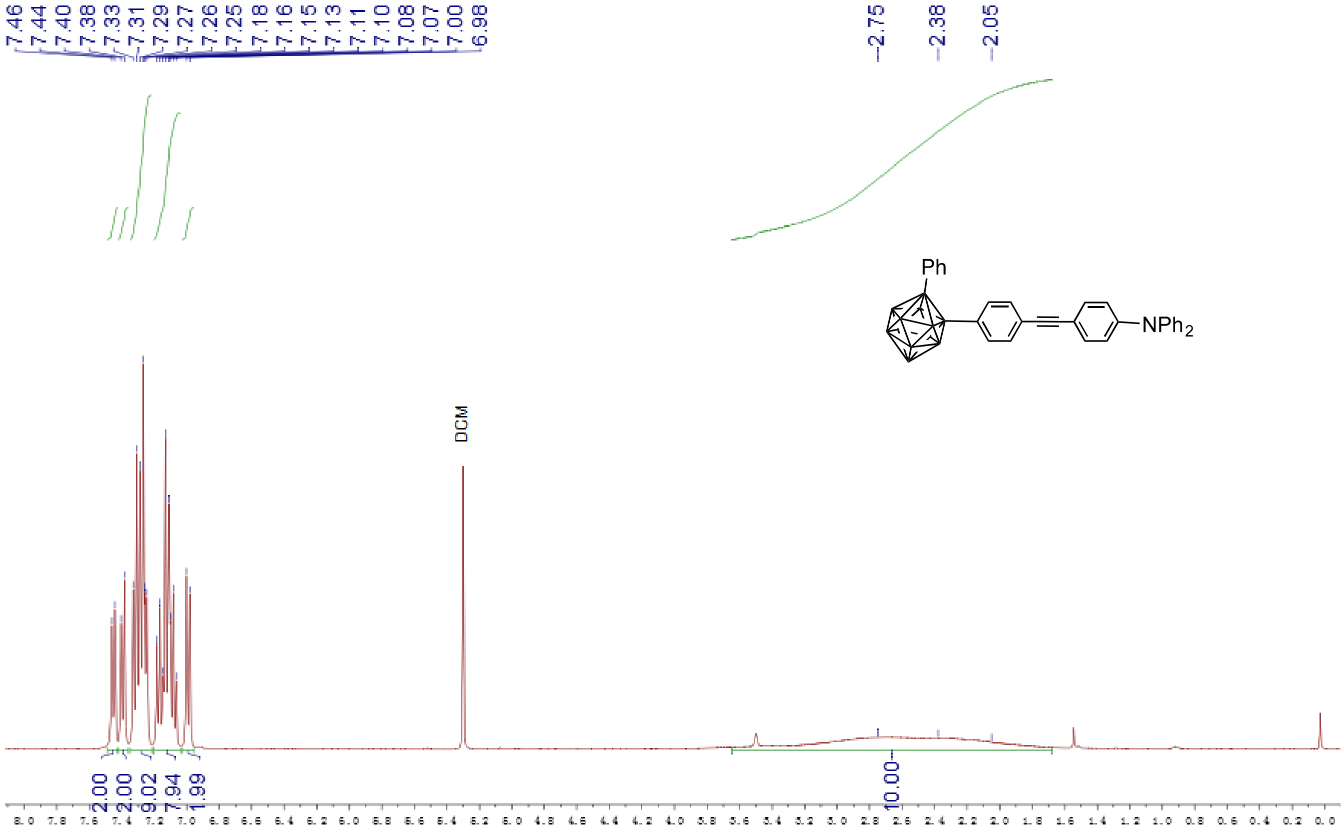

Figure S12. ^{1}H NMR spectrum of **6** (400 MHz, CDCl$_3$).

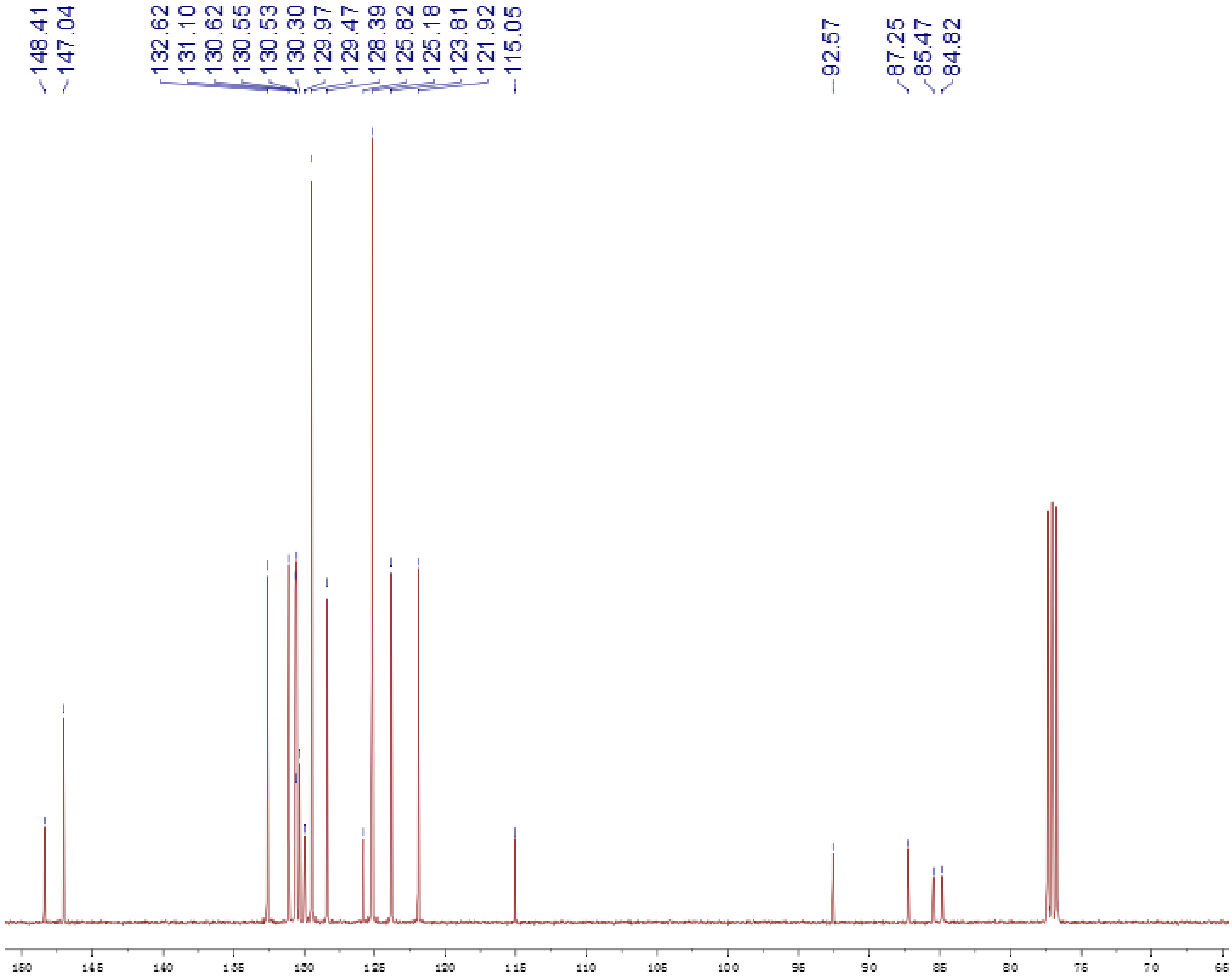

Figure S13. ^{13}C NMR spectrum of **6** (101 MHz, $CDCl_3$).

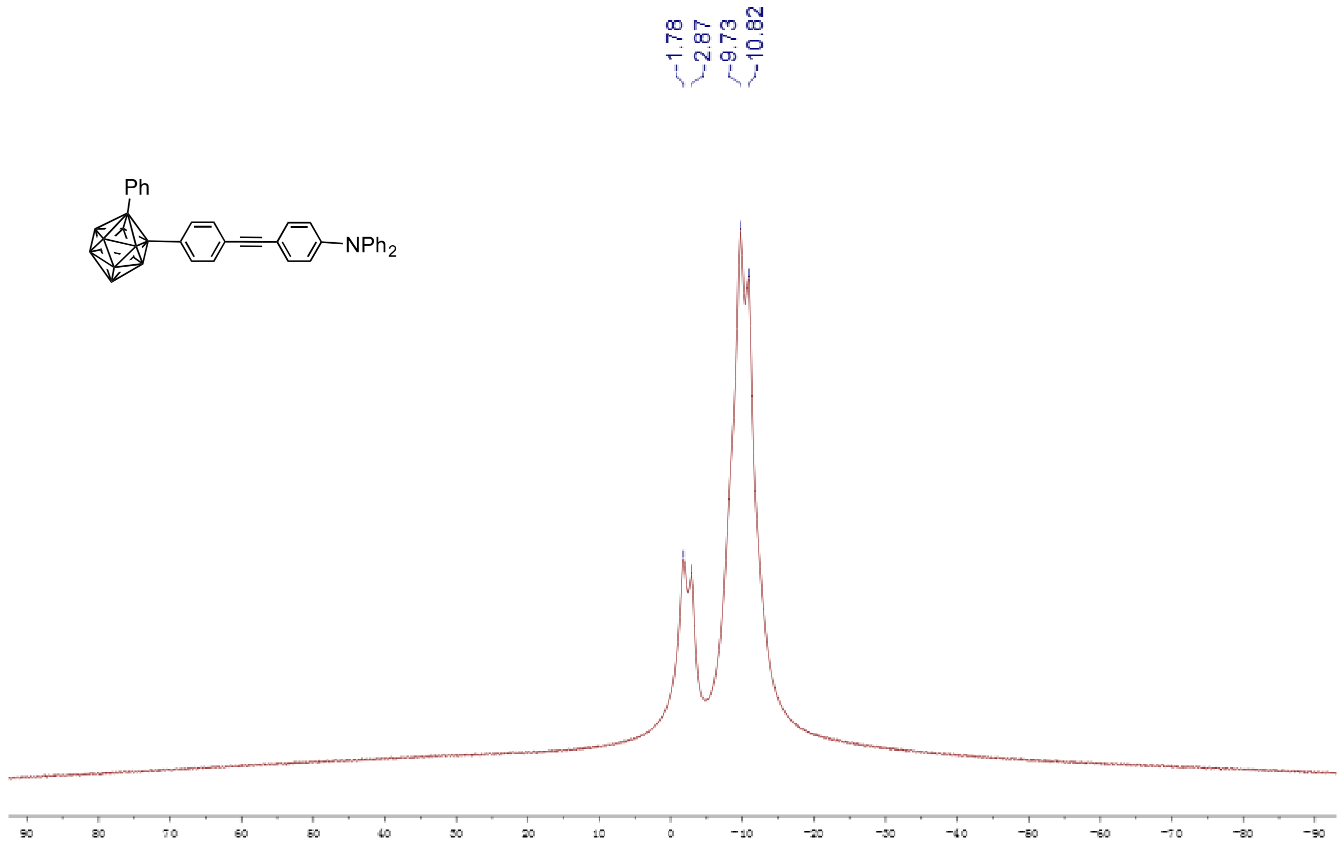

Figure S14. ^{11}B NMR spectrum of **6** (128 MHz, $CDCl_3$).

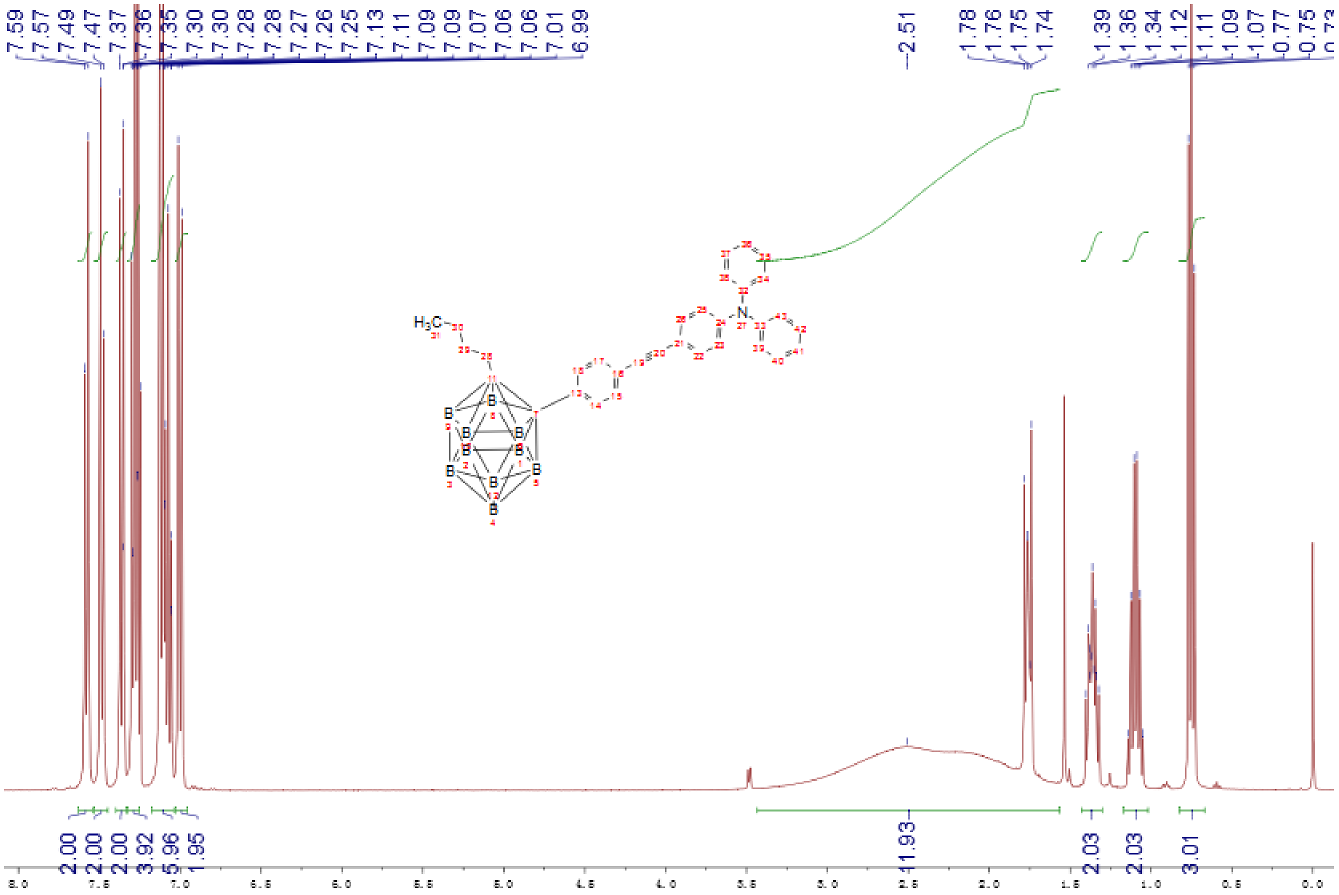

Figure S15. ^{1}H NMR spectrum of **7** (400 MHz, $CDCl_3$).

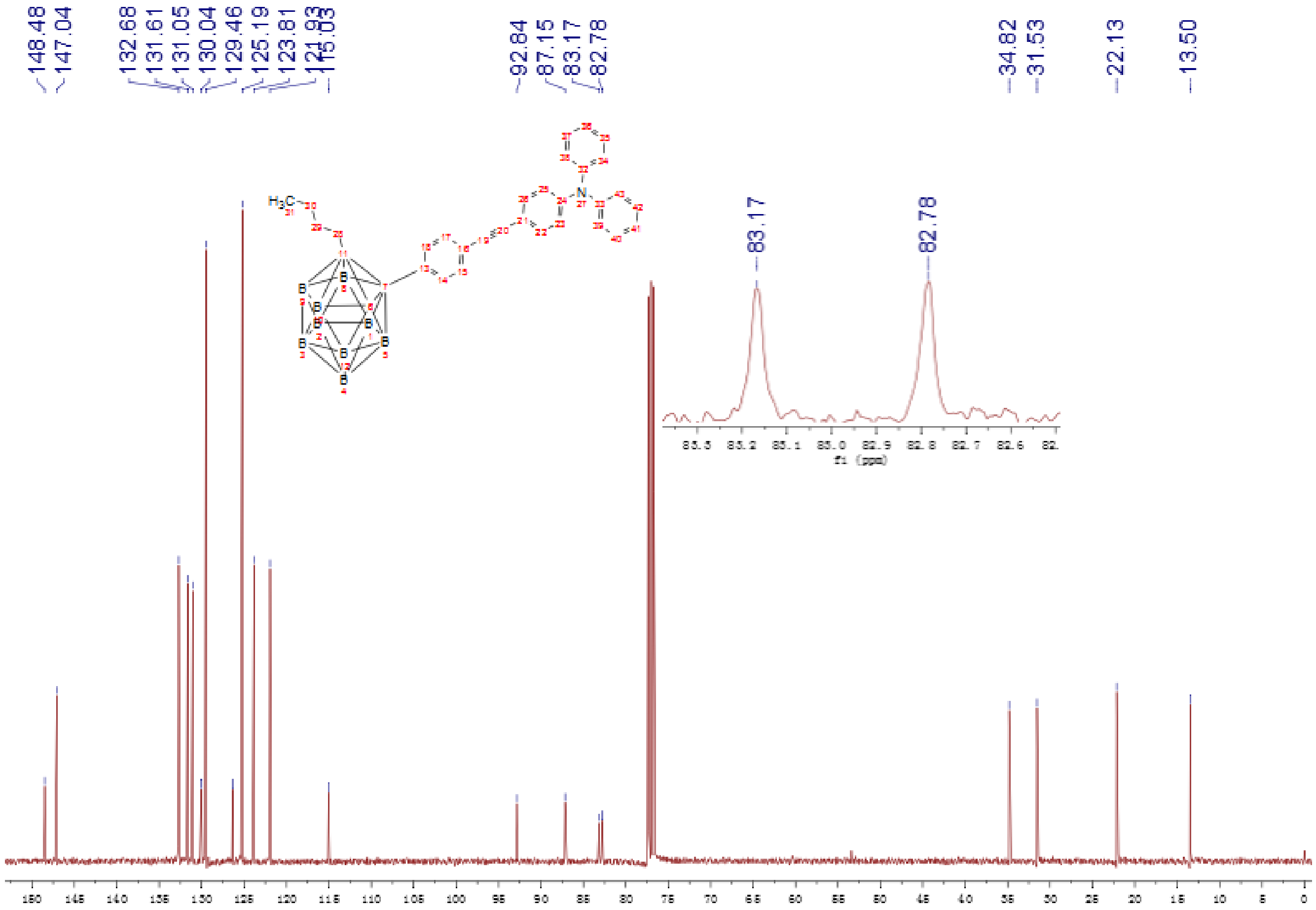

Figure S16. ^{13}C NMR spectrum of **7** (101 MHz, CDCl$_3$).

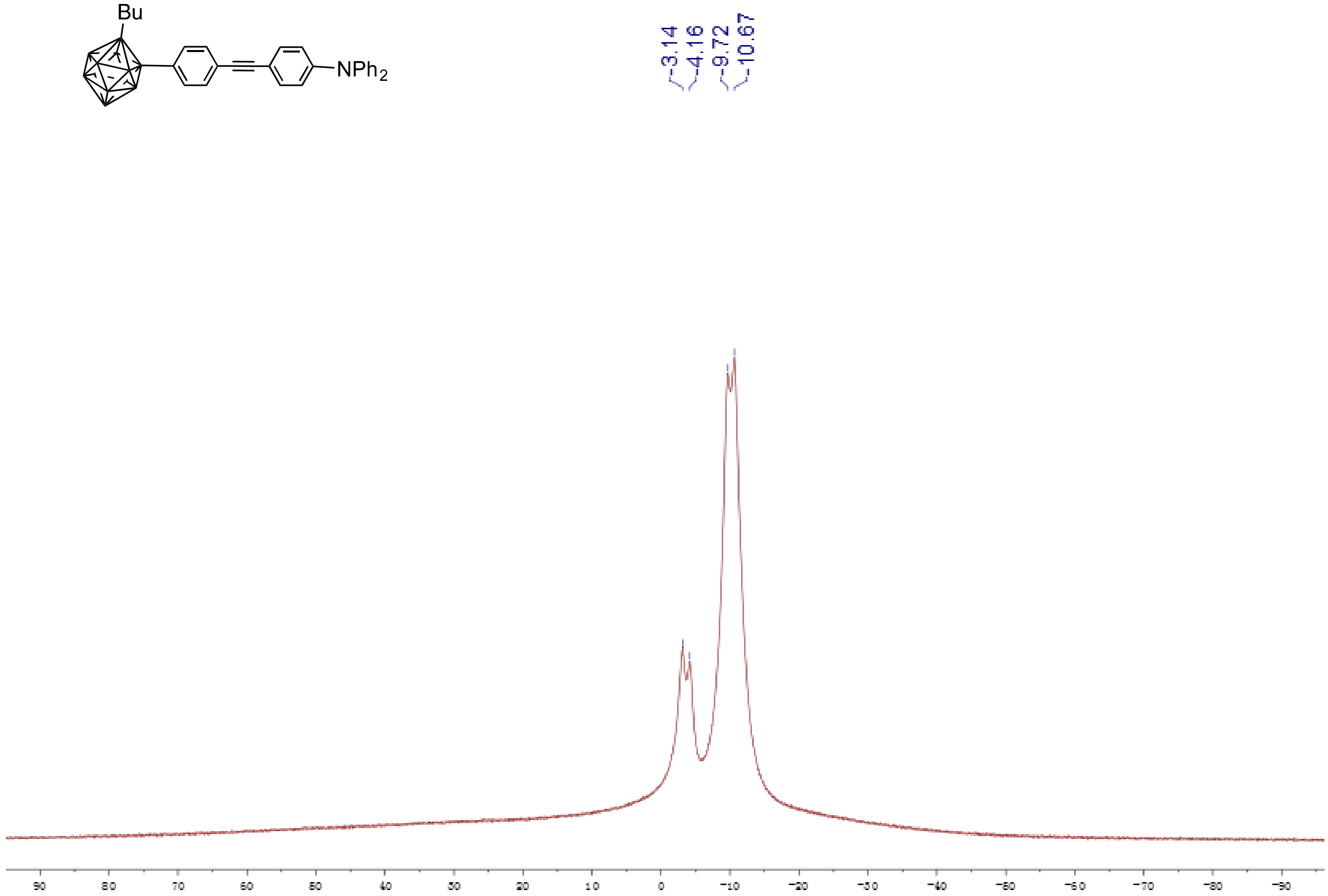

Figure S17. ^{11}B NMR spectrum of **7** (128 MHz, $CDCl_3$).

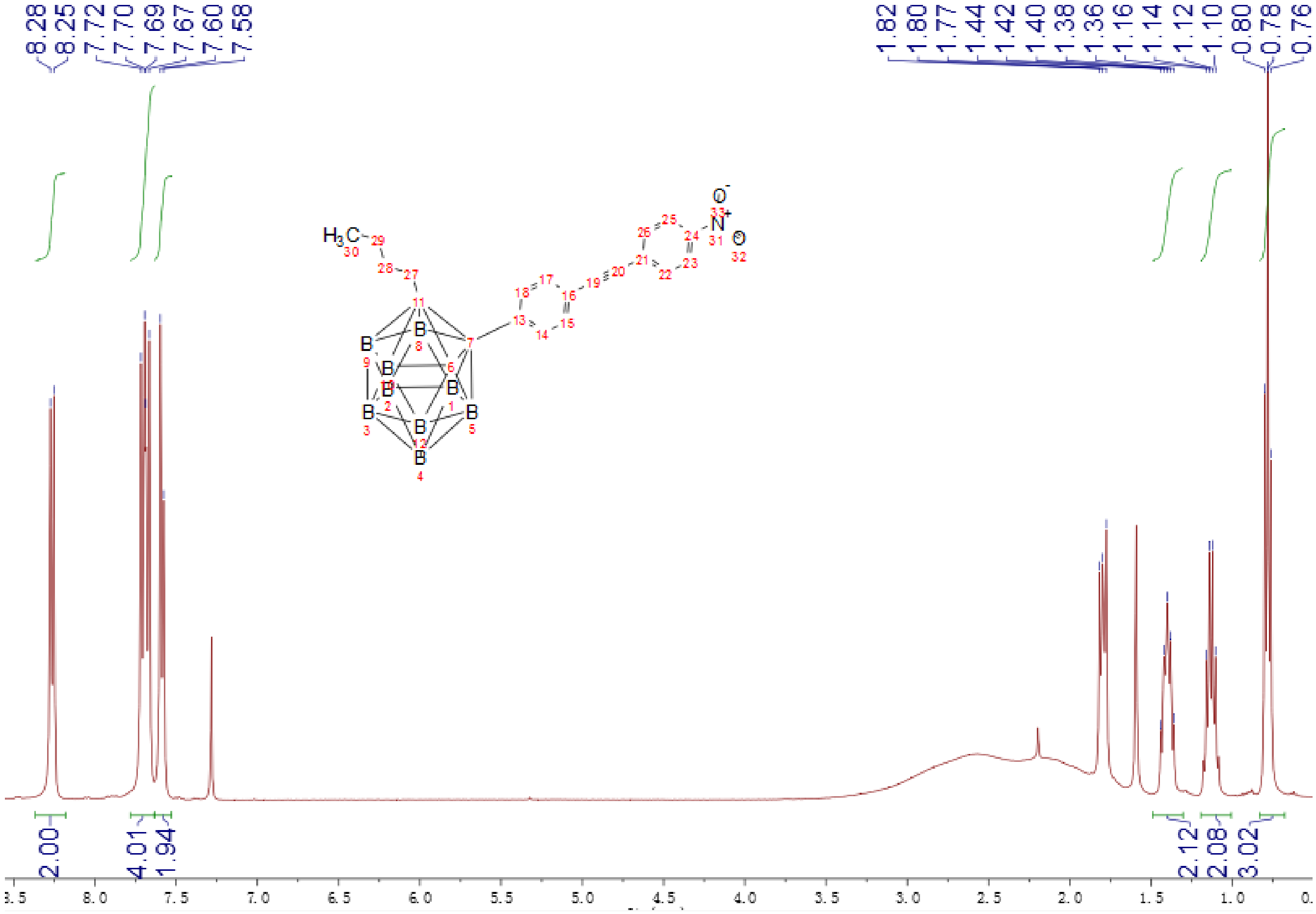

Figure S18. ^{1}H NMR spectrum of **8** (400 MHz, $CDCl_3$).

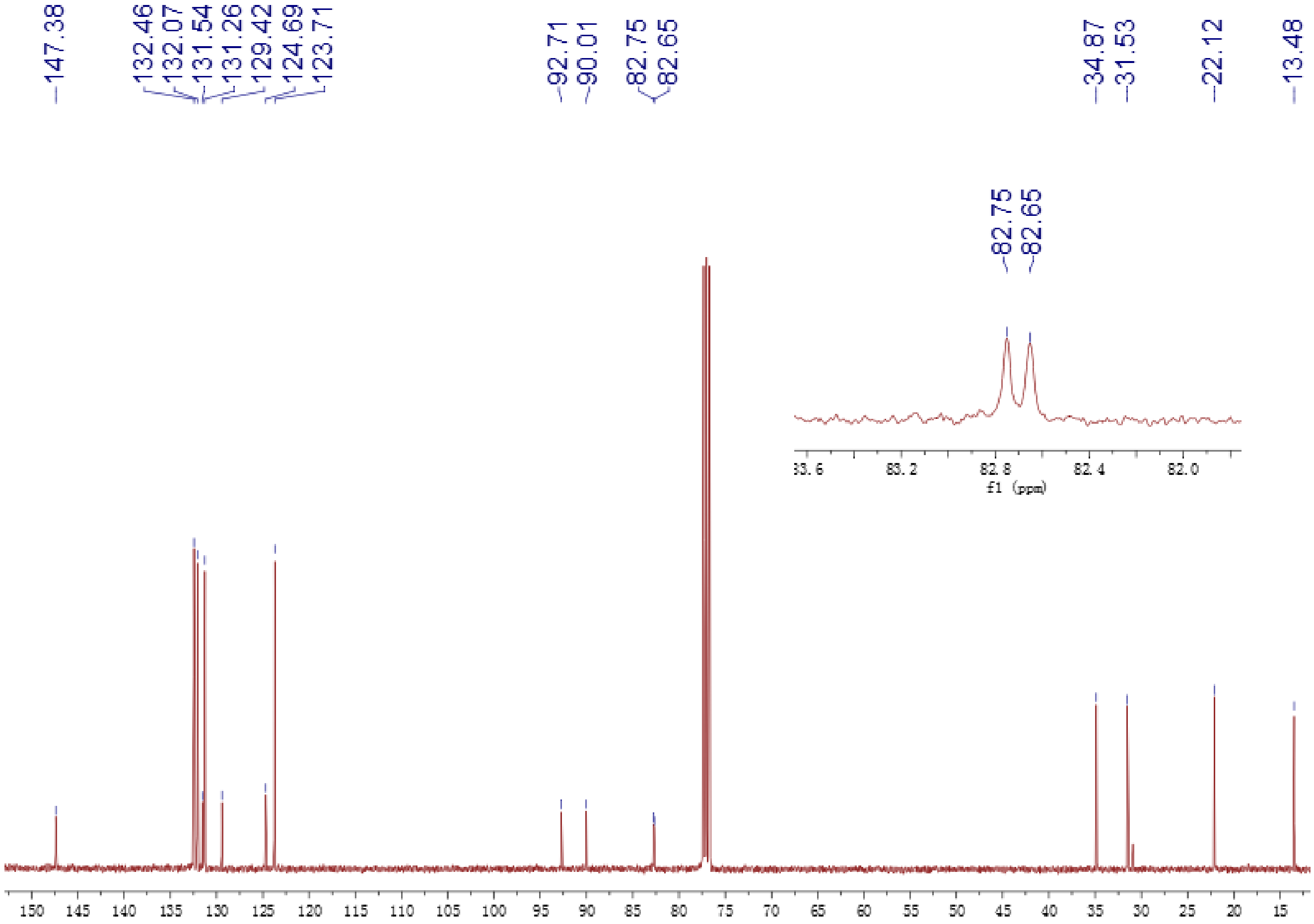

Figure S19. ^{13}C NMR spectrum of **8** (101 MHz, CDCl$_3$).

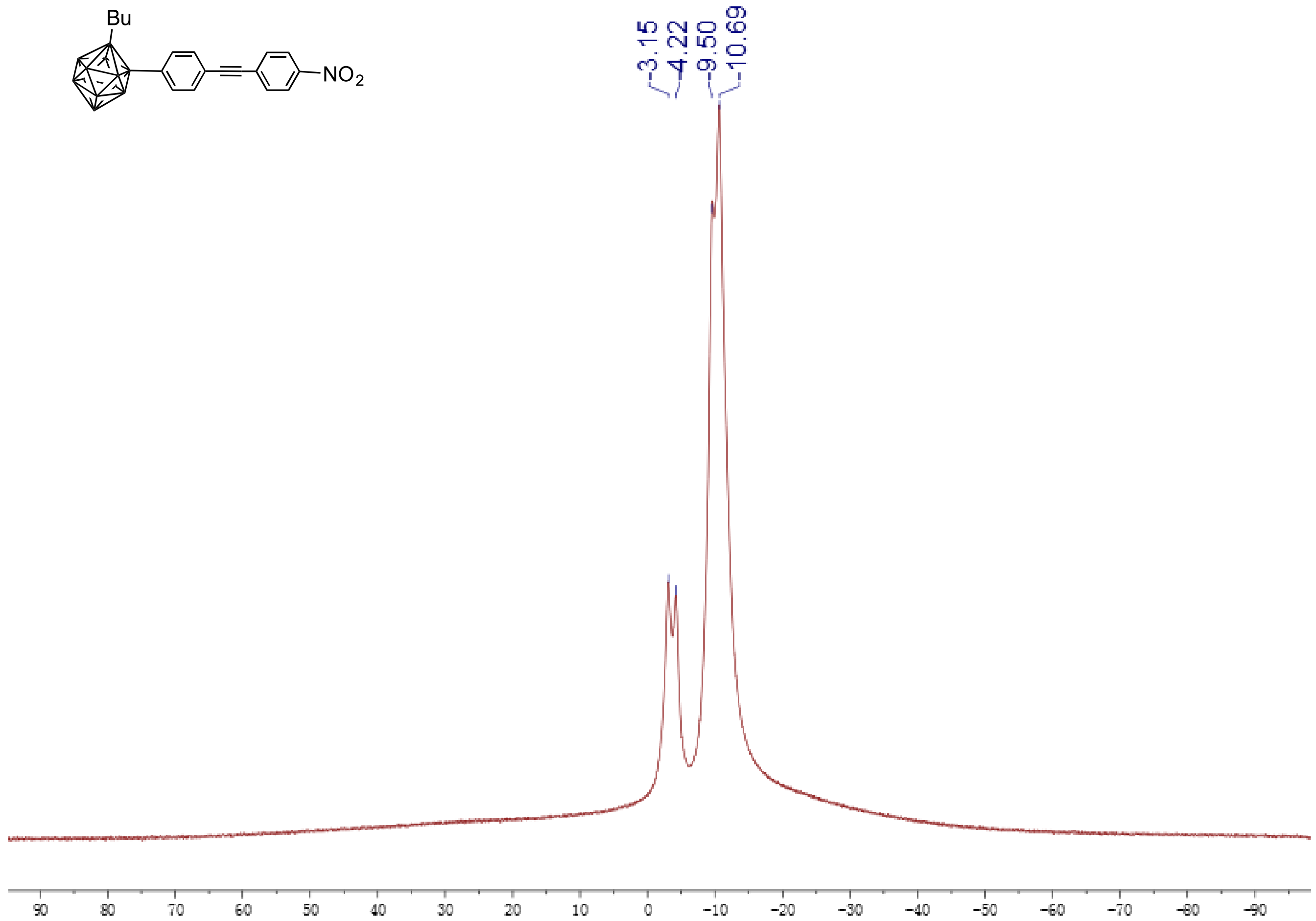

Figure S20. ^{11}B NMR spectrum of **8** (128 MHz, CDCl$_3$).

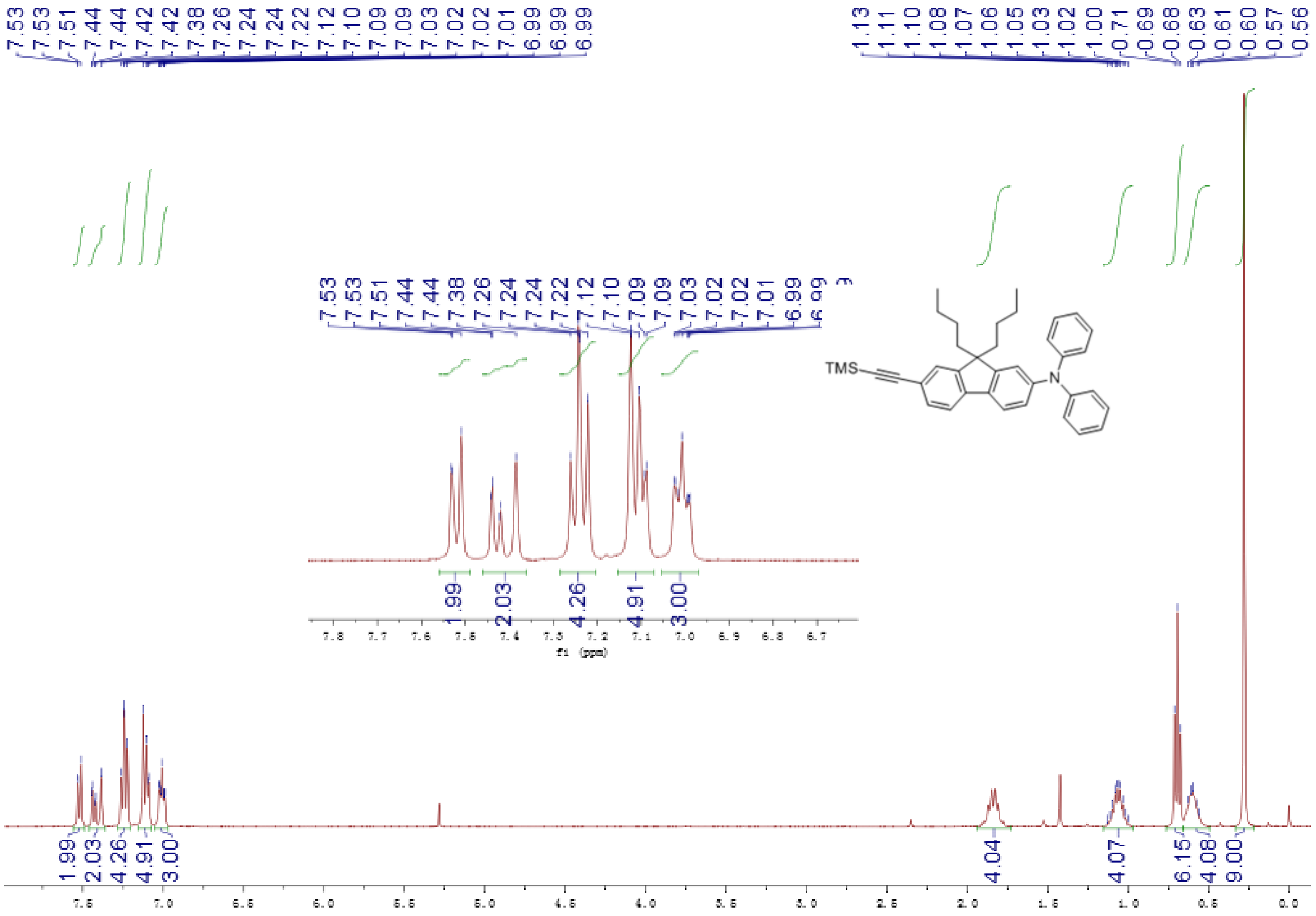

Figure S21. ^{1}H NMR spectrum of **10** (400 MHz, $CDCl_3$).

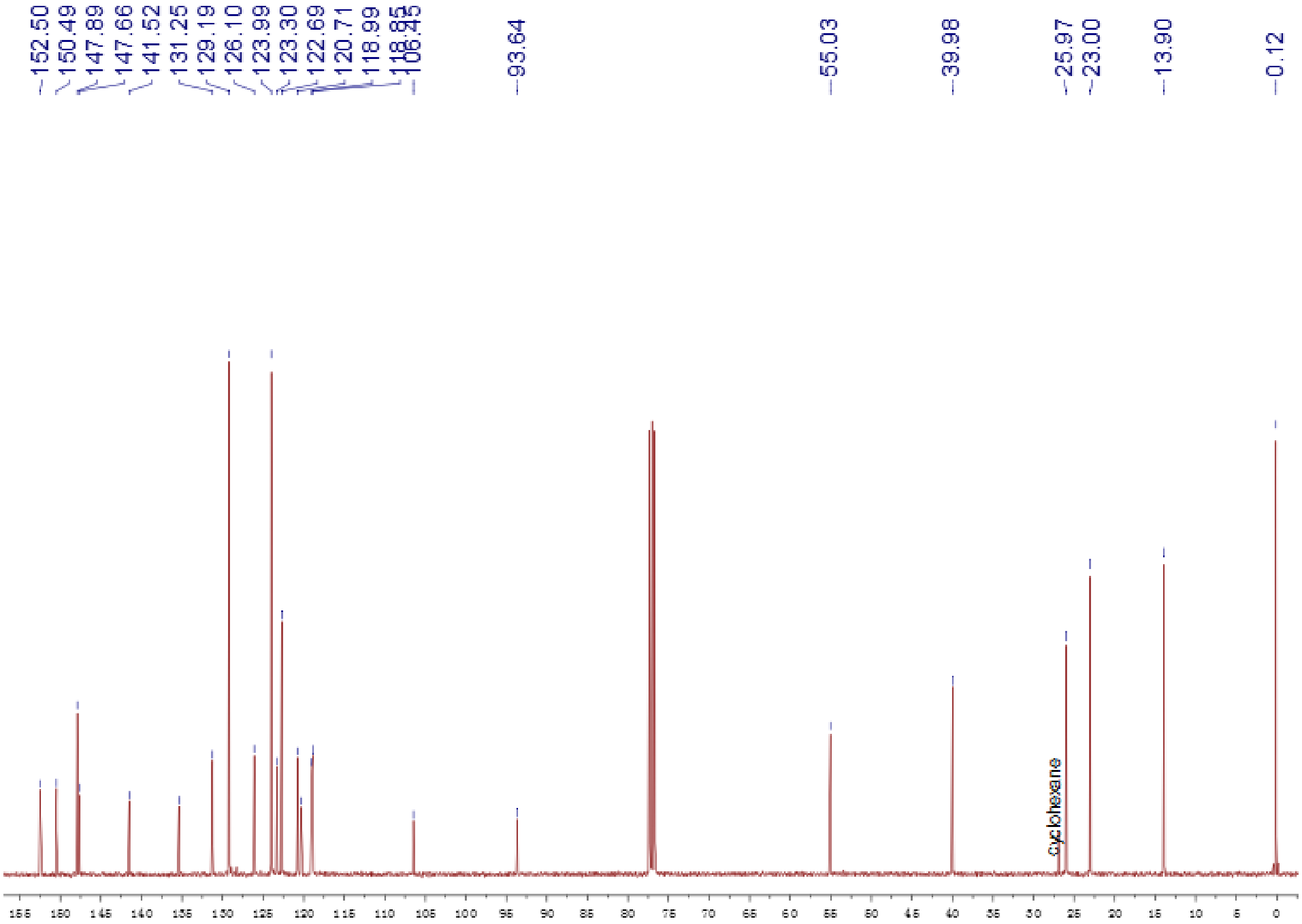

Figure S22. ^{13}C NMR spectrum of **10** (101 MHz, $CDCl_3$).

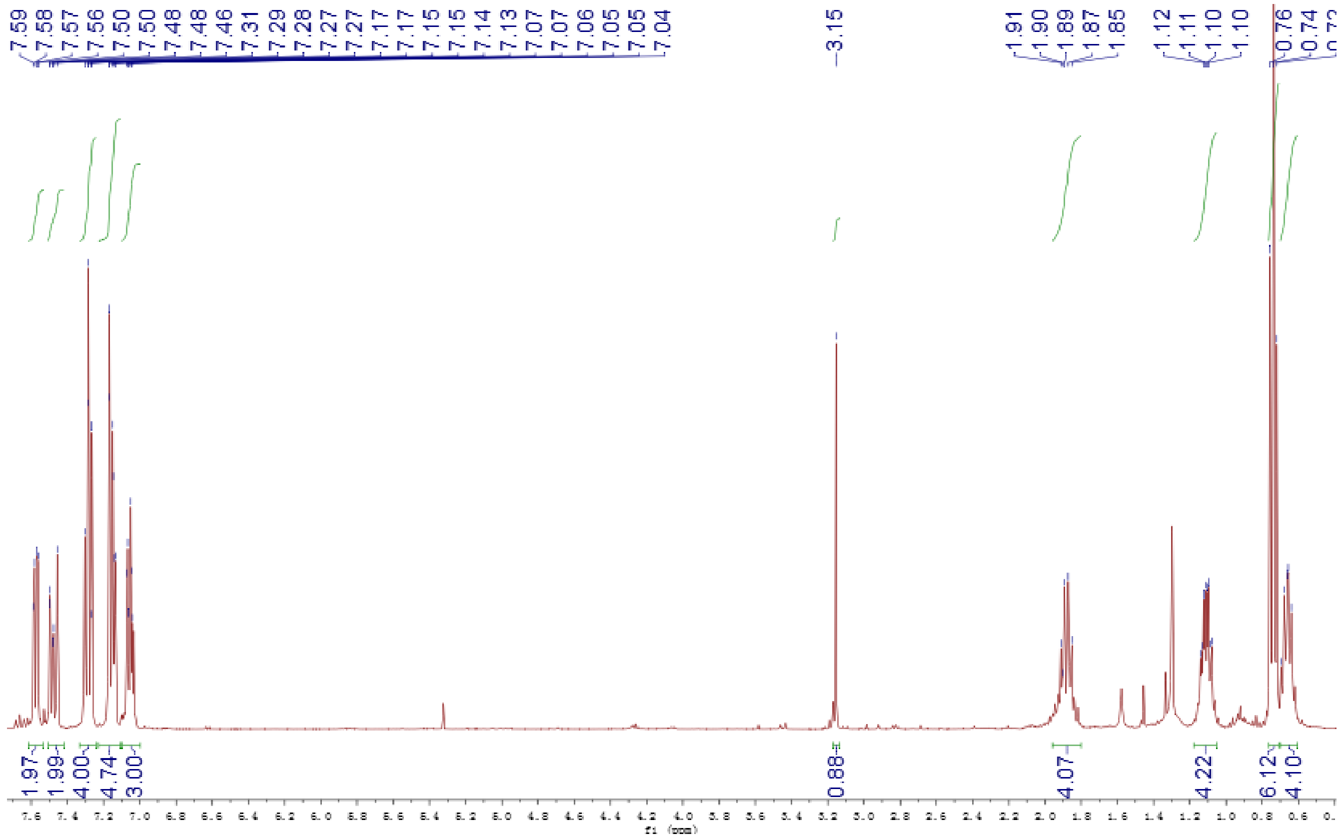

Figure S23. ^{1}H NMR spectrum of **11** (400 MHz, $CDCl_3$).

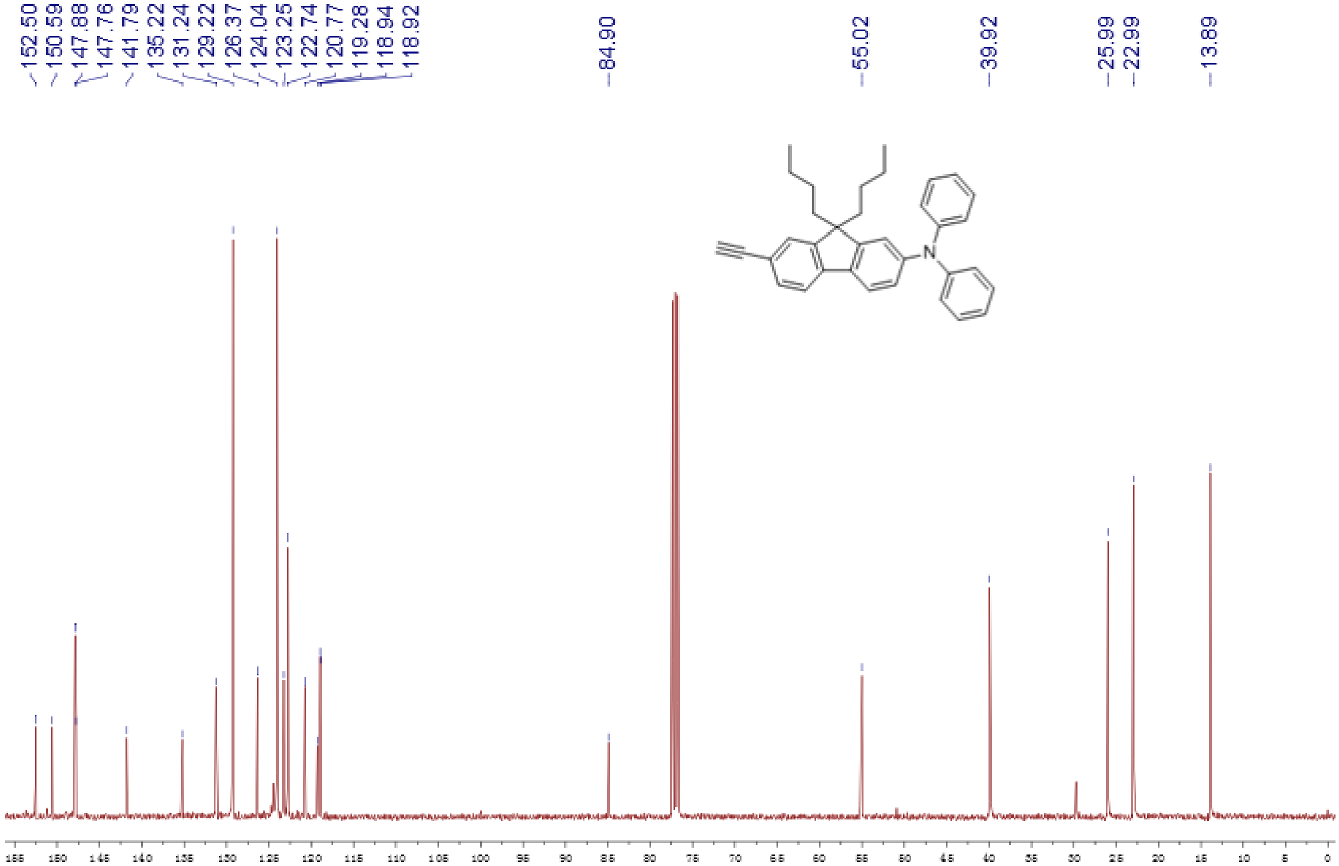

Figure S24. ^{13}C NMR spectrum of **11** (101 MHz, CDCl$_3$).

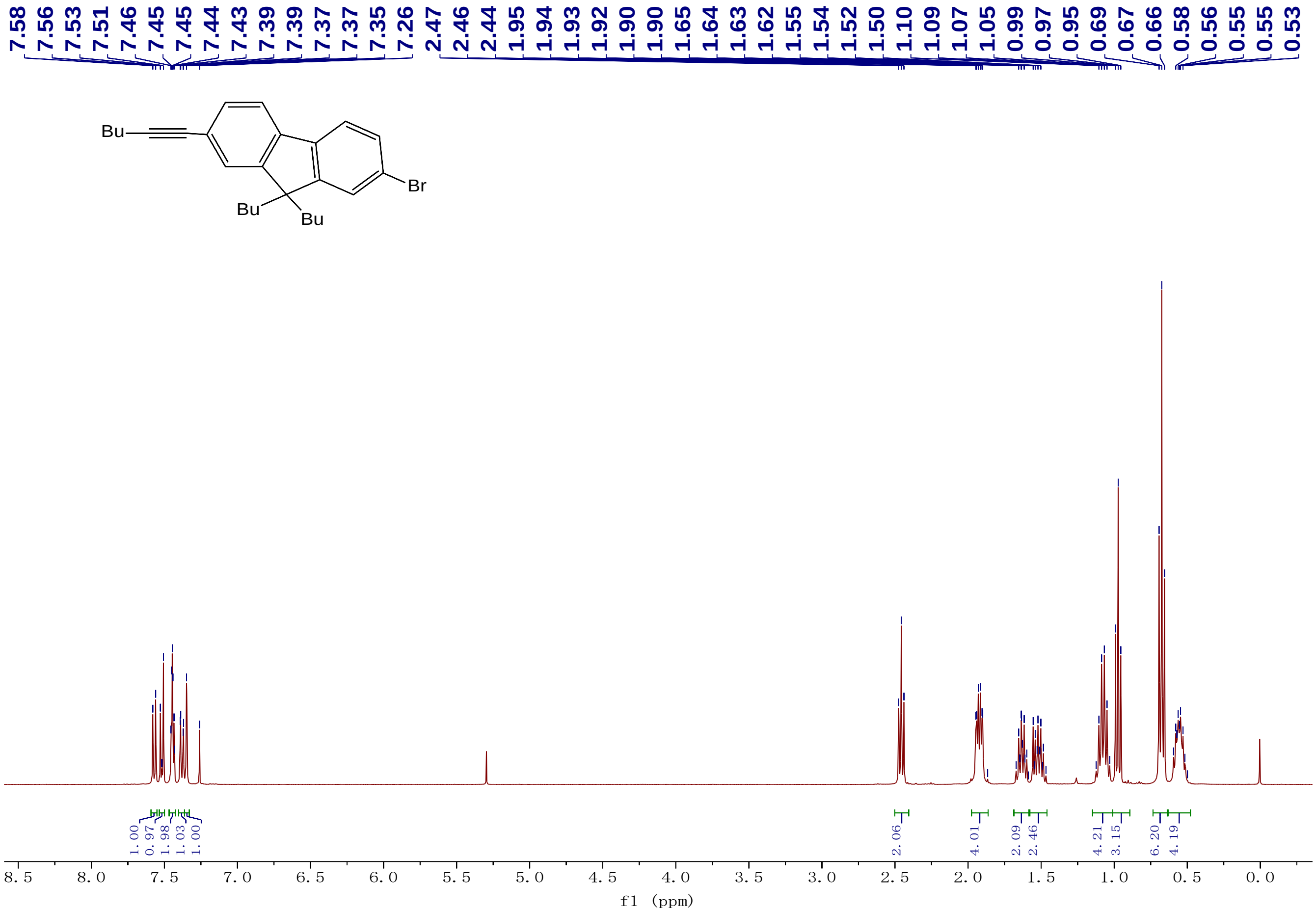

Figure S25. ^{1}H NMR spectrum of **12** (400 MHz, CDCl$_3$).

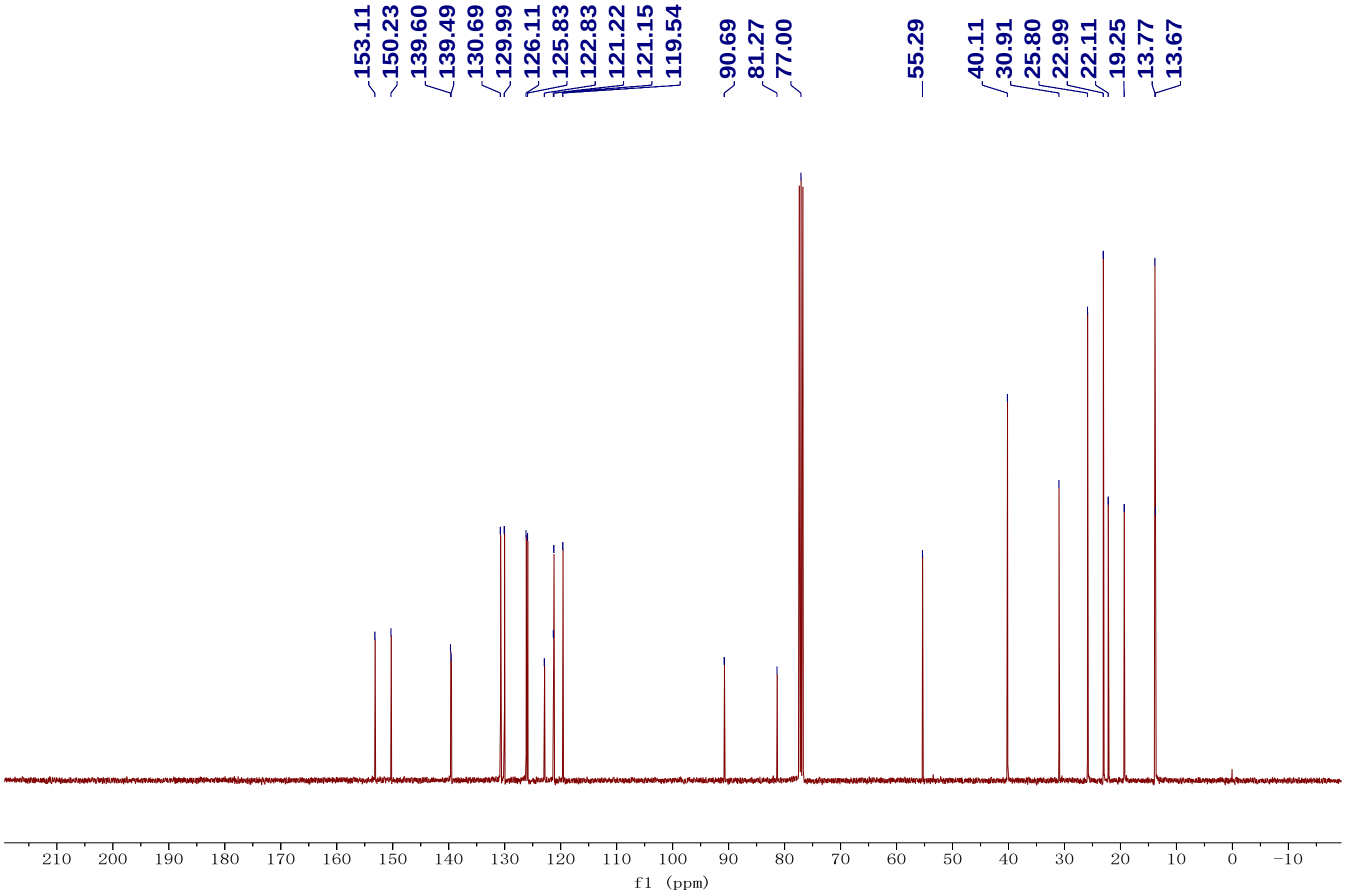

Figure S26. ^{13}C NMR spectrum of **12** (101 MHz, $CDCl_3$).

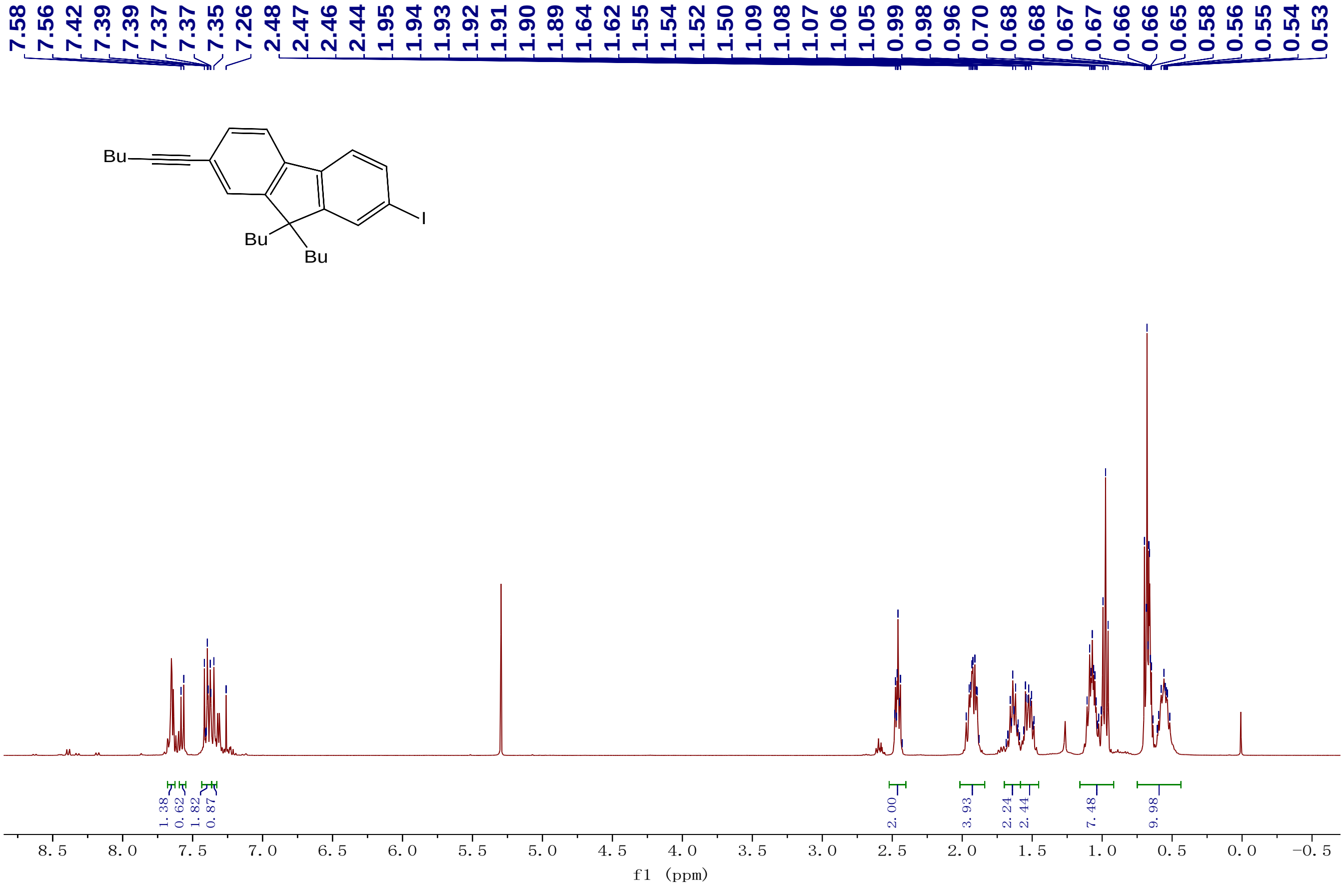

Figure S27. ^{1}H NMR spectrum of **13** (400 MHz, $CDCl_3$).

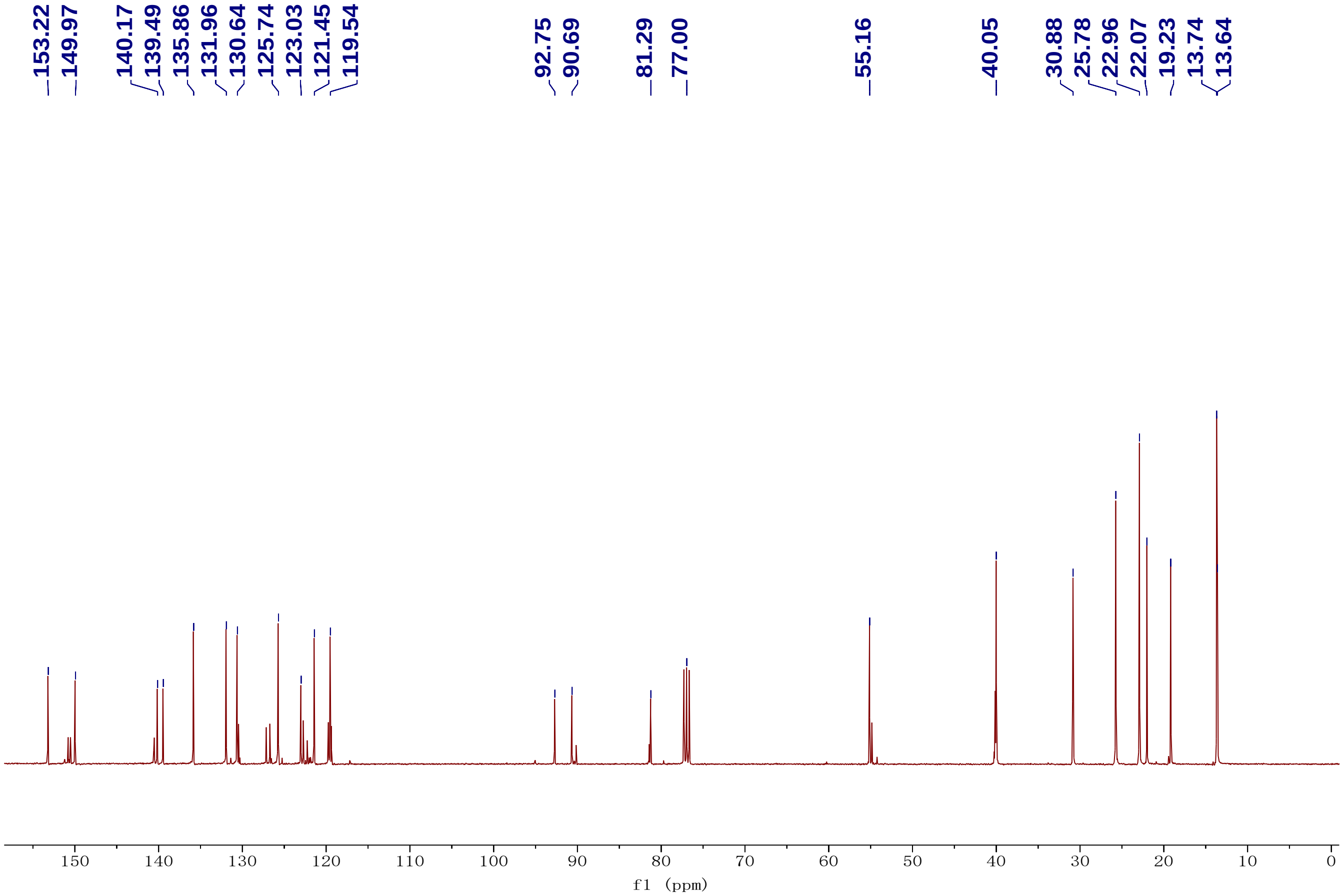

Figure S28. ^{13}C NMR spectrum of **13** (101 MHz, CDCl$_3$).

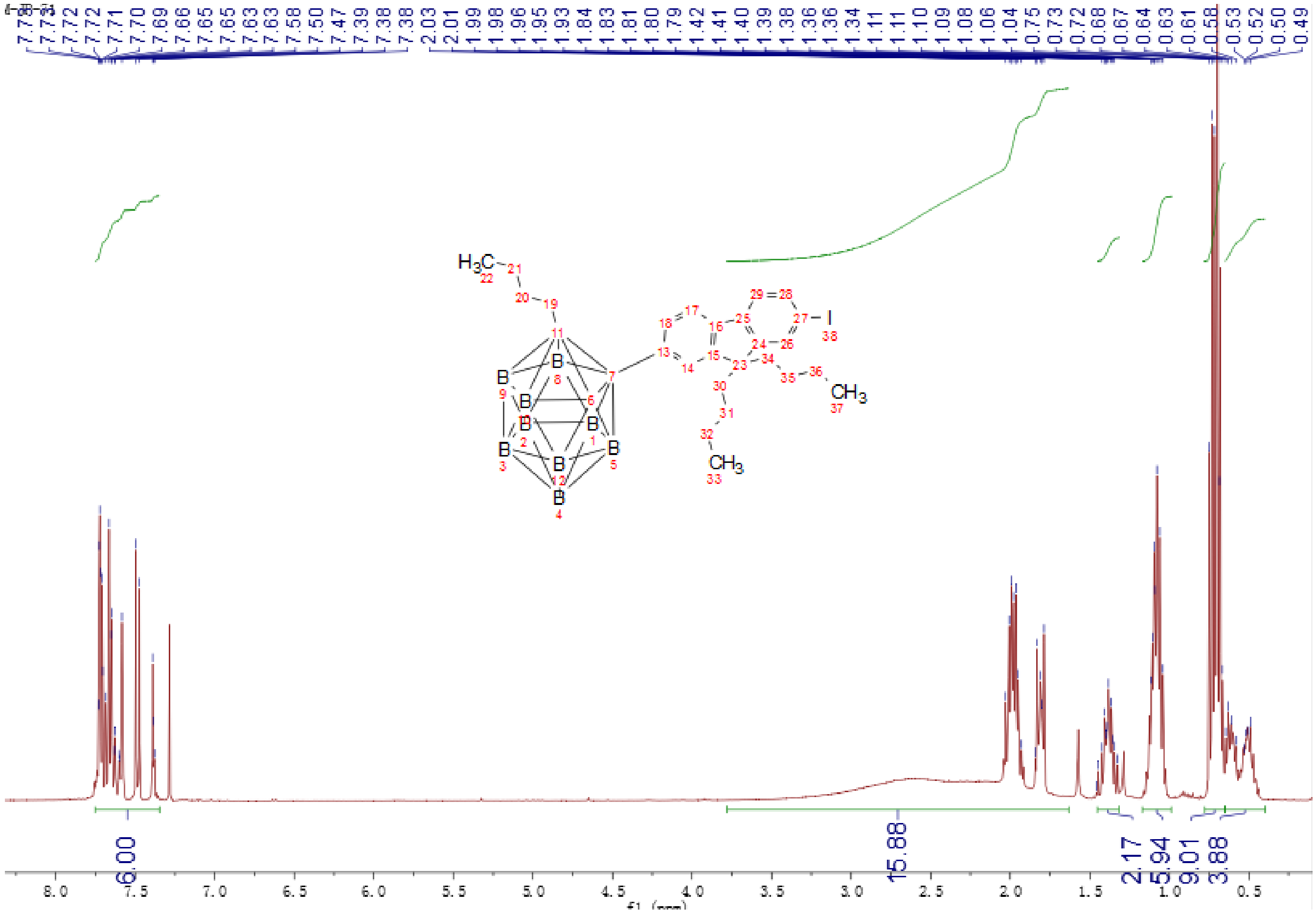

Figure S29. ^{1}H NMR spectrum of **14** (400 MHz, $CDCl_3$).

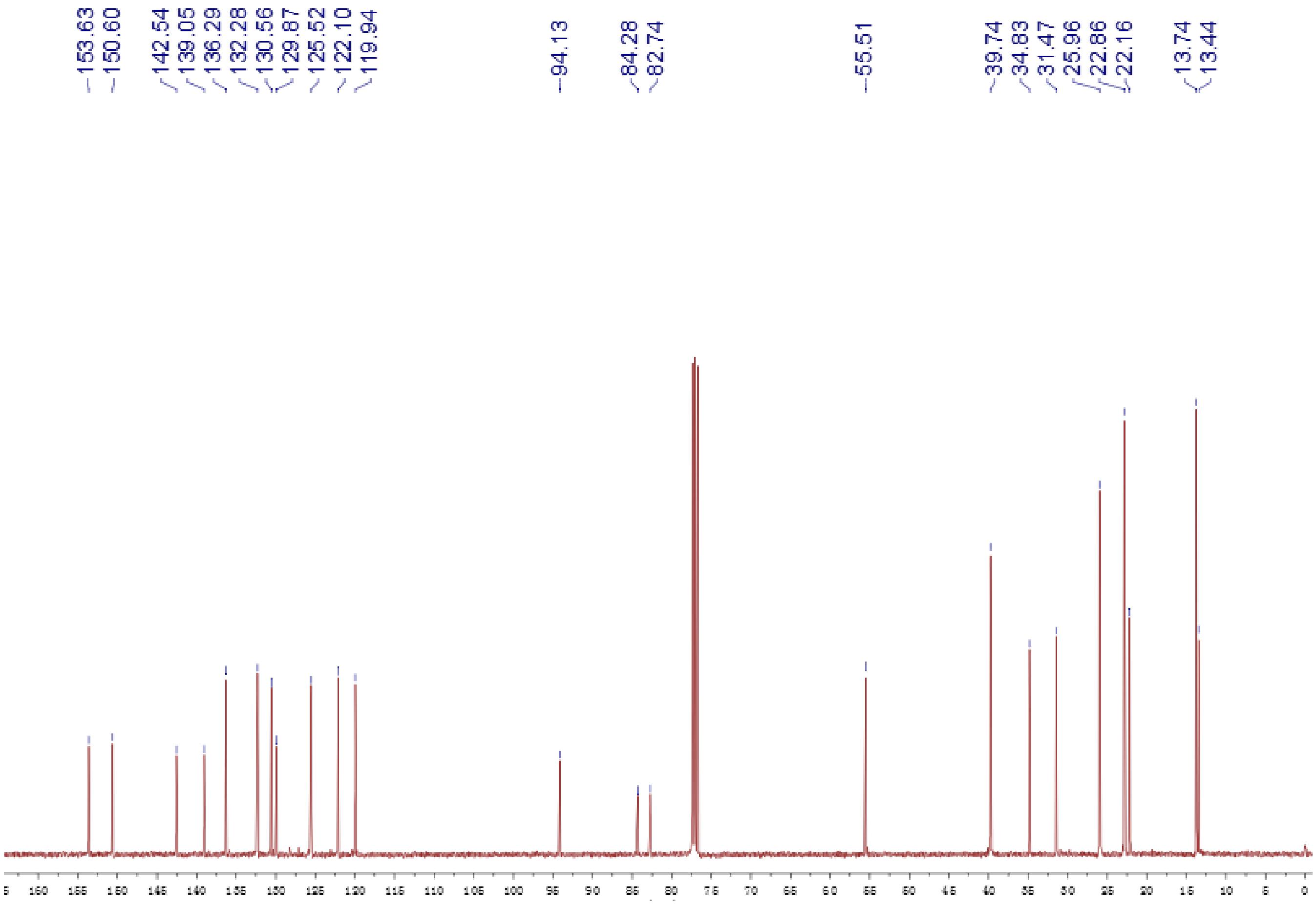

Figure S30. ^{13}C NMR spectrum of **14** (101 MHz, $CDCl_3$).

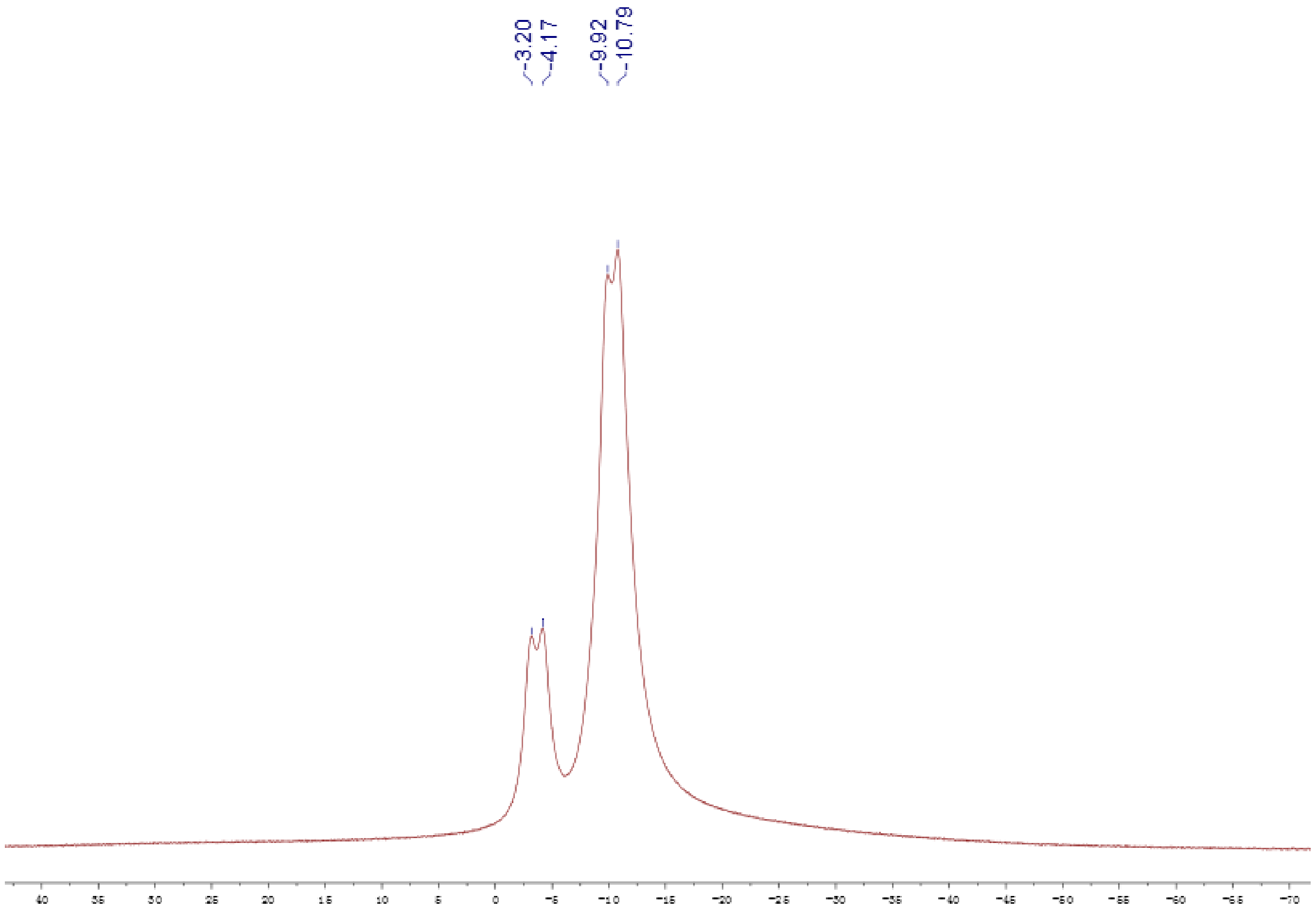

Figure S31. ^{11}B NMR spectrum of **14** (128 MHz, $CDCl_3$).

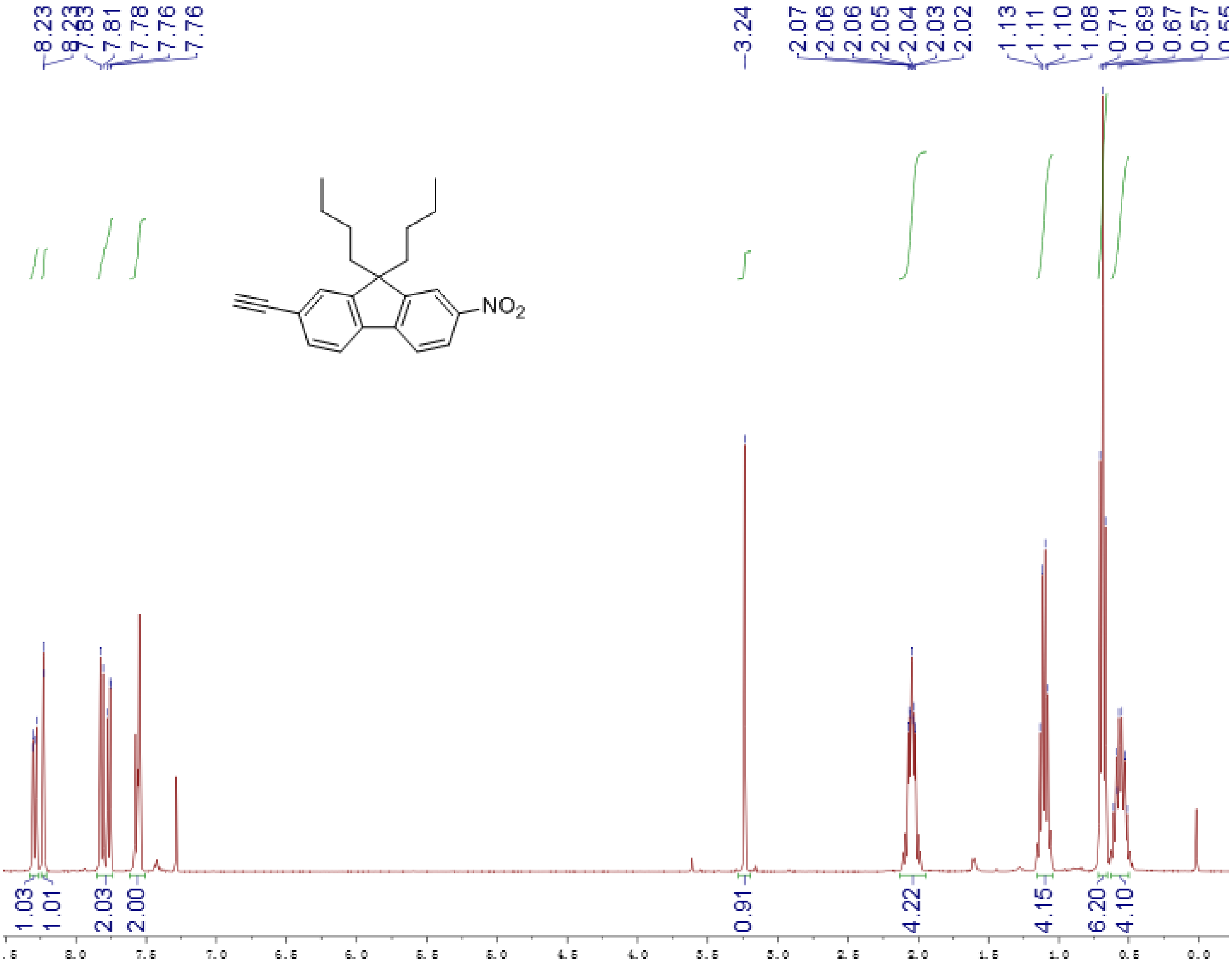

Figure S32. ^{1}H NMR spectrum of **15** (400 MHz, $CDCl_3$).

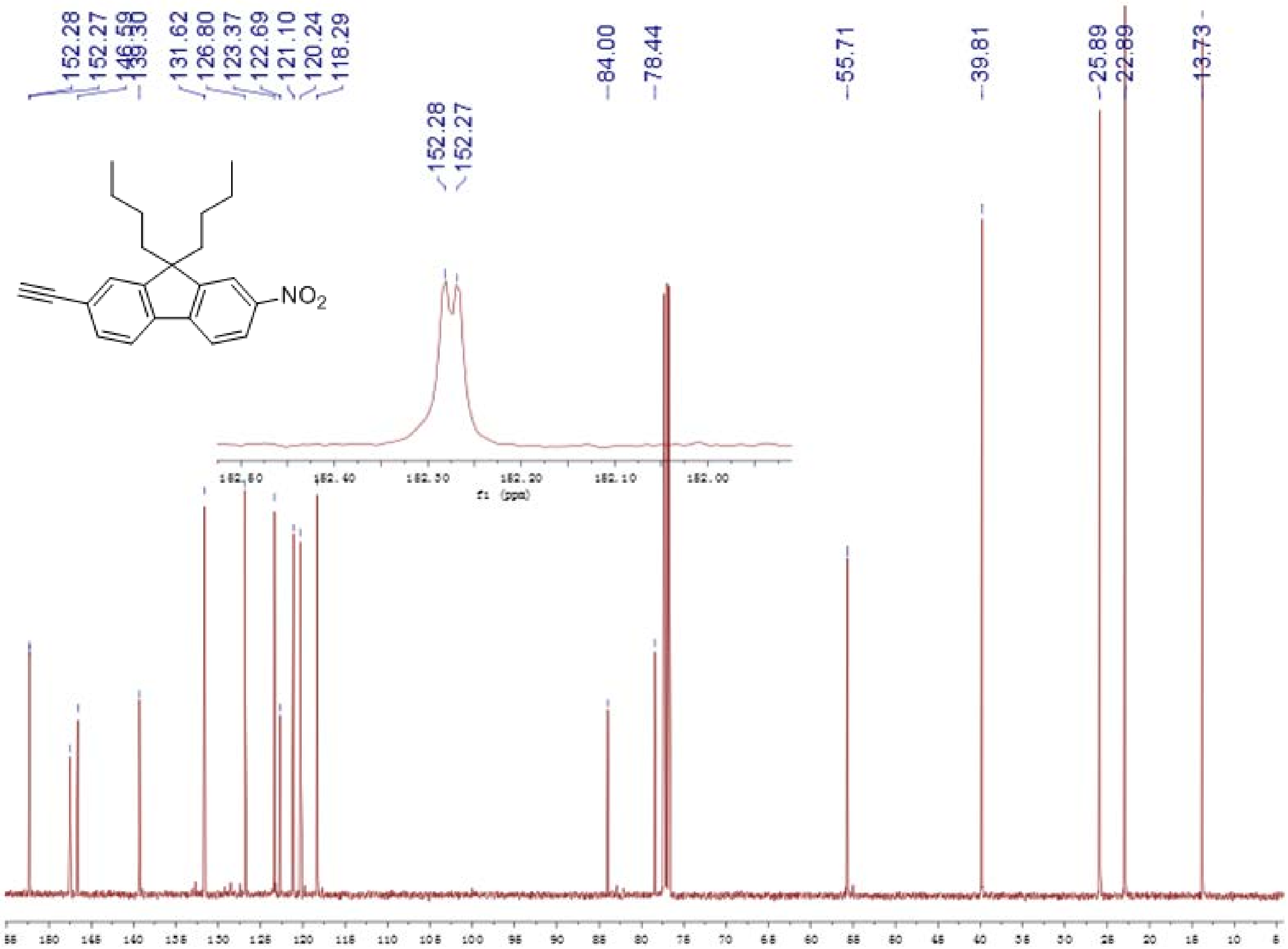

Figure S33. ^{13}C NMR spectrum of **15** (101 MHz, CDCl$_3$).

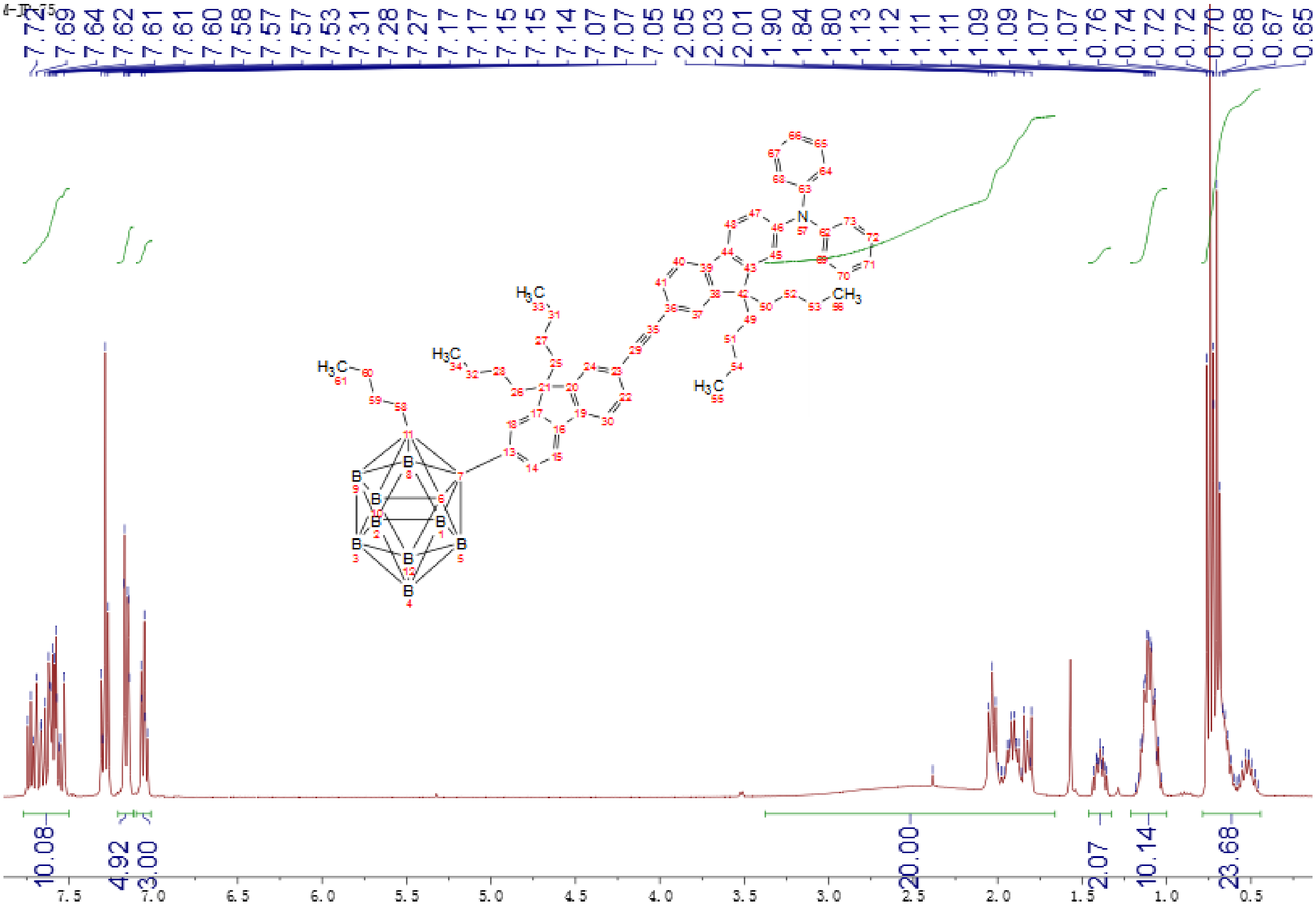

Figure S34. ^{1}H NMR spectrum of **16** (400 MHz, $CDCl_3$).

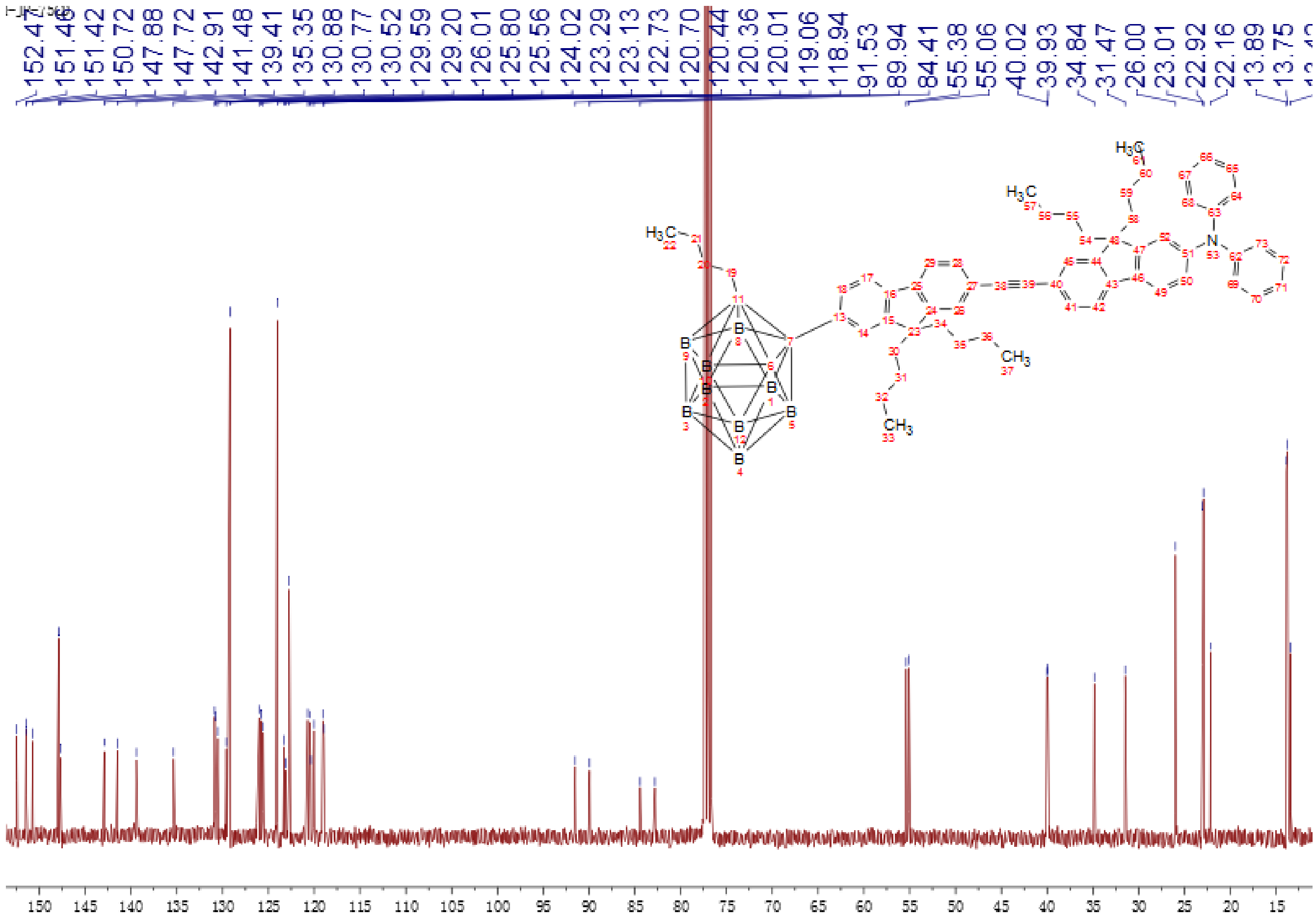

Figure S35. ^{13}C NMR spectrum of **16** (101 MHz, CDCl$_3$).

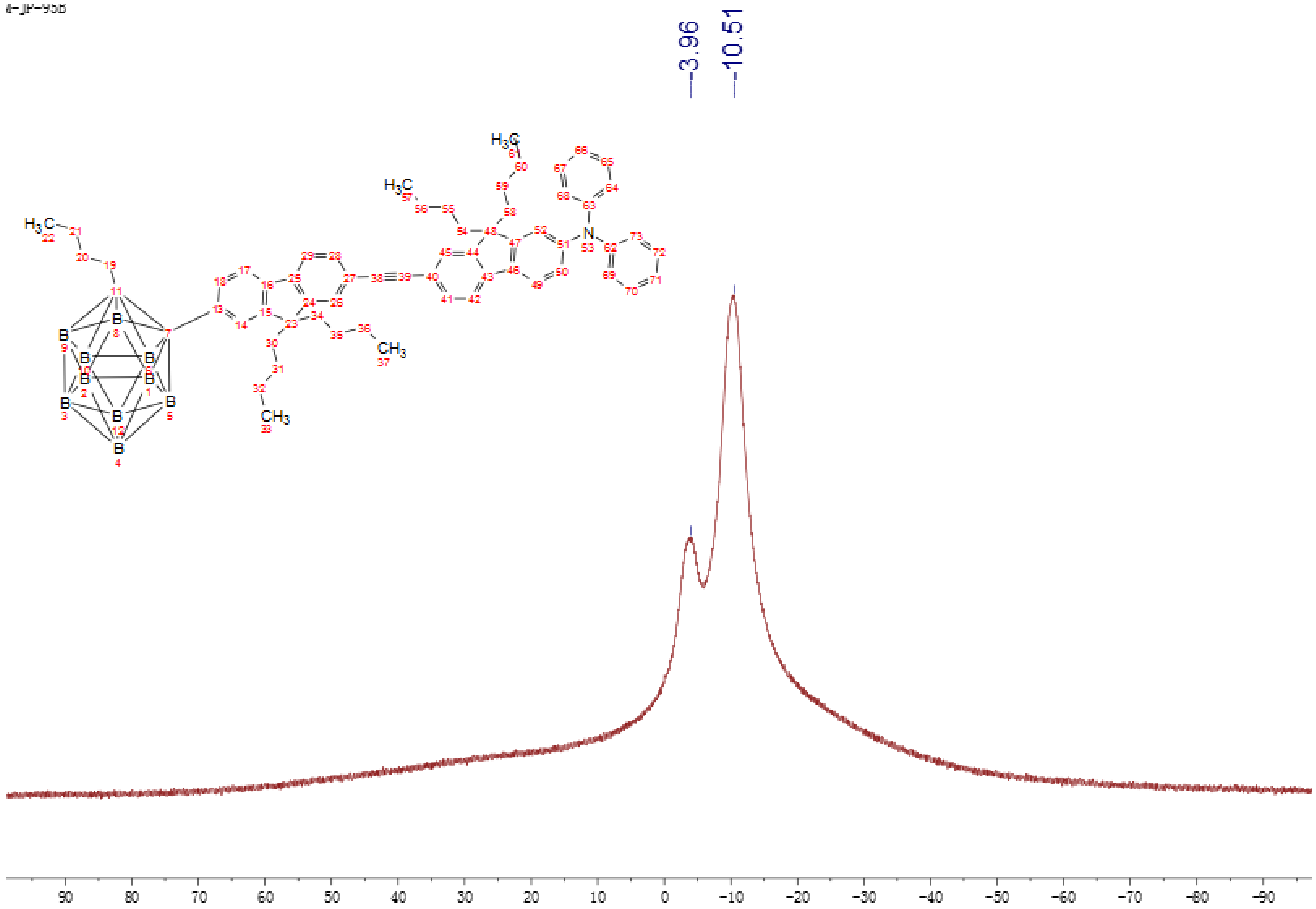

Figure S36. ^{11}B NMR spectrum of **16** (128 MHz, CDCl$_3$).

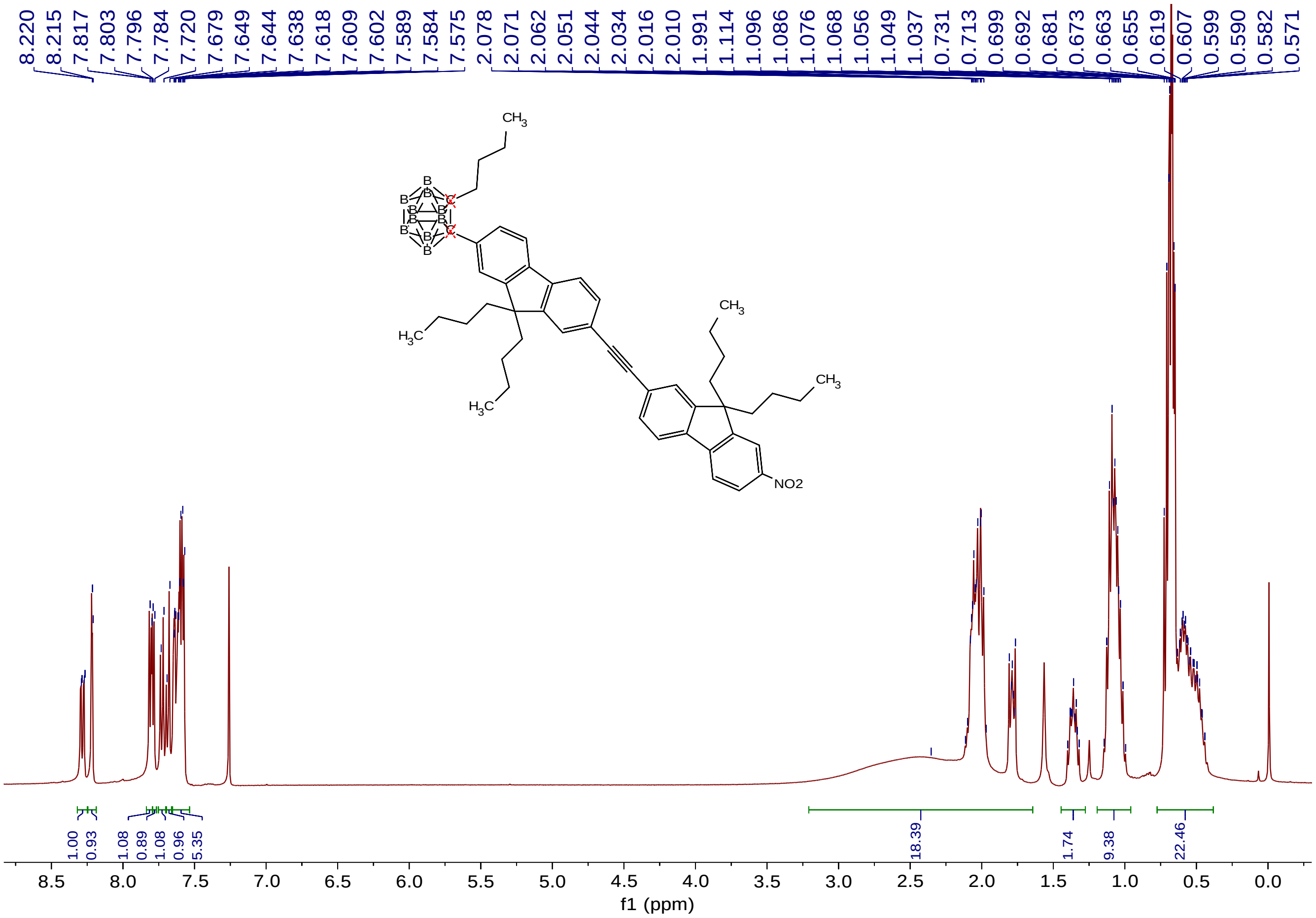

Figure S37. ^{1}H NMR spectrum of **17** (400 MHz, $CDCl_3$).

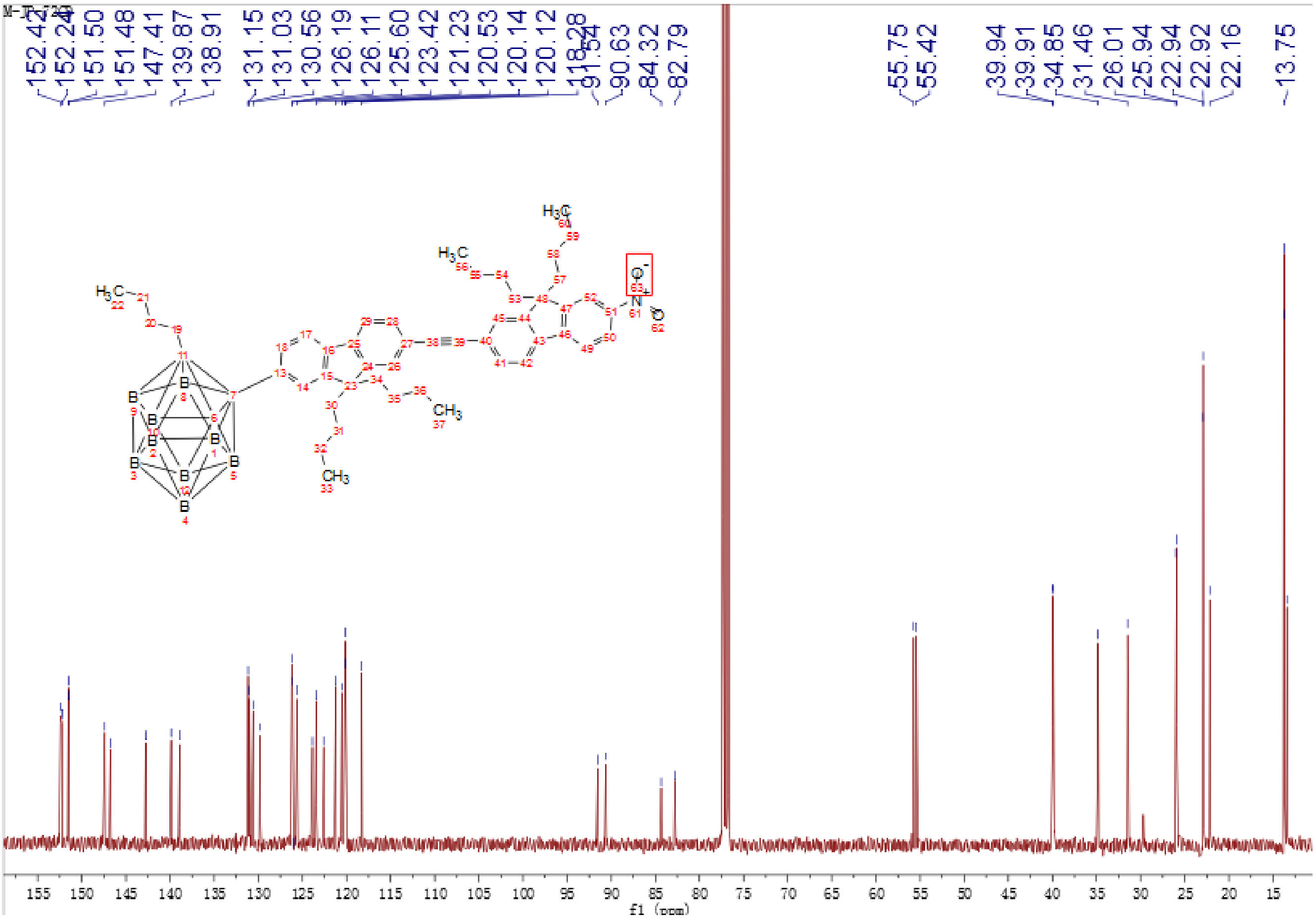

Figure S38. ^{13}C NMR spectrum of **17** (101 MHz, $CDCl_3$).

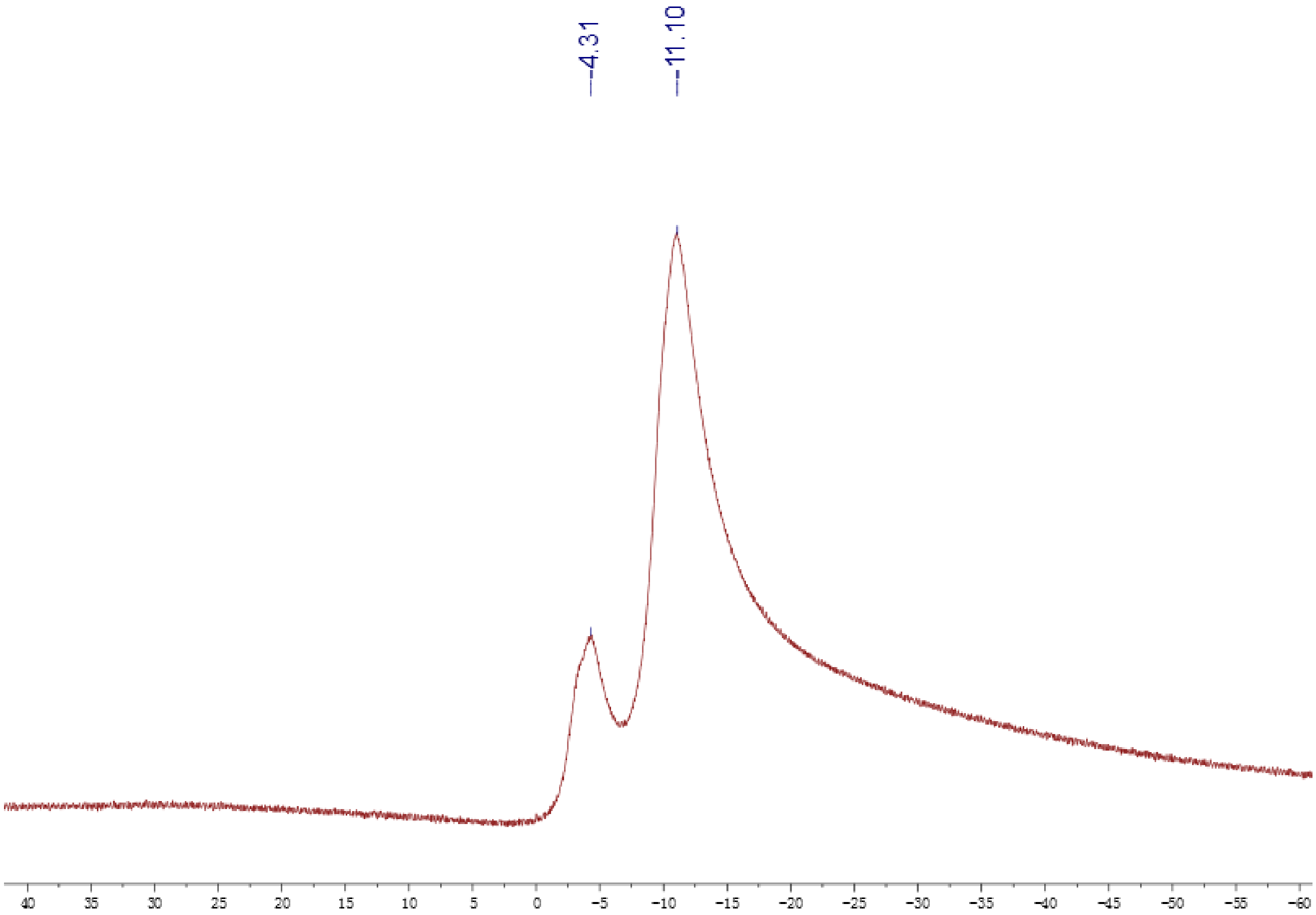

Figure S39. ^{11}B NMR spectrum of **17** (128 MHz, $CDCl_3$).

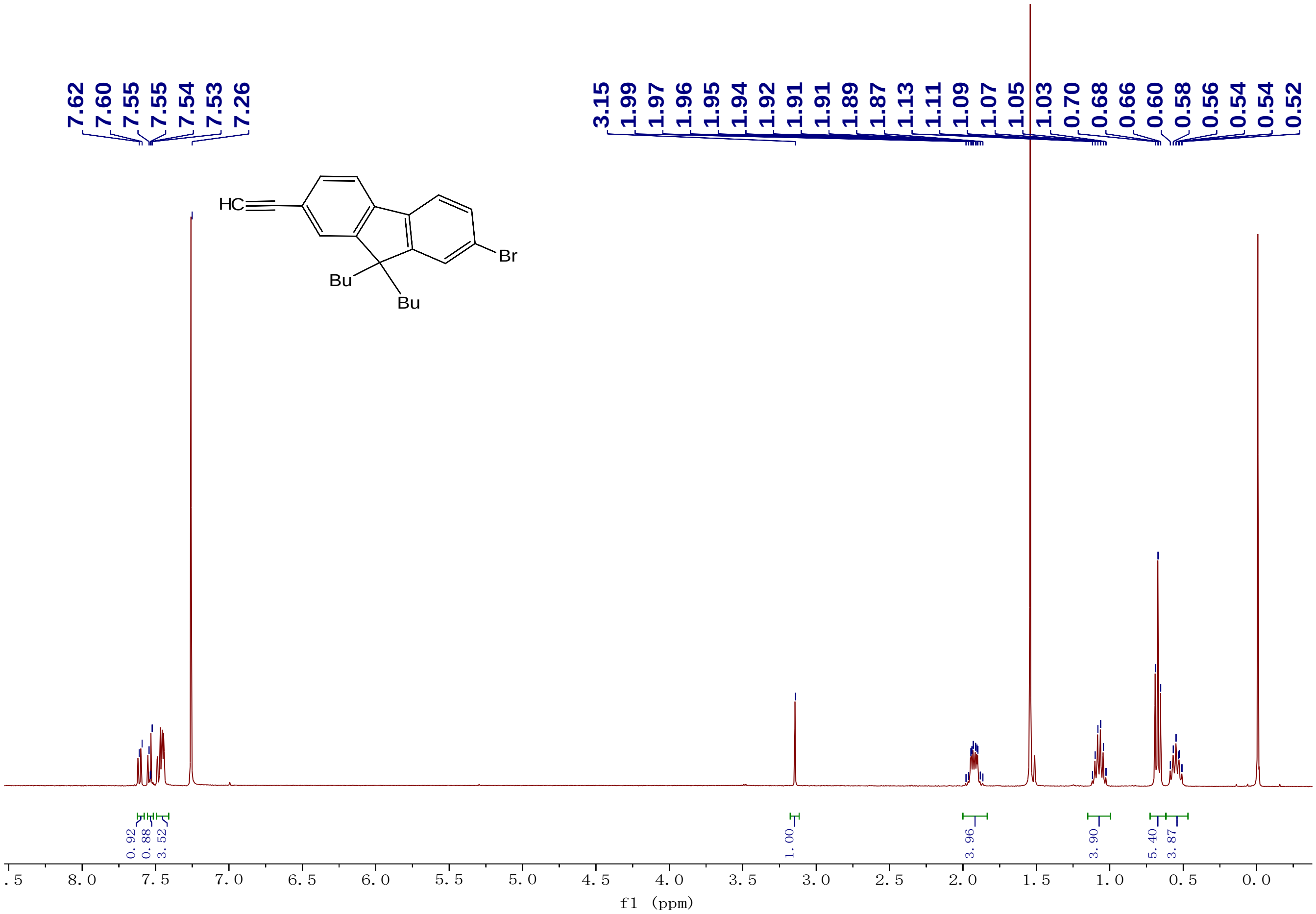

Figure S40. ^{1}H NMR spectrum of **18** (400 MHz, CDCl$_3$).

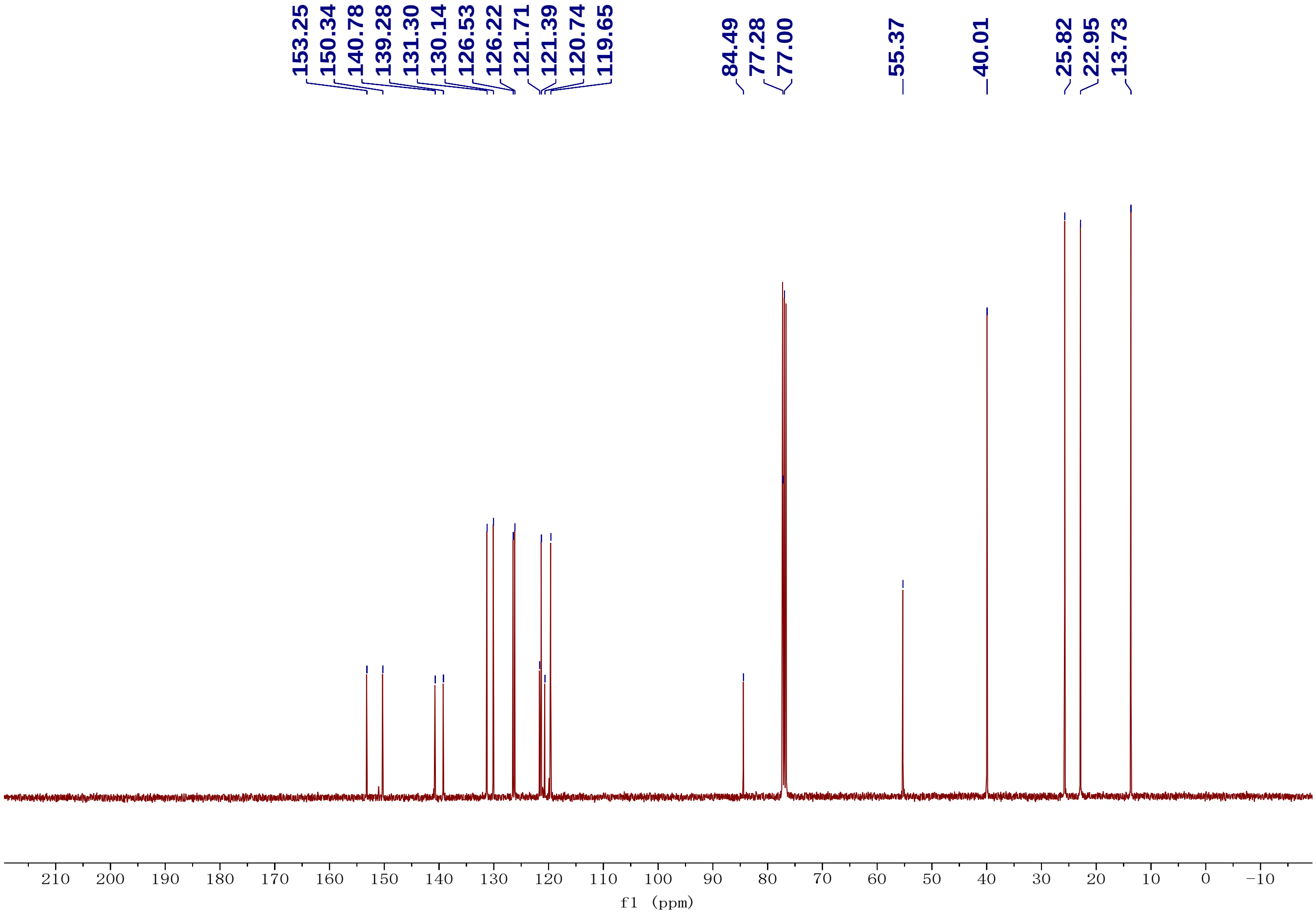

Figure S41. ^{13}C NMR spectrum of **18** (101 MHz, $CDCl_3$).

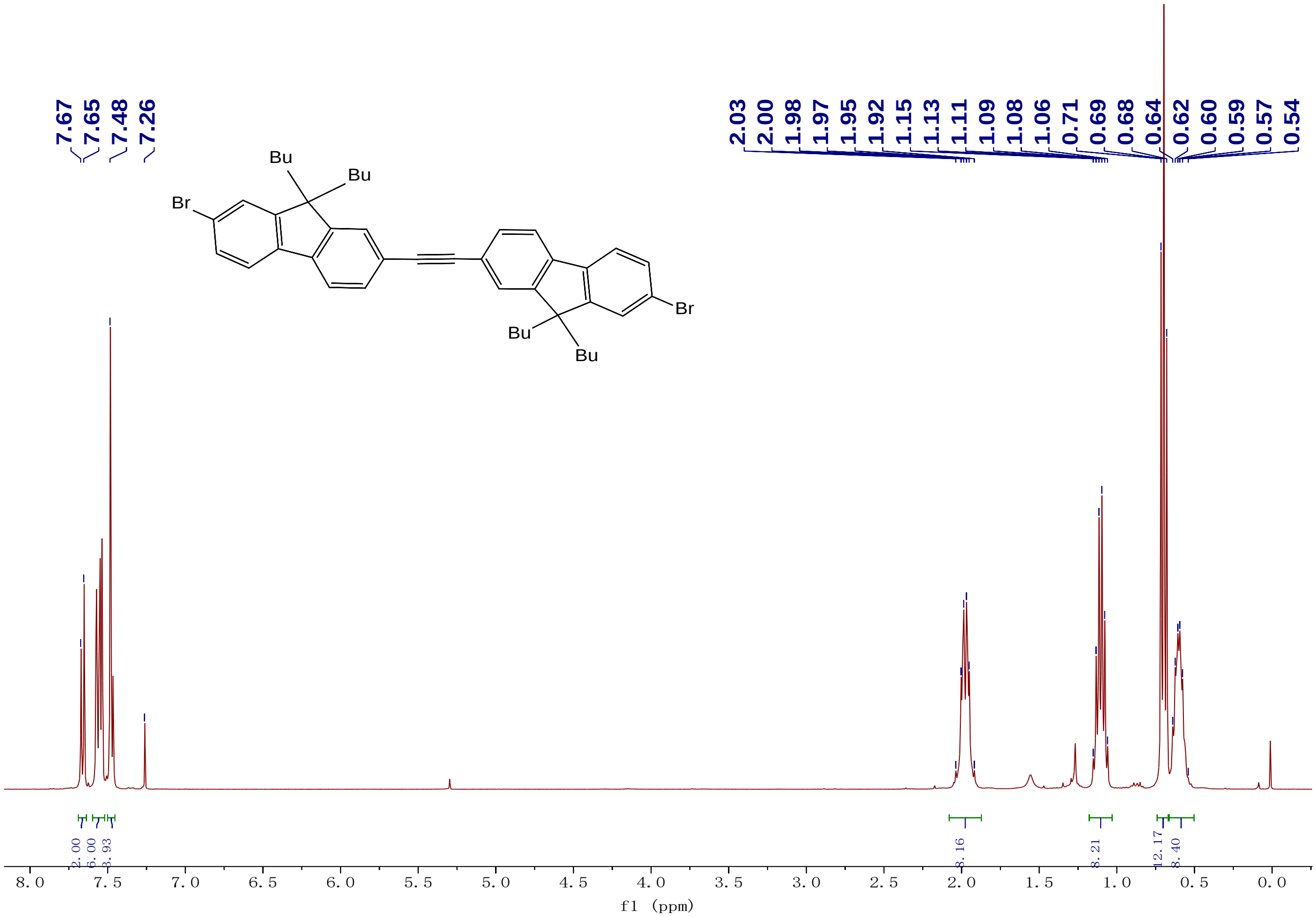

Figure S42. ^{1}H NMR spectrum of **19** (400 MHz, $CDCl_3$).

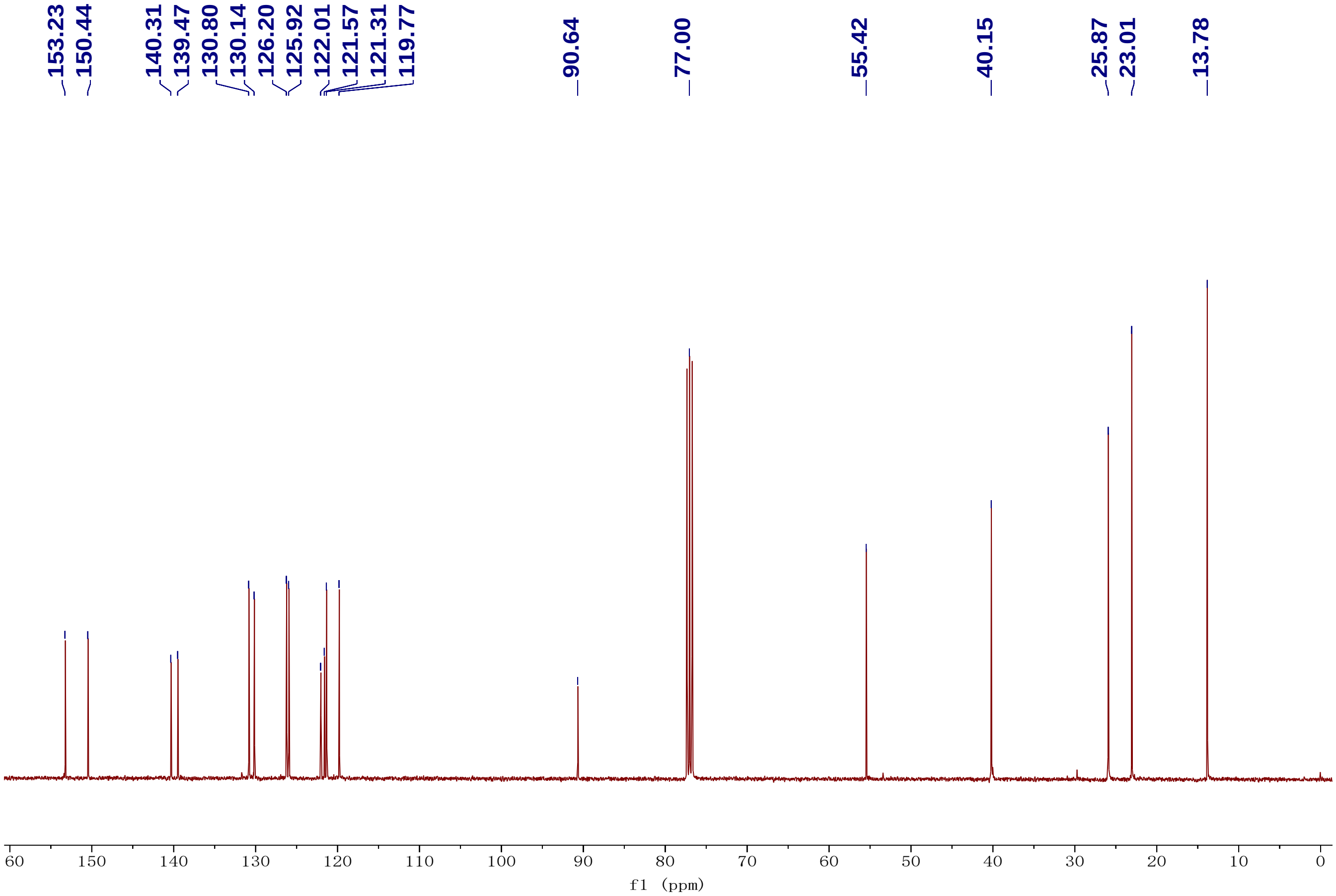

Figure S43. ^{13}C NMR spectrum of **19** (101 MHz, $CDCl_3$).

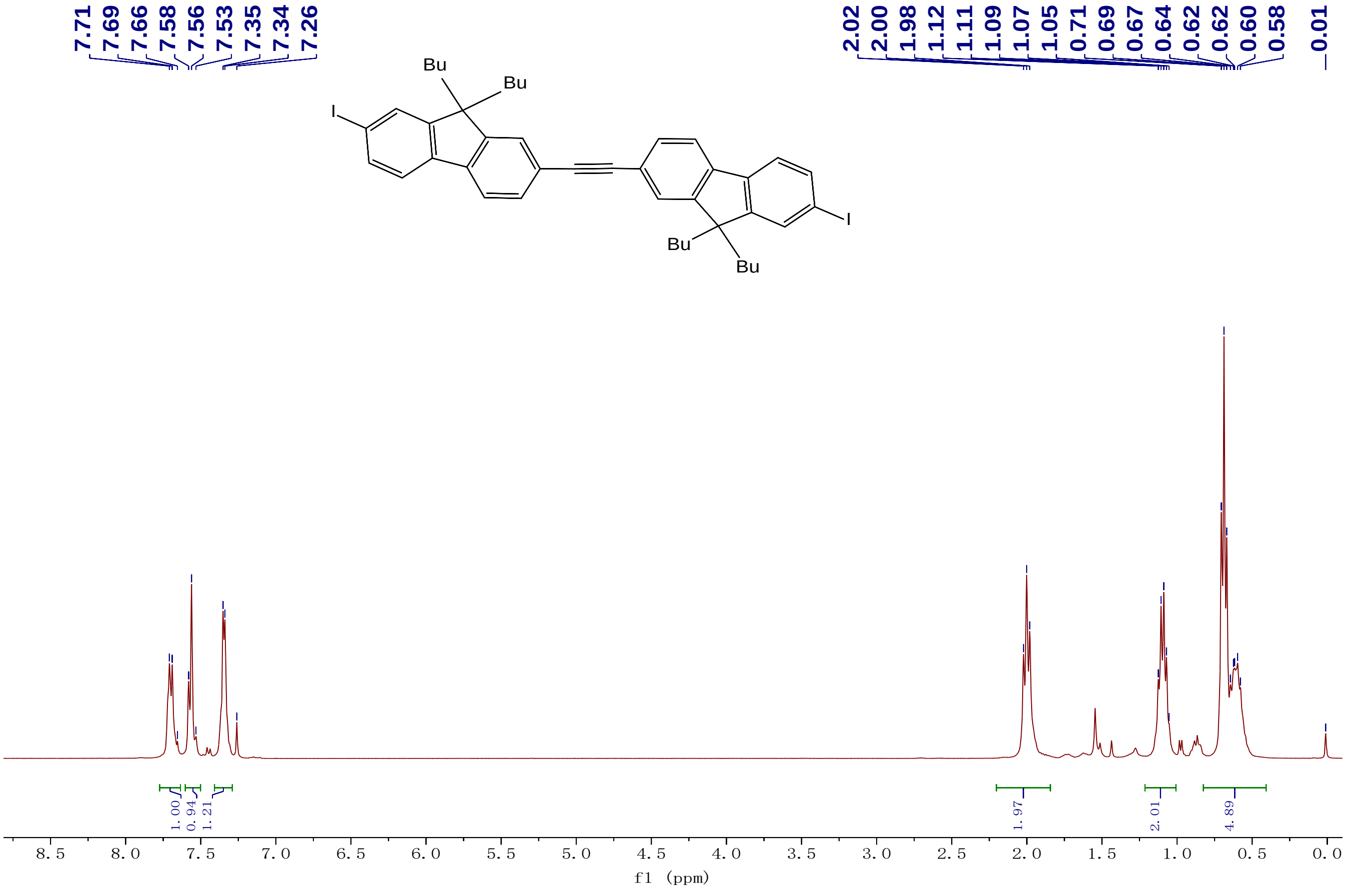

Figure S44. ^{1}H NMR spectrum of **20** (400 MHz, CDCl$_3$).

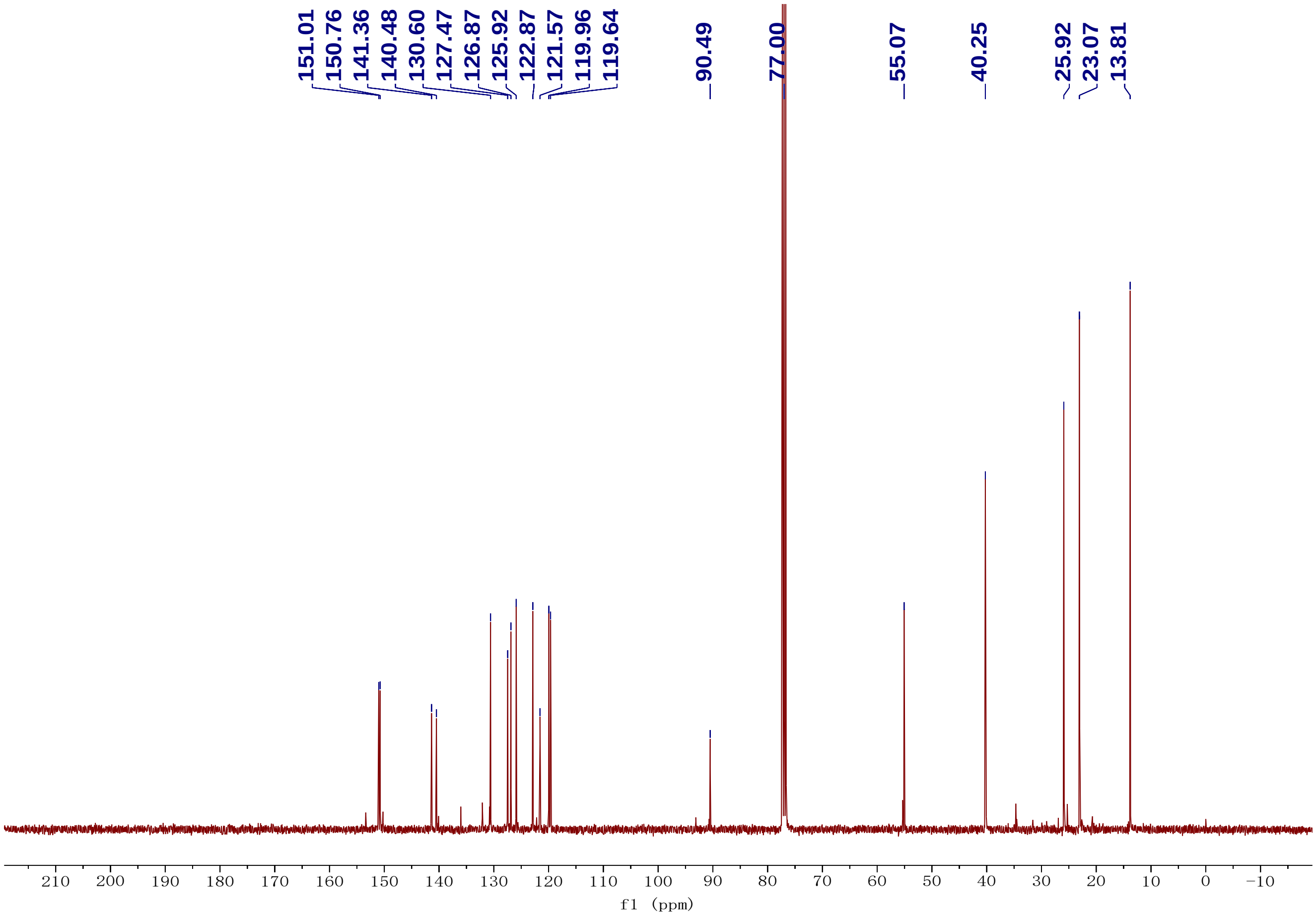

Figure S45. ^{13}C NMR spectrum of **20** (101 MHz, $CDCl_3$).

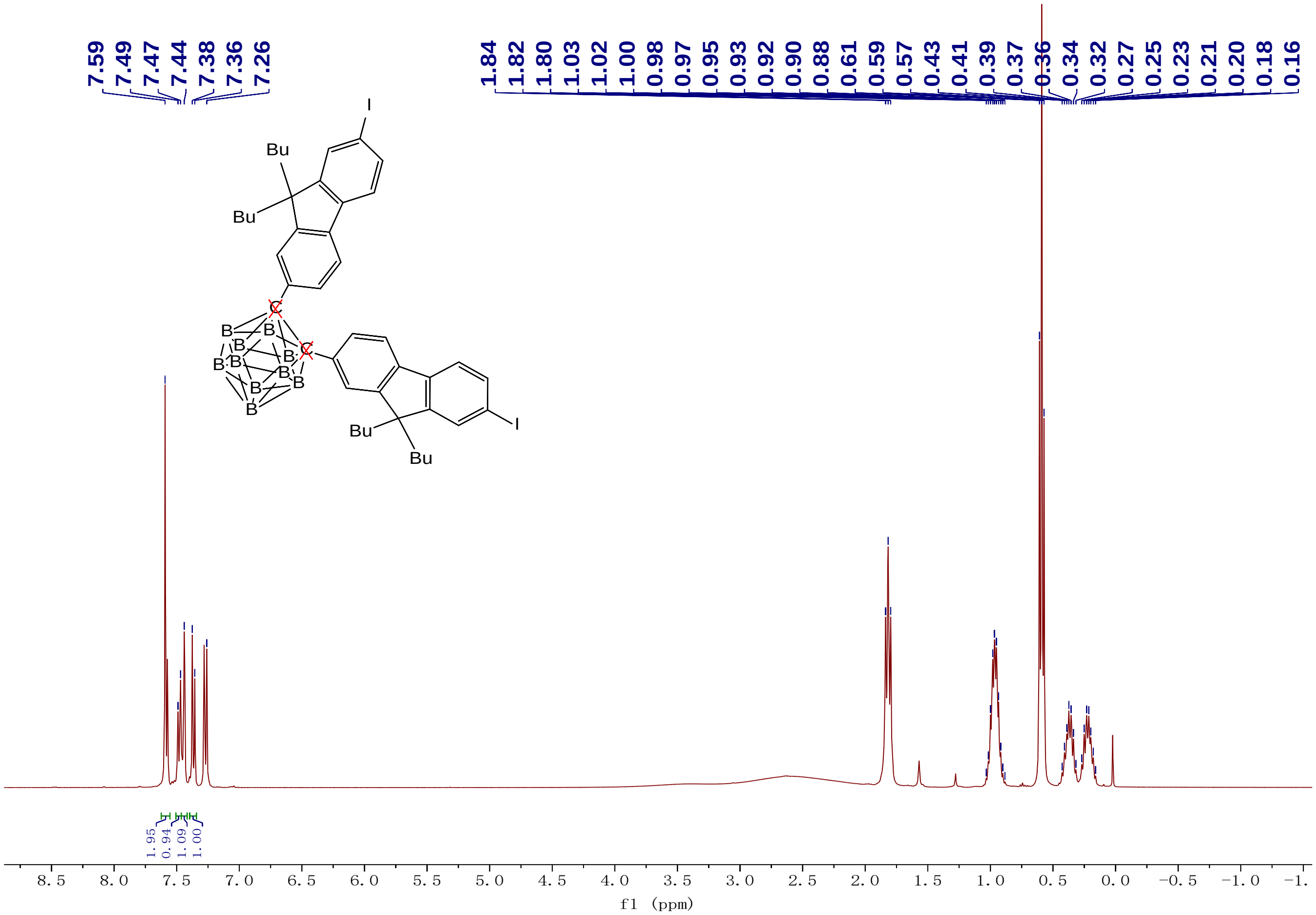

Figure S46. ^{1}H NMR spectrum of **21** (400 MHz, $CDCl_3$).

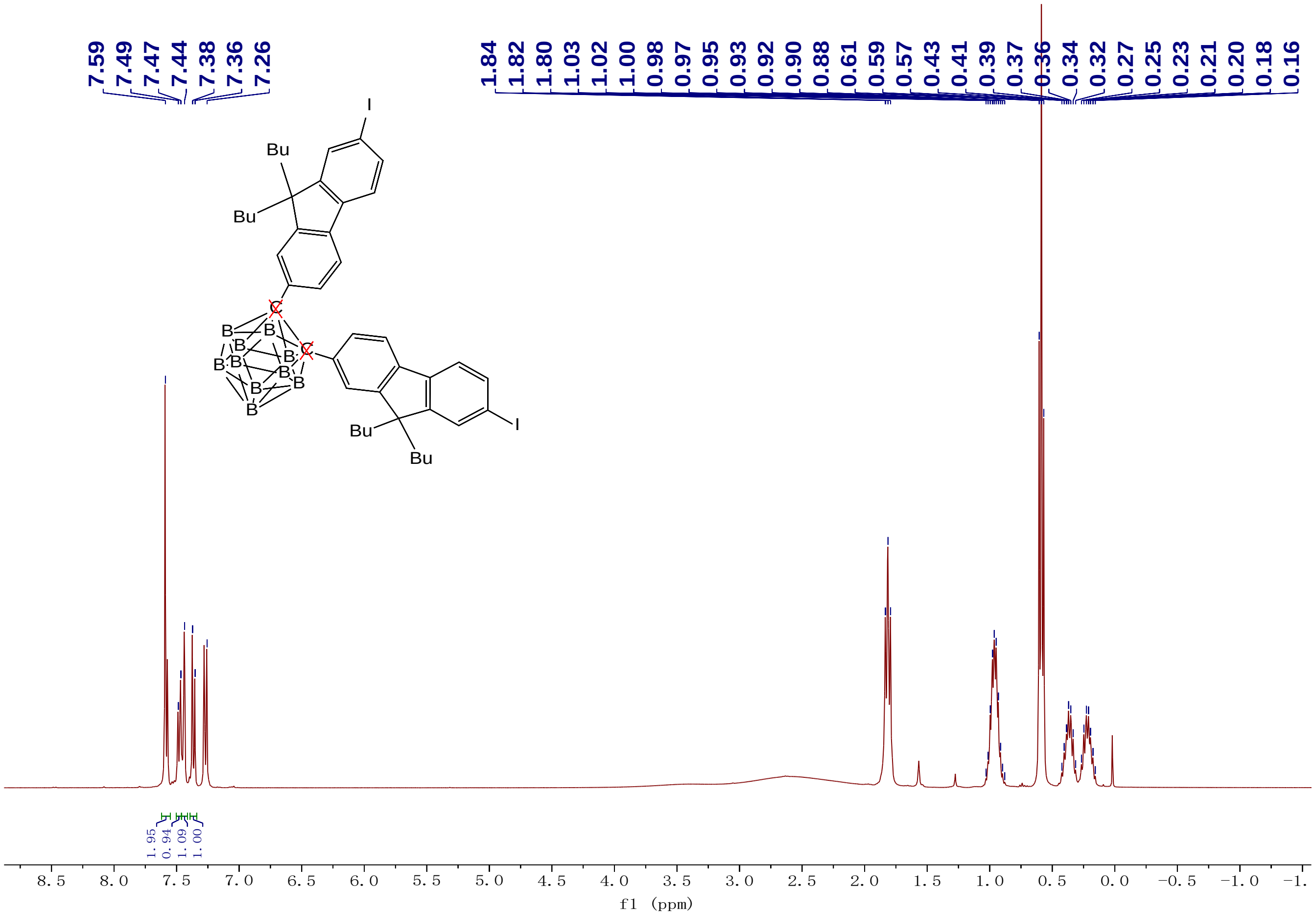

Figure S47. ^{13}C NMR spectrum of **21** (101 MHz, CDCl$_3$).

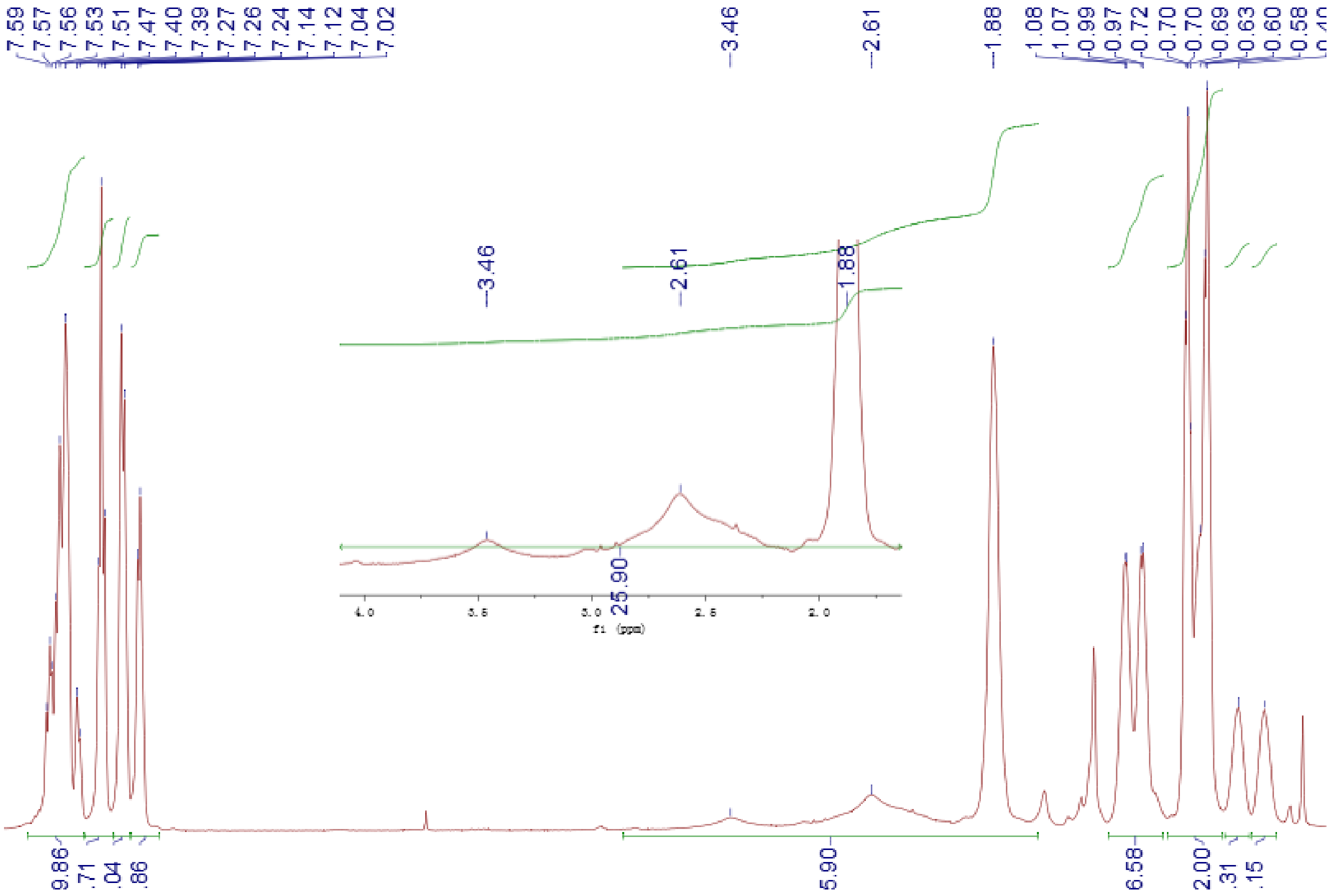

Figure S48. ^{1}H NMR spectrum of **22** (400 MHz, $CDCl_3$).

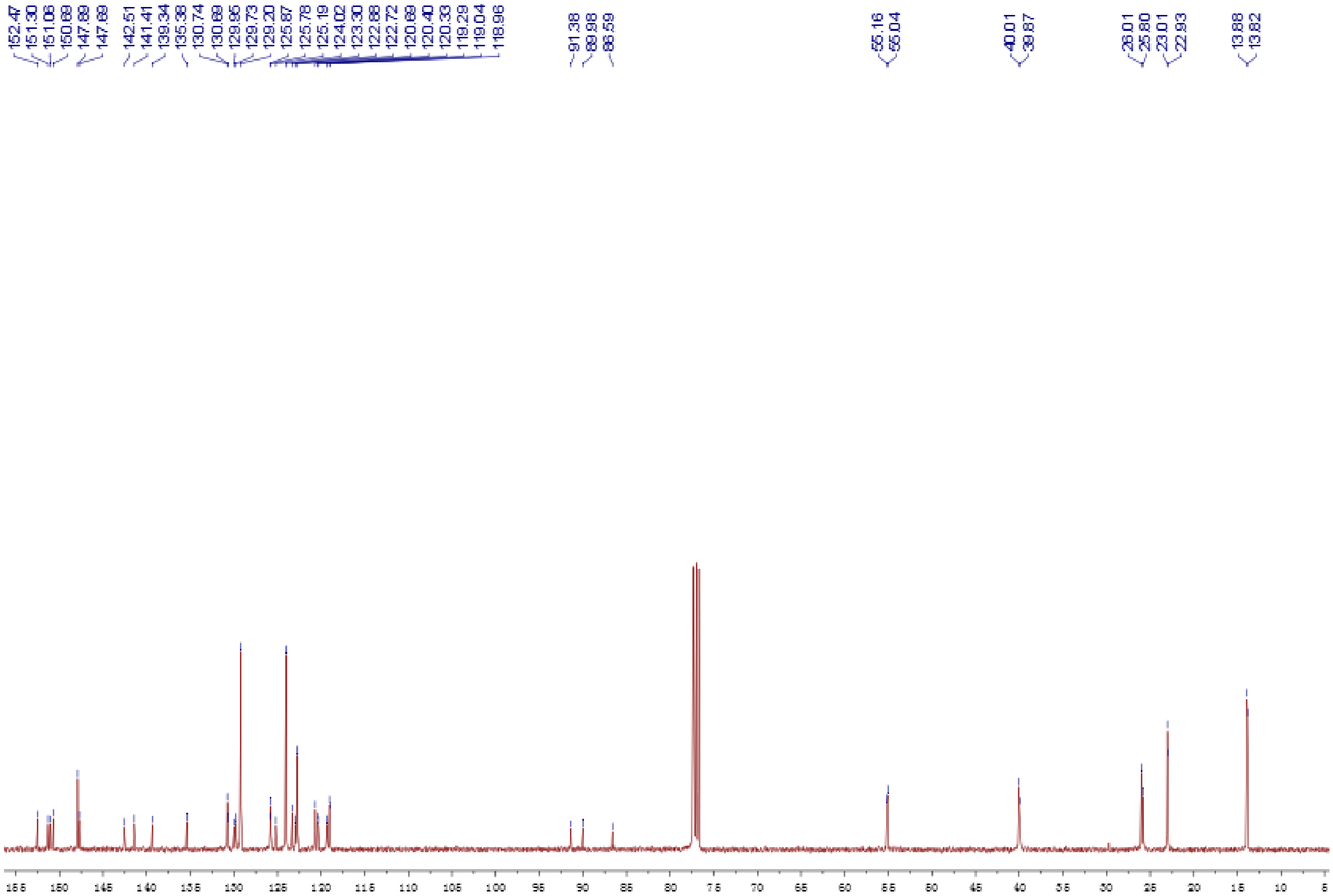

Figure S49. ^{13}C NMR spectrum of **22** (101 MHz, $CDCl_3$).

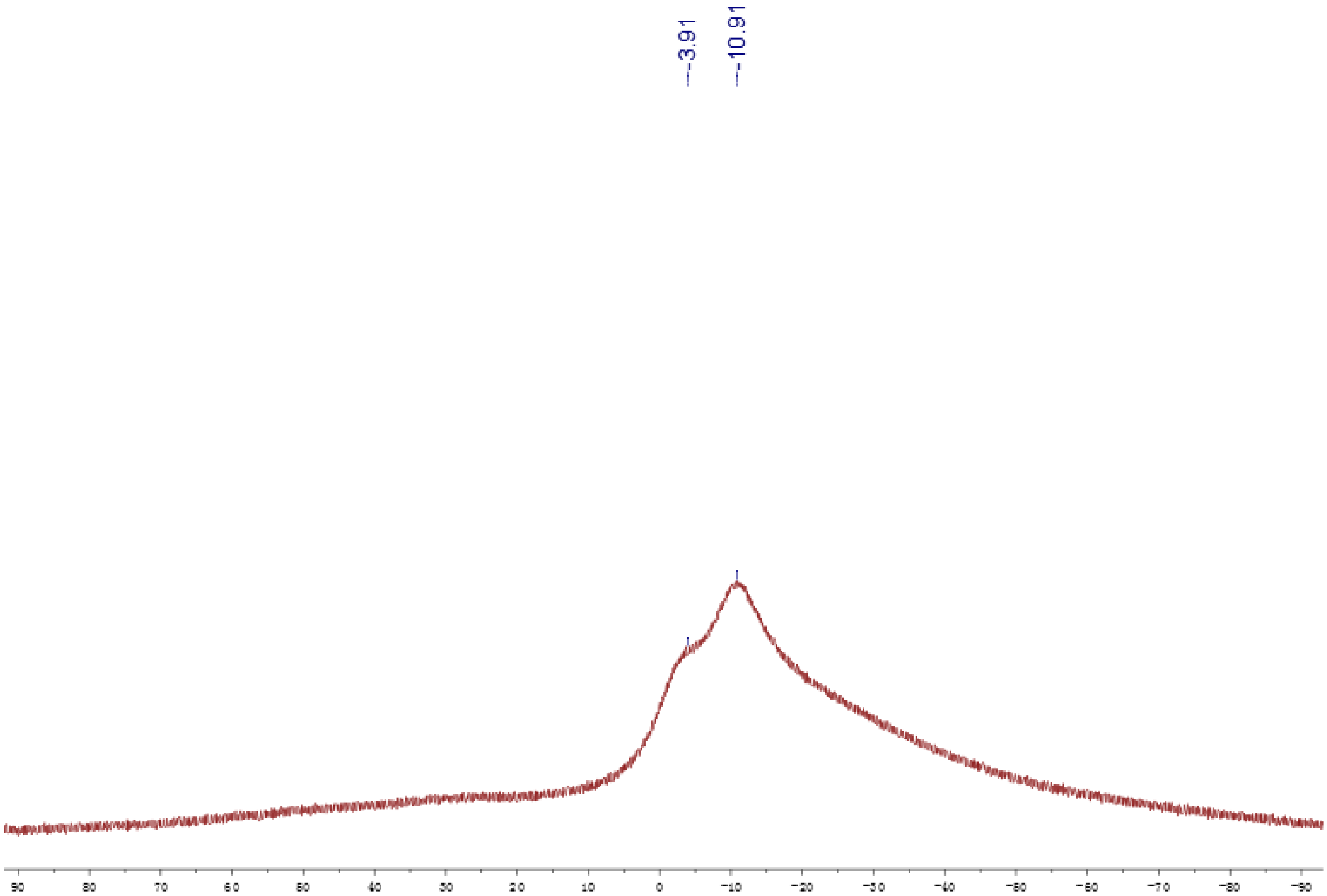

Figure S50. ^{11}B NMR spectrum of **22** (128 MHz, $CDCl_3$).

Crystallographic data

The crystal and refinement data for compounds **1, 4**-**8, 10**, **11** and **14** are summarized in Table 1. Crystals suitable for the X-ray structural analyses were grown from concentrated hexane (**1**, **4**, **5**, **14**), CH_2Cl_2/hexane (**6**, **8**), methanol (**7**), cyclohexane (**10**), and CCl_4 (**11**) solutions at 298 K. Suitable crystals were mounted on MicroMounts (MiTeGen) using Paratone-N oil (Hampton Research) and cooled rapidly to 150 K using an Oxford Cryosystems low-temperature device.[1] Intensity data for **1, 4, 5, 7, 8, 10, 11** and **14** were collected on an Agilent SuperNova CCD diffractometer using mirror-monochromated Cu-K_α radiation (λ = 1.54184 Å) and intensity data for **6** were collected on an Agilent XCalibur CCD diffractometer using graphite-monochromated Mo-K_α radiation (λ = 0.71073 Å). N_t (total) reflections were measured by using omega scans and were reduced to N_o unique reflections, with $F_o > 2\sigma(F_o)$ being considered to be observed. Semi-empirical absorption corrections based on symmetry-equivalent and repeat reflections were applied.[2] The structures were solved using direct methods and observed reflections were used in least-squares refinement on F^2, with anisotropic thermal parameters refined for non-hydrogen atoms. Hydrogen atoms were constrained in calculated positions and refined with a riding model. Programs used were CrysAlisPro[3] (control and integration), and SHELXS-97,[4] SHELXL-2014[5] and Olex2[6] (structure solution and refinement and molecular graphics). Crystallographic data for the structural analyses have been deposited with the Cambridge Crystallographic Data Centre, CCDC numbers 1935869 (**1**), 1935868 (**4**), 1935870 (**5**), 1935871 (**6**), 1935866 (**7**), 1935865 (**8**), 1935872 (**10**), 1935873 (**11**), and 1935867 (**14**). Copies of this information may be obtained, free of charge, from the Director, CCDC, 12 Union Road, Cambridge CB2 1E2, UK (fax: +44-1223-336033; e-mail: deposit@ccdc.cam.ac.uk or www: http://www.ccdc.cam.ac.uk).

Variata. In **1**: rigid bond restraints were applied to phenyl group C21A – C26A.

In **5**: the structure was refined as a two-component twin, 0.628(5):0.372(5). Because only one of the C vertices is substituted, the other remains a C-H. It is commonplace in carborane structures that the C-H vertices are wrongly assigned (due to the minimal difference between B and C), so to ensure the assignment is correct, we have applied the "Vertex-to-Centroid Distance Method",[7] which gave the following centroid to atom distances (Ångstroms) using the current atom assignments:

C1 1.553(7), C2 1.597(6), B1 1.706(7), B2 1.701(7), B3 1.700(8), B4 1.705(8), B5 1.697(8), B6 1.695(7), B7 1.680(8), B8 1.691(7), B9 1.667(8), B10 1.671(8).

From these values, it is clear that the C and B atoms have been correctly assigned, as the centroid to C distances are significantly lower than the centroid to B distances. The magnitudes of these distances are also in agreement with the data for icosahedral carboranes in Table 2 of the abovementioned paper.[7]

In **7**: the structure was refined as a two-component twin, 0.9779(10):0.0221(11).

The crystal structure of **10** has been previously reported[8] with data collected at room temperature and a higher R-factor.

Table S1. Crystal data for **1** and **4-7**.

	1	**4**	**5**	**6**	**7**
Formula	$C_{32}H_{23}N$	$C_{12}H_{23}B_{10}I$	$C_{28}H_{29}B_{10}N$	$C_{34}H_{33}B_{10}N$	$C_{32}H_{37}B_{10}N$
FW	421.51	402.30	487.62	563.71	543.72
Size (mm)	0.12x0.05x0.03	0.13x0.11x0.06	0.26x0.17x0.07	0.28x0.15x0.11	0.16x0.10x0.05
Crystal system	Triclinic	Monoclinic	Monoclinic	Orthorhombic	Triclinic
Space group	P-1	$P2_1/c$	$P2_1/c$	$Pna2_1$	P-1
a (Å)	10.1137(7)	7.66445(9)	11.1826(2)	18.7163(3)	10.8530(5)
b (Å)	10.5179(6)	24.0864(3)	7.76362(13)	17.1816(3)	14.4693(7)
c (Å)	24.2285(15)	9.93244(11)	31.4490(6)	9.89979(15)	20.0555(9)
α (°)	84.313(5)	90	90	90	97.508(4)
β (°)	82.206(5)	91.4799(10)	97.4343(16)	90	91.388(4)
γ (°)	64.163(6)	90	90	90	90.186(4)
V (Å^3)	2295.9(3)	1833.01(4)	2707.38(9)	3183.53(9)	3121.5(3)
Z	4	4	4	4	4
D_{calc} (g cm^{-3})	1.219	1.458	1.196	1.176	1.157
μ (mm^{-1})	0.534	13.575	0.462	0.062	0.447
θ_{min} (°)	3.7	3.7	4.0	3.3	3.1
θ_{max} (°)	72.3	72.4	66.6	29.9	72.1
$N_{collected}$	13041	10125	29135	32872	20096
N_{unique}	8737	3629	29135	7657	11985
$N_{observed}$	5607 ($I > 2\sigma(I)$)	3539 ($I > 2\sigma(I)$)	27555 ($I > 2\sigma(I)$)	6532 ($I > 2\sigma(I)$)	9936 ($I > 2\sigma(I)$)
No. of parameters	595	209	353	407	778
R_1	0.057	0.023	0.121	0.043	0.139
wR_2	0.117	0.057	0.327	0.091	0.381
S	1.05	1.06	1.22	1.06	1.05
$(\Delta/\rho)_{min}$ (e Å^{-3})	-0.20	-0.67	-0.63	-0.25	-0.42
$(\Delta/\rho)_{max}$ (e Å^{-3})	0.27	1.02	0.54	0.21	0.63

Table S2. Crystal data for **8, 10, 11** and **14**.

	8	**10**	**11**	**14**
Formula	$C_{20}H_{27}B_{10}NO_2$	$C_{38}H_{43}NSi$	$C_{35}H_{35}N$	$C_{27}H_{43}B_{10}I$
FW	421.52	541.82	469.64	602.61
Size (mm)	0.15x0.12x0.05	0.10x0.07x0.05	0.15x0.10x0.04	0.13x0.09x0.05
Crystal system	Monoclinic	Triclinic	Triclinic	Monoclinic
Space group	$P2_1/c$	P-1	P-1	$P2_1/c$
a (Å)	19.7572(10)	9.6878(5)	11.5730(5)	12.37394(8)
b (Å)	7.1356(4)	13.3183(6)	12.1386(5)	15.47174(10)
c (Å)	16.9222(9)	14.0198(8)	12.2843(6)	16.34898(12)
α (°)	90	67.144(5)	105.841(4)	90
β (°)	106.060(5)	77.412(4)	108.491(4)	99.7934(6)
γ (°)	90	80.202(4)	110.908(4)	90
V (Å^3)	2292.6(2)	1619.43(15)	1375.96(11)	3084.34(4)
Z	4	2	2	4
D_{calc} (g cm^{-3})	1.221	1.111	1.134	1.298
μ (mm^{-1})	0.525	0.814	0.486	8.244
θ_{min} (°)	4.7	3.5	4.2	3.6
θ_{max} (°)	72.3	72.3	72.1	72.2
$N_{collected}$	7232	12065	8341	23841
N_{unique}	4393	6316	5247	6056
$N_{observed}$	3184 ($I > 2\sigma(I)$)	5468 ($I > 2\sigma(I)$)	4344 ($I > 2\sigma(I)$)	5830 ($I > 2\sigma(I)$)
No. of parameters	299	366	327	346
R_1	0.064	0.039	0.040	0.034
wR_2	0.159	0.093	0.098	0.097
S	1.07	1.03	1.03	1.09
$(\Delta/\rho)_{min}$ (e Å^{-3})	-0.29	-0.28	-0.17	-0.76
$(\Delta/\rho)_{max}$ (e Å^{-3})	0.60	0.31	0.23	0.58

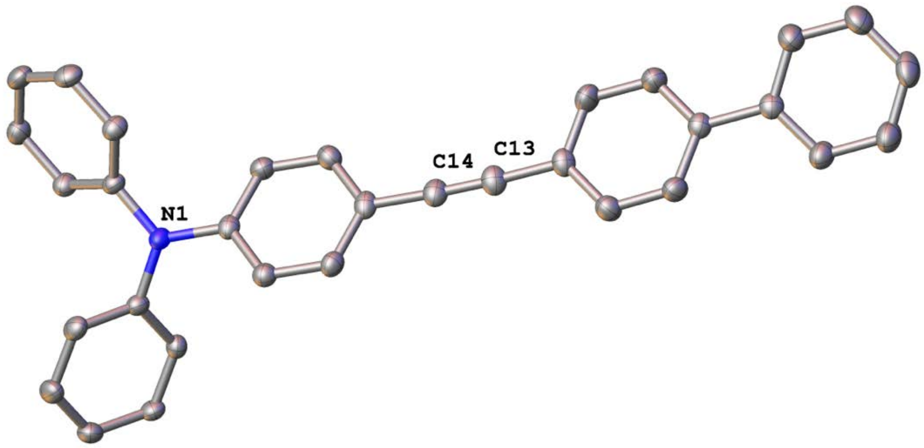

Figure S51. Molecular structure of **1**, with thermal ellipsoids set at the 40% probability level. Hydrogen atoms and the second crystallographically distinct molecule have been omitted for clarity. Selected bond lengths (Å): C1-C2 1.484(3), C13-C14 1.197(4).

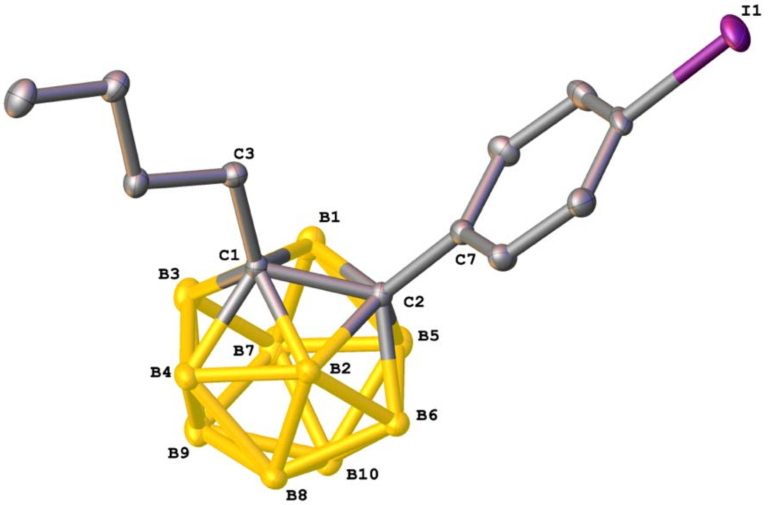

Figure S52. Molecular structure of **4**, with thermal ellipsoids set at the 40% probability level. Hydrogen atoms have been omitted for clarity. Selected bond lengths (Å): C1-C2 1.705(2), B(1)-B(3) 1.774(3), B(1)-B(5) 1.777(3), B(1)-B(7) 1.763(3), B(1)-C(1) 1.726(3), B(1)-C(2) 1.724(3), B(2)-B(4) 1.772(3), B(2)-B(6) 1.783(3), B(2)-B(8) 1.773(3), B(2)-C(1) 1.721(3), B(2)-C(2) 1.731(3), B(3)-B(4) 1.772(3), B(3)-B(7) 1.785(3), B(3)-B(9) 1.780(4), B(3)-C(1) 1.700(3), B(4)-B(8) 1.773(3), B(4)-B(9) 1.776(3), B(4)-C(1) 1.712(3), B(5)-B(6) 1.782(3), B(5)-B(7) 1.775(3), B(5)-B(10) 1.779(3), B(5)-C(2) 1.710(3), B(6)-B(8) 1.772(3), B(6)-B(10) 1.779(3), B(6)-C(2) 1.708(3), B(7)-B(9) 1.786(4) B(7)-B(10) 1.784(4), B(8)-B(9) 1.791(4), B(8)-B(10) 1.783(4), B(9)-B(10) 1.781(3).

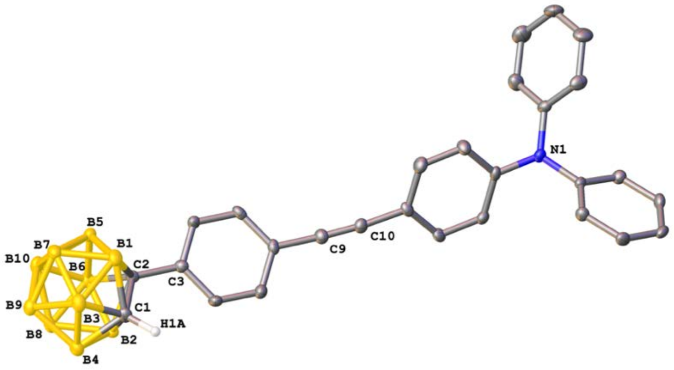

Figure S53. Molecular structure of **5**, with thermal ellipsoids set at the 40% probability level. Hydrogen atoms, other than H1A, have been omitted for clarity. Selected bond lengths (Å): C1-C2 1.484(3), B(1)-B(3) 1.786(12), B(1)-B(5) 1.774(11), B(1)-B(7) 1.759(10), B(1)-C(1) 1.716(10), B(1)-C(2) 1.739(9), B(2)-B(4) 1.767(11), B(2)-B(6) 1.778(11), B(2)-B(8) 1.773(10), B(2)-C(1) 1.715(10), B(2)-C(2) 1.733(9), B(3)-B(4) 1.791(11), B(3)-B(7) 1.779(12), B(3)-B(9) 1.779(11), B(3)-C(1) 1.697(10), B(4)-B(8) 1.792(11), B(4)-B(9) 1.789(11), B(4)-C(1) 1.698(10), B(5)-B(6) 1.786(10), B(5)-B(7) 1.783(11), B(5)-B(10) 1.776(11), B(5)-C(2) 1.722(9), B(6)-B(8) 1.786(11), B(6)-B(10) 1.787(10), B(6)-C(2) 1.717(9), B(7)-B(9) 1.779(11), B(7)-B(10) 1.775(11), B(8)-B(9) 1.775(10), B(8)-B(10) 1.790(12), B(9)-B(10) 1.773(11), C(1)-H(1A) 1.1000.

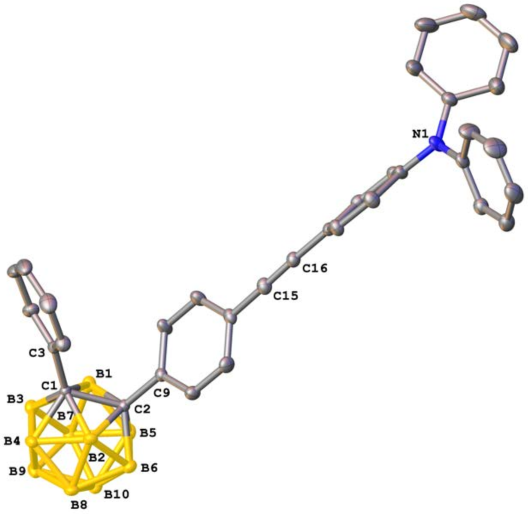

Figure S54. Molecular structure of **6**, with thermal ellipsoids set at the 40% probability level. Hydrogen atoms have been omitted for clarity. Selected bond lengths (Å): C1-C2 1.713(3), B(1)-B(3) 1.771(3), B(1)-B(5) 1.776(3), B(1)-B(7) 1.764(3), B(1)-C(1) 1.736(3), B(1)-C(2) 1.732(3), B(2)-B(4) 1.775(3), B(2)-B(6) 1.776(3), B(2)-B(8) 1.762(3), B(2)-C(1) 1.720(3), B(2)-C(2) 1.732(3), B(3)-B(4) 1.780(4), B(3)-B(7) 1.774(3), B(3)-B(9) 1.768(4), B(3)-C(1) 1.708(3), B(4)-B(8) 1.769(3), B(4)-B(9) 1.771(4), B(4)-C(1) 1.712(3), B(5)-B(6) 1.772(4), B(5)-B(7) 1.774(3), B(5)-B(10) 1.780(4), B(5)-C(2) 1.712(3), B(6)-B(8) 1.780(3), B(6)-B(10) 1.771(4), B(6)-C(2) 1.709(3), B(7)-B(9) 1.786(4), B(7)-B(10) 1.777(4), B(8)-B(9) 1.782(4), B(8)-B(10) 1.779(4), B(9)-B(10) 1.773(4).

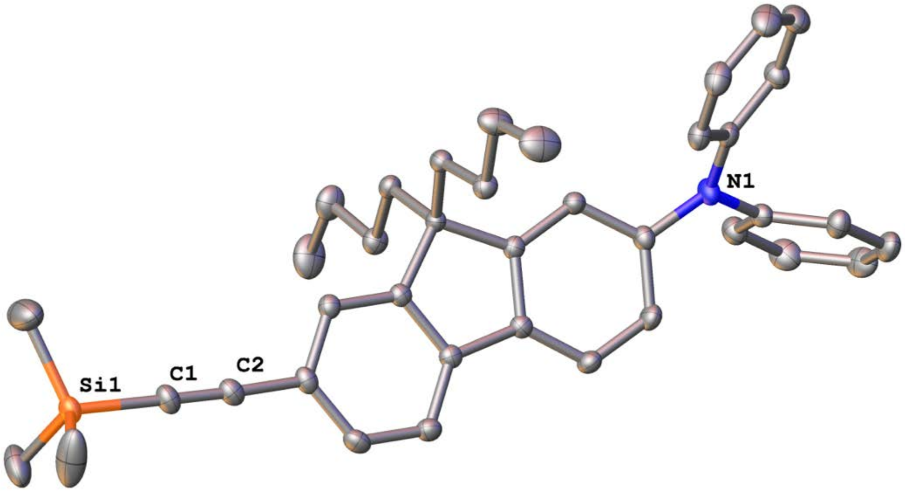

Figure S55. Molecular structure of **10**, with thermal ellipsoids set at the 40% probability level. Hydrogen atoms have been omitted for clarity. Selected bond lengths (Å): C1-C2 1.206(2).

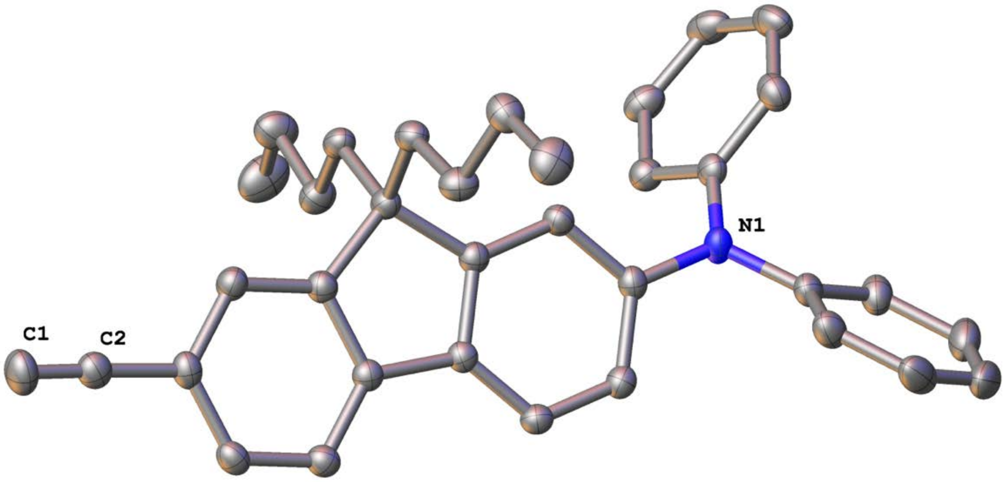

Figure S56. Molecular structure of **11**, with thermal ellipsoids set at the 40% probability level. Hydrogen atoms have been omitted for clarity. Selected bond lengths (Å): C1-C2 1.159(2).

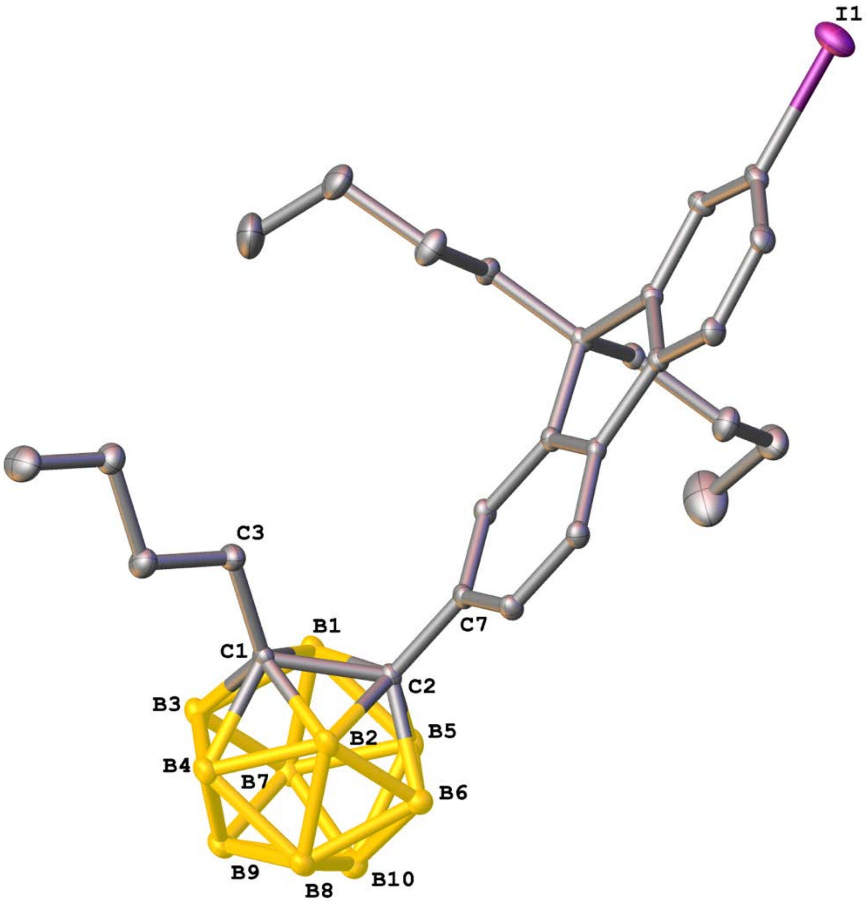

Figure S57. Molecular structure of **14**, with thermal ellipsoids set at the 40% probability level. Hydrogen atoms have been omitted for clarity. Selected bond lengths (Å): C1-C2 1.702(3), B(1)-B(3) 1.769(4), B(1)-B(5) 1.775(4), B(1)-B(7) 1.771(4), B(1)-C(1) 1.715(4), B(1)-C(2) 1.726(4), B(2)-B(4) 1.772(4), B(2)-B(6) 1.786(4), B(2)-B(8) 1.768(4), B(2)-C(1) 1.716(4), B(2)-C(2) 1.729(4), B(3)-B(4) 1.765(4), B(3)-B(7) 1.786(4), B(3)-B(9) 1.778(4), B(3)-C(1) 1.702(4), B(4)-B(8) 1.768(4), B(4)-B(9) 1.768(4), B(4)-C(1) 1.715(4), B(5)-B(6) 1.783(4), B(5)-B(7) 1.779(4), B(5)-B(10) 1.783(5), B(5)-C(2) 1.710(4), B(6)-B(8) 1.782(4), B(6)-B(10) 1.782(5), B(6)-C(2) 1.710(4), B(7)-B(9) 1.786(5), B(7)-B(10) 1.787(5), B(8)-B(9) 1.793(5), B(8)-B(10) 1.794(5), B(9)-B(10) 1.785(4).

Linear optical absorption data

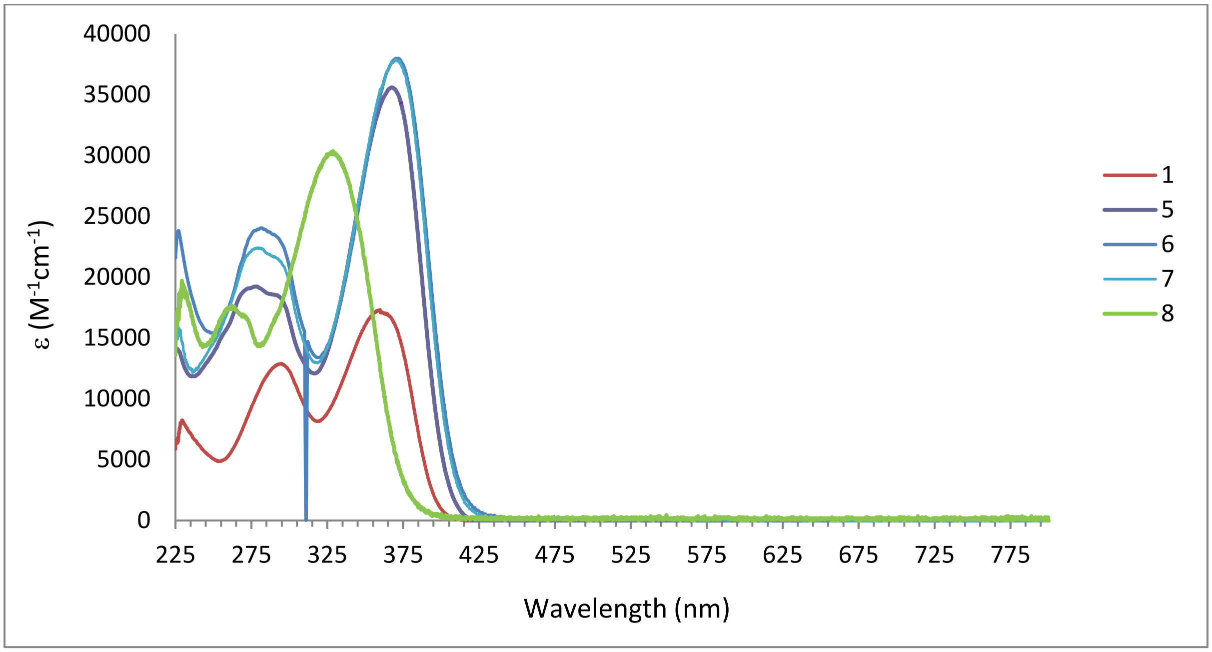

Figure S58. Linear optical absorption spectra of **1** and **5** - **8**.

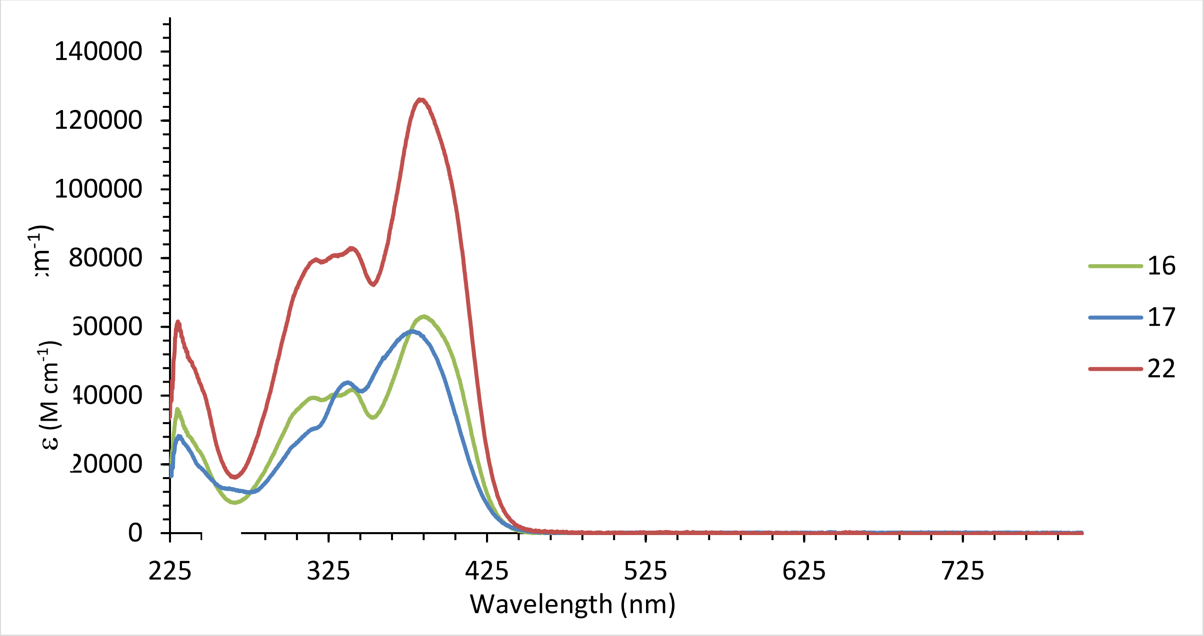

Figure S59. Linear optical absorption spectra of **16**, **17**, and **22**.

Hyper-Rayleigh scattering studies

The HRS measurement setup was similar to that reported in the literature.[9] A schematic diagram is shown in Figure S60. The laser used was a pulsed Nd-YAG laser (Spectra-Physics, GCR-150-30) with a maximum pulse energy of 200 mJ at a repetition rate of 30 Hz and at a wavelength of 1064 nm. The pulsed laser passed through a half-wave plate (HW) and a polarizer (P) that together form a beam attenuator (Thorlabs, VBA05-1064). The half-wave plate was mounted on a rotational stage that had a servo motor driver (PRM1MZ8E, Thorlabs). By controlling the rotation of the half-wave plate through a Visual Basic program, we were able to vary the incident laser intensity (or fundamental light intensity), but also to automate the measurement process. After passing the beam attenuator, a small portion of the incident laser light (around 10%) was reflected towards a battery powered Si diode (PD) via a beam splitter (BS: in practice, this was a microscope cover-slide). The signal from the Si diode served two purposes: it monitored the incident laser intensity and it provided the trigger signal for the oscilloscope. The majority of the laser beam was reflected by a laser line mirror (NB1-K14, Thorlabs) and subsequently focused via a focusing lens (FL, f = 75 mm, AC254-075-B-ML, Thorlabs) into the sample cell to generate HRS. The sample cell was a rectangular standard fluorometer cell with Teflon stopper (cell dimensions: 45 x 12.5 x 7.5 mm) and was placed so that the focal point of the beam was roughly in the middle of the cell.

To detect HRS, a camera lens (CL, Nikkor 50 mm, Nikon) was placed at 90 degrees to the beam propagation direction to collect the scattered light. A concave mirror (CCM, CM508-038-P01, f = 38.1 mm, Thorlabs) was placed opposite the camera lens at the other side of the sample cell to reflect back the scattered light. The camera lens not only collected all the scattered light, but also focused the light onto the open slit of a monochromator (MNCM, Spex 500M) which acted as a variable filter and allowed only the selected wavelength of light to pass. At the other end of the monochromator, a photomultiplier tube (PMT, R269 Hamamatsu) detected the HRS. The signals from both the Si diode and the PMT were passed to an oscilloscope (TDS2024C, Tektronix) for display and averaging. A dedicated PC with a custom-written Visual Basic program acquired data from the oscilloscope and ran the measurements automatically.

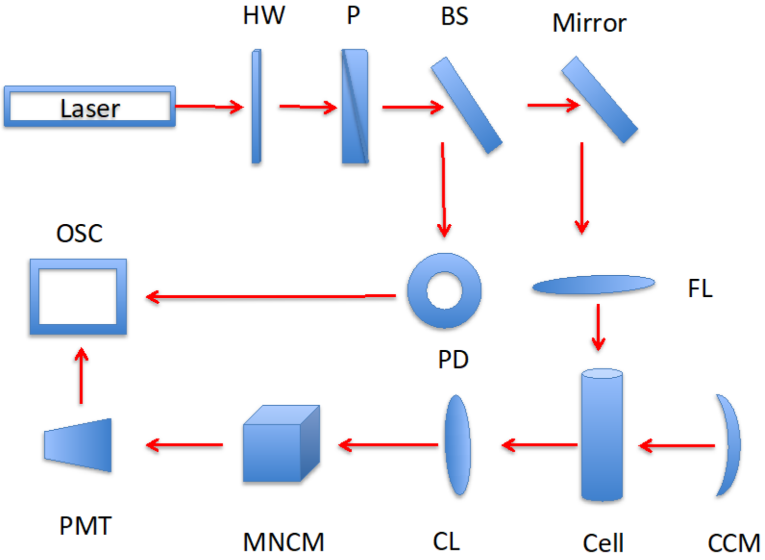

Figure S60. Schematic diagram of the HRS setup. BS: beam splitter, P: polarizer, HW: half-wave plate, OSC: oscilloscope, PD: Si photodiode, FL: focusing lens, PMT: photomultiplier tube, MNCM: monochromator, CL: camera lens, CCM: concave mirror.

We used the internal reference method to measure the first hyperpolarizabilities, <β>, of the compounds. Tetrahydrofuran (THF) was chosen as the reference solvent with a known <β> value of 0.44 x10^{-30} esu.[10] For any given compound solution, a maximum incident laser intensity was determined, to ensure that there was a reasonable scattering signal at 532 nm (likely HRS), but also that there was no decomposition of the sample. At the same time, at this maximum incident laser intensity, the wavelength setting on the monochromator was scanned at wavelengths around 532 nm to test if there was scattering at other wavelengths. When scattering was only observed at 532 nm, a quick check on a quadratic relationship between the scattering signal and the incident laser intensity was carried out, to confirm that the scattering signal was indeed HRS. Once the HRS signal was confirmed, HRS measurements were carried out by rotating the half-wave plate by means of a computer program, causing the incident light intensity to vary from minimum to maximum or vice versa, and at same time recording both the HRS signal and the incident light intensity. For each sample solution, the HRS measurement was repeated three times to average the large fluctuation of the HRS signals. As an example, Figure S61 shows the measured HRS signal as a function of incident intensity for **5** at various concentrations.

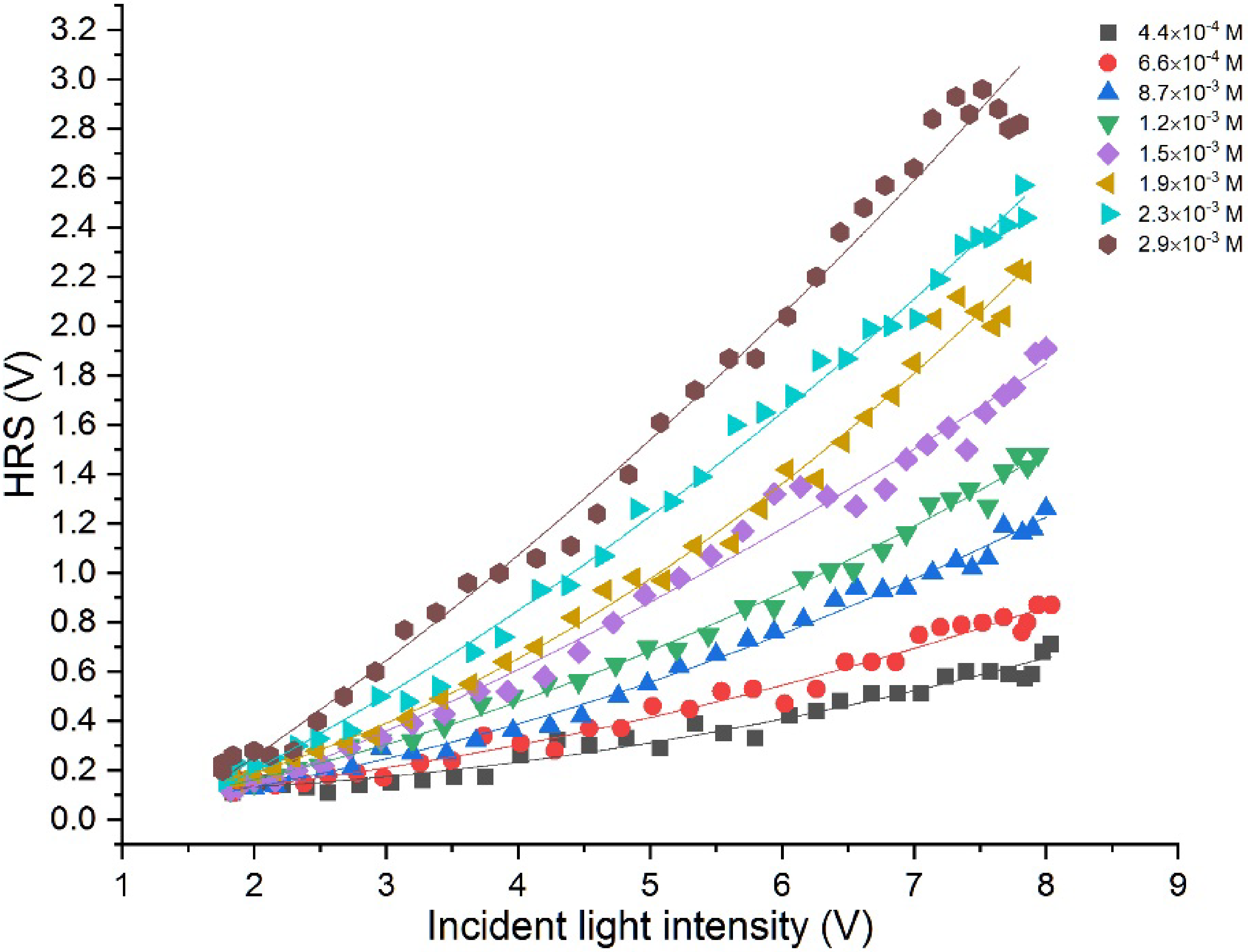

Figure S61. HRS signal of **5** as a function of incident light intensity and displaying a quadratic relationship.

Sometimes samples not only produce HRS, but also produce broad scattering around 532 nm due to fluorescence, etc. In order to extract the true HRS signal for those samples, a correction is needed for the measured scattering signal at 532 nm to remove the contributions from other sources. HRS is wavelength specific and under our setup with 1064 nm incident light, the HRS signal vanished when the monochromator wavelength was set 1 nm away from 532 nm. One way to correct is therefore to measure the scattering at 533 nm or 531 nm, and then subtract this from the scattering measured at 532 nm, assuming that the broad scattering from other sources has a similar intensity at 532 nm and 533/531 nm (a reasonable assumption given the proximity of the wavelength).

For any given compound/complex, a few milligrams of sample were dissolved in THF. The stock solution was then used to form a series of sample solutions with different concentrations (the concentrations were usually low: < 10^{-2} M). HRS measurements were then carried out on each sample solution. When a solute concentration is very low, the solution is sufficiently dilute that the measured HRS can be described as follows:[9]

$$I_{2\omega}/I^2_{\omega} = G[N_{solute}\langle\beta\rangle^2_{solute} + N_{solvent}\langle\beta\rangle^2_{solvent}]$$

where $I_{2\omega}$ is the measured HRS, I_{ω} is the incident light intensity, G is a calibration factor associated with setup and light collection efficiency, N_{solute} and $N_{solvent}$ are the number densities or molar concentrations of the solute and solvent in the solution, and $\langle\beta\rangle^2_{solute}$ and $\langle\beta\rangle^2_{solvent}$ are the first hyperpolarizabilities for the solute and solvent, respectively. A plot of $I_{2\omega}/I^2_{\omega}$ vs molar concentration of solute will yield a straight line (e.g. Figure S62).

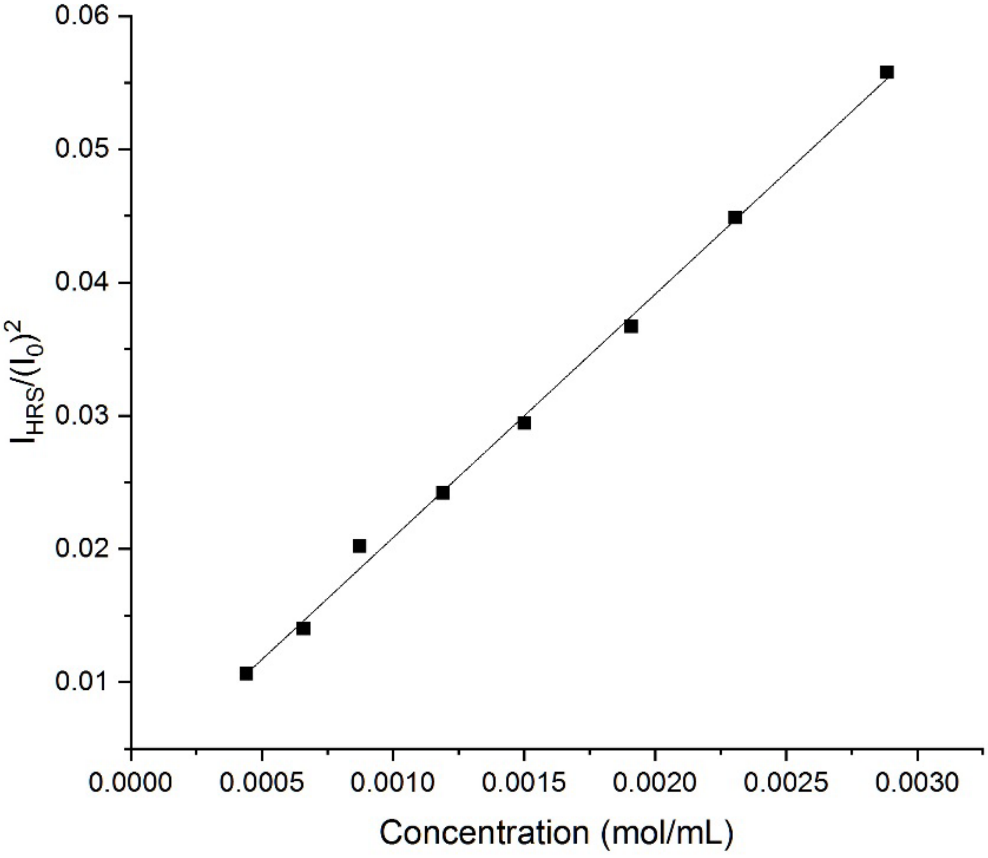

Figure S62. $I_{2\omega}/I^2_{\omega}$ for **5** as a function of solute concentration.

Uncertainties in HRS measurements may depend on many factors. Firstly, the HRS signal is partially associated with orientational fluctuations of all molecules in the solution, a random process that causes the HRS signal to fluctuate, so the β value is an average to control for these fluctuations; we averaged the HRS signal over 128 incident pulses (the maximum number of pulses that a Tektronix 2024C oscilloscope can handle). Statistically, the standard deviation for an average over 128 runs is ca. 10%. Secondly, the ratio $I_{2\omega}/I^2_{\omega}$ has a linear relationship with solute concentration when the solute concentration is very low, but when the solute concentration is high, the ratio tends to saturate for various reasons such as self-absorption, so the lower concentration region should be used or $<\beta>$ may be underestimated. Thirdly, each PMT produces dark current (electronic background noise). For compounds/complexes with large β values, the background signal is usually negligible, but for materials with small β values, a correction for this background signal is necessary and extra error on the HRS result is likely introduced. Fourthly, for materials with broad spectrum scattering around the HRS wavelength, the efficiency in separating the true HRS signal from other sources of scattering impacts the HRS results.

References

1. J. Cosier, A.M. Glazer, *J. Appl. Cryst.* **1986**, *19*, 105.
2. R.C. Clark, J.S. Reid, *Acta Crystallogr. A* **1995**, *51*, 887.
3. CrysAlisPro, Agilent Technologies, Yarnton, England, **2013**.
4 G. M. Sheldrick, *Acta Crystallogr. A* **2008**, *64*, 112.
5. G.M. Sheldrick, *Acta Crystallogr. C* **2015**, *71*, 3.
6. O. V. Dolomanov, L. J. Bourhis, R. J. Gildea, J. A. K. Howard and H. Puschmann, *J. Appl. Crystallogr.* **2009**, *42*, 339.
7. A. McAnaw, G. Scott, L. Elrick, G. M. Rosair, A. J. Welch, *Dalton Trans.* **2013**, *42*, 65.
8. J. G. Malecki, CCDC 1539900: *CSD Commun.* **2017**, DOI: 10.5517/ccdc.csd.cc1npd6y.
9. K. Clays, A. Persoons, *Rev. Sci. Instrum.* 1992, **63**, 3285-3289.
10. L. M. Tomalino, A. Voronov, A. Kohut, W. W. Peukert, *J. Phys. Chem.* 2008, **B112**, 6338-6343.